Reduction of Unsteady Underwater Propeller Forces via Active Tail Articulation

by

Richard A James

Submitted to the Department of Mechanical Engineering
in partial fulfillment of the requirements for the degree of

Master of Science in Mechanical Engineering

at the

MASSACHUSETTS INSTITUTE OF TECHNOLOGY

June 2006

Author .....
Department of Mechanical Engineering
May 12, 2006

Certified by .....
Dr Anuradha Annaswamy
Senior Research Scientist
Thesis Supervisor

Accepted by .....
Lallit Anand
Chairman, Department Committee on Graduate Students

Reduction of Unsteady Underwater Propeller Forces via Active Tail Articulation

by

Richard A James

Submitted to the Department of Mechanical Engineering
on May 12, 2006, in partial fulfillment of the
requirements for the degree of
Master of Science in Mechanical Engineering

Abstract

This study investigates the use of biologically-inspired tail articulation as a means to reduce unsteady propeller forces and by extension, noise due to stator wake blade interaction. This study is experimental in nature and testing was completed in a closed-channel water tunnel at the Naval Undersea Warfare Center in Newport, RI. A propeller-force measurement apparatus was designed and built to measure the forces and moments created by a spinning propeller behind a life scale stator model. Tests were conducted at a Reynolds number of 75,000 and stator tail articulation was carried out in the range of Strouhal number $0.0 < St < 0.13$. A variety of non-lifting propellers were used to investigate sinusoidal articulation profiles in the range of amplitudes (2°,5°,10°), and phase angles between propeller blades and stator ($0° - 360°$). It was found that stator articulation is capable of reducing the RMS of both unsteady thrust force and its time derivative as compared with a baseline static stator wake by choosing a suitable Strouhal number and phase angle. Tail articulation at $St < 0.08$ showed reduced unsteady forces for certain phase angles, while other phase angles demonstrated unsteady forces greater than the baseline wake. Articulation at $St > 0.08$ also showed unsteady forces that varied with phase but the associated unsteady forces were greater than the baseline wake for all phase angles. Similar results were obtained from spectral analysis where blade rate harmonics showed decreased magnitudes for certain phase angles at $St < 0.08$. A reduced order wake model was used to calculate the relative position of wake vortices and propeller blades which was used in turn to visualize the effect of phase angle on propeller blade-wake interaction.

Thesis Supervisor: Dr Anuradha Annaswamy
Title: Senior Research Scientist

Acknowledgments

This work was supported by the Office of Naval Research University/Laboratory Initiative project on Active Control of Blade Tonals (N00014-03-0777).

Firstly, I would like to thank all those people who assisted me over the course of this project for over a year and a half. My MIT thesis advisor Dr. Anuradha Annaswamy; my ONR-ULI advisor Dr. Steve Huyer; Charles Henoch and Dave Beal for all of your much appreciated time and effort at the water tunnel. I would also like to thank my friends and family for their much needed support and guidance as I completed my master's degree. Last but not least I would like to thank those at the Office of Naval Research University Laboratory Initiative program for the opportunity to complete my master's degree while completing such an interesting and challenging project.

I have learned much from the experiences involved in this project and I am sure they will serve me well throughout my future endeavors.

Richard A James

Contents

[1]This document contains several figures which look best when viewed in color. The reader is invited to request an electronic copy of this document in color from the MIT Library.

List of Figures

Nomenclature

A Wake width or tail displacement

α Angle of attack

β Blade pitch angle

c_0 Speed of sound

C_d Coefficient of drag

C_l Coefficient of lift

δ Boundary layer thickness

D Drag force

f Frequency

F Force

γ Point vortex strength

Γ Airfoil bound circulation

L Lift force

$\dot{L}$ Time derivative of lift force

L_{chord} Stator chord length

L_{tail} Length of hinged tail

ν Kinematic viscosity

ω Vorticity

Ω Blade rate

P' Acoustic pressure

Φ Potential function

Q Torque

r Radial distance

r_{blade} Radius of propeller blade

r_{ij} Radial distance from j to i

Re Reynold number

ρ Density of water

S Airfoil span

St Strouhal number

T Thrust

θ Angular coordinate

u Fluid velocity in the $\hat{x}$ direction

v Fluid velocity in the $\hat{y}$ direction

w Fluid velocity in the $\hat{z}$ direction

U Free stream u velocity

U_{blade} Nominal propeller blade inflow

$\hat{x}$ Direction of the tunnel flow

$\hat{y}$ Direction transverse to the tunnel flow

$\hat{z}$ Direction of gravity

Chapter 1

Introduction

1.1 Background

Some modern underwater vehicles use a swirl-inducing stator upstream of a propulsor' design (i.e. SISUP). As the name implies, such a design consists of an array of stators located upstream of a rotary propulsor which are placed radially on a cylindrical vehicle body. A stator is defined as the stationary part of a machine about which a rotor revolves. Stators can be found in both electric motors (as stationary windings) and gas turbines (as stationary vanes). In the case of underwater vehicles, however, stators are typically fin-like appendages placed on the surface of a vehicle body with the intention of providing directional or attitudinal stability.

Propeller or rotor blades generate both thrust and torque in the direction of their rotational axis. Much like a helicopter needs a tail rotor to counteract the reaction moment generated by its main rotor, a propeller-driven underwater vehicles requires stators to counteract the reaction torque created by the spinning propeller blades. If these stators were absent, the vehicle body would simply rotate in a opposite sense to the propeller and no useful work would be done. In an SISUP vehicle, stators have an additional function to pre-swirl the inflow to the propeller. Such a configuration results in more efficient thrust because less work is done to increase the angular momentum of the flow and flow separation due to high blade angles of attack is minimized. Figure 1-1 is a schematic of a propeller blade section where β is the local blade pitch angle, α the local angle of attack, Ω the blade rate, U the free stream velocity in the $\hat{x}$, V the free stream velocity in the $\hat{y}$ direction, U_{blade} the nominal blade velocity, L the lift force, D the drag force, Q the rotor torque and T is the thrust force used for propelling the vehicle.

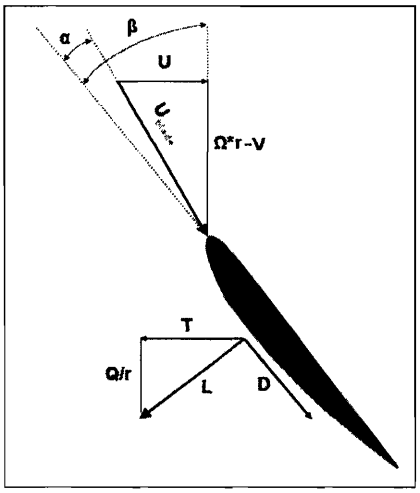

Figure 1-1: Forces acting on a propeller blade section

1.2 Problem Definition

Ideally, in a SISUP vehicle, upstream stators pre-swirl the inflow to the propeller blades uniformly so that a steady thrust force is produced. In a viscous fluid however, the no-slip boundary condition induces a boundary layer where local fluid velocity is much lower than the free stream velocity. The boundary layer represents the region of the moving fluid where energy has been removed due to the stator surface drag force. This effect persists downstream of the stator or any similar appendage, as a wake velocity defect. Although in practice most vehicle use stators downstream of the propeller, all vehicles have some sort of appendage which can create a wake deficit. Figure 1-2 shows the wake deficit generated by an upstream stator on a single propeller blade. The fluid inflow to downstream rotor blades becomes nonuniform. As the propeller blade passes through regions of varying flow velocity, the local blade

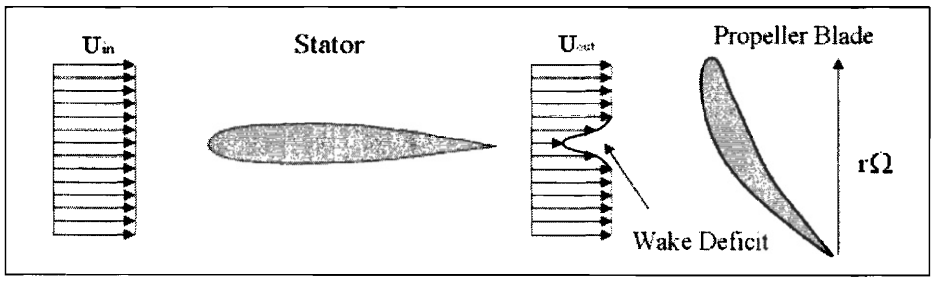

Figure 1-2: Wake velocity defect created downstream of stator

angle of attack α, varies since it depends on the angle of the local inflow velocity

U_{blade}:

$$\begin{aligned} \alpha &= \beta - \angle \vec{U}_{blade} \\ \alpha &= \beta - \arctan \frac{U}{\Omega r - V} \end{aligned} \tag{1.1}$$

For airfoils at low angles of attack, the lift generated by the foil is generally proportional to its angle of attack. As the blade's effective angle of attack changes, the blades experiences unsteady thrust forces (and to a lesser extent forces/moments in the other directions). Ross states that, "any rigid surface acted on by a non-steady force will radiate sound." [9] An unsteady force has an associated fluctuating pressure field which will directly radiate sound in a compressible medium. The expression for the acoustic pressure due to an unsteady concentrated force $\vec{F}$ at a fluid boundary is:

$$P'(\vec{r}, t) = \frac{1}{4\pi r} \nabla \cdot \vec{F} \left(t - \frac{r}{c_0} \right) \approx k_0 \dot{F} \tag{1.2}$$

where P' is the acoustic pressure, r is the distance from the source to the observer,$\vec{F}$ is the force vector acting on the body, c_0 is the speed of sound in the medium, k_0 is a suitably chosen constant, and $\dot{F}$ is the time derivative of the force. The noise generated by blade-wake interaction is called blade tonal noise. It occurs at harmonics of the blade passing rate because the motion of propeller blades is periodic in time. Noise sources associated with propellers typically dominate over other unsteady force sources because the highest local flow speeds around a vehicle usually occur at propeller blade sections. Blade tonals are particularly disadvantageous in military applications since they are commonly used to track and identify acoustic targets underwater. Such periodic forces are also undesirable because they may induce vehicle structural vibrations and lead to blade fatigue. Noise radiated by secondary vibrational sources is considered indirect radiation.

Experiments have shown that the primary component of directly radiated noise in SISUP vehicles is generated by blade-wake interaction. By reducing or altering the wake velocity defect created by upstream appendages, a vehicle's emitted noise could potentially be significantly silenced or its acoustic signature suitably altered to gain a tactical advantage. Several strategies to reduce radiated blade-wake noise have been attempted in the past [9]. One such method specified the use of unequal stator and/or blade spacing to reduce blade frequency tonals. Shaft-rate tonals however, are increased so that total sound output remains the same but with the spectrum has a greater broadband character. Changing the ratio of the number of blades to

the number of stators also has an effect on the generated noise spectrum, however primary blade-rate tonals are still strongly radiated.

1.3 Biomimetic Tail Articulation

The baseline wake deficit introduced by a stator may be thought of as the shedding of vorticity from the stator's boundary layer. The vorticity of a fluid particle is a vector quantity that specifies its angular velocity (actually vorticity is twice the angular velocity). Vorticity is the curl of a the particle's velocity vector. For a two-dimensional velocity field the vorticity, ω, is:

$$\omega = \nabla \times \vec{u} = \left(\frac{\partial v}{\partial x} - \frac{\partial u}{\partial y} \right) \hat{z}$$

The relationship between the baseline wake defect and vorticity in the boundary layer can be seen in figure 1-3. Two-dimensional vorticity is a scalar so it can readily be used to visualize the stator wake effectively.

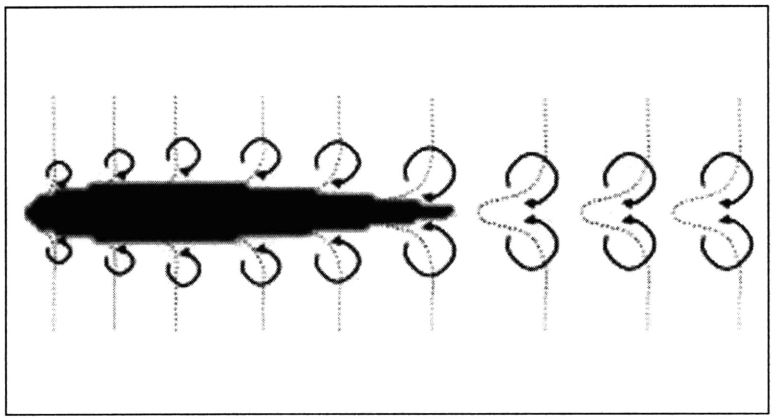

Figure 1-3: Wake deficit due to shedding of boundary layer vorticity

Biomimetic tail articulation has its roots in nature. With the help of millions of years of evolution nature has produced a variety of animals that can move and maneuver easily and efficiently underwater. Fish fins are control devices especially adept at propulsion and trajectory control. Typically, fish swim using one of two general methods: body and/or caudal fin (BCF) or median and/or pared fin (MPF) swimming. BCF swimming is the most common category of swimming in which fish use their caudal fin and/or undulating body motions to propel themselves. Other fish use BCF swimming to propel themselves via the formation of vorticity in the

flow. MPF swimming makes use of the complex and precise deformations achievable with the pectoral, dorsal and other fins for fine flow manipulation useful in low-speed propulsion, maneuvering, and stabilization.[4]

Much effort has been made to use biologically inspired swimming motions to solve propulsion and trajectory control problems in underwater vehicles. There has been extensive study of the propulsive efficiency of pitching and heaving foils modeled after BCF swimming[1, 2, 8]. Of critical importance in such studies is a dimensionless number relating to oscillating flows known as the Strouhal number, St, which is expressed as:

$$St = \frac{fA}{U} \tag{1.3}$$

where f is the frequency that vortices are shed into the wake and A is the width of the wake. The Strouhal number provides a relative measure of the spacing between vortices in a flow. The Strouhal number of vortex wake shed by a cylinder for example, where A is defined as the cylinder diameter, remains at a constant value of 0.22 for a wide range of flow speeds. Studies of oscillating foils have shown that highest propulsive efficiency is obtained within a specific Strouhal number region. In fact, it has been shown that a large range of fish and swimming animals beat their tails within this same Strouhal number regime, $0.25 < St < 0.35$. [10]

The SISUP propeller is a well developed technology and is effective for many types of missions, however the use of stator articulation may increase the viability of this noiser design. Instead of viewing oscillating foils as a propulsive means of their own, the goal of this study is to use the biologically-inspired method of stator articulation for noise control purposes. A schematic of the proposed addition of a tail affixed to the trailing edge of the stator blade is shown in Figure 1-4. The purpose of such an actuator would be modify the stator-wake for the purpose of either silencing blade tonal-noise or significantly altering a vehicle's blade-tonal acoustic signature via active control of an articulating stator trailing edge.

1.4 Previous Tail Articulation Research

W. Krol et. al [3] first numerically studied the use of tail articulation for blade tonal noise reduction. The effect of tail articulation on the wake was modeled as a point vorticity source at the stator trailing edge. Vortices were convected according to free stream velocity and the influence of wake vortices on each other. A 2nd order system was proposed that described propeller lift due to the wake effect. The system was

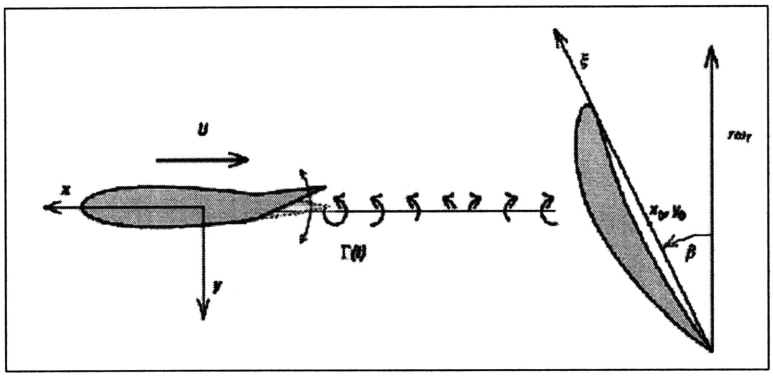

Figure 1-4: Schematic of stator-wake alteration vis tail articulation concept.

solved by setting the 1st derivative of the lift force, $\dot{L}$, to zero. The ideal vorticity input predicted by this model was a general non-sinusoidal, non-periodic function with a large noise reduction potential.

Experimental measurements on the effects of tail articulation on a stator wake were performed by D. Opila [6, 7]. Velocity measurements in an open channel water tunnel were made by using hot-film anemometry. The study showed that tail articulation was capable of reducing the wake deficit behind the stator by up to 60%. Opila found that optimal wake reduction by sinusoidal motions occured in the range of $0.25 < St < 0.35$ with A defined as the maximum tail deflection rather than the wake width. These measurement were completed at low speeds, $U = 4$ cm/s and low Reynolds number, $Re = 4000$. The Reynolds number is a critical dimensionless number for a large variety of fluid problems and is defined as:

$$Re = \frac{Ul}{\nu} \tag{1.4}$$

where l the associated length scale and ν the kinematic viscosity of the fluid. The Reynolds number provides a ratio of viscous to inertial forces in the fluid. At lower Re large scale viscous forces are more important than at higher Re. A transition from laminar to turbulent flow is associated with increasing Re. Tail articulation, in his experiments, was carried out by a stepper motor due to force and bandwidth requirements.

D. Macumber performed experimental measurements at high Reynold's number on the effect of stator articulation on a stator wake [5]. Experiments were conducted in a closed channel water tunnel in the range of $75,000 < Re < 300,000$, which more closely resembles the Re range in which typical autonomous underwater vehicles (AUVs) operate. Flow measurements were taken using both Laser Doppler

Velocimetry (LDV) and Particle Image Velocimetry (PIV). LDV was used to observe time-mean wake velocity measurements to quantify the relationship between St and drag coefficient C_d. Instantaneous velocity measurements using PIV were used to visualize the stator wake created by active tail articulation. Roll-up of an alternating vortex sheet shed by the stator was the primary descriptor of the active wake. At low Strouhal number the wake is deflected in a quasi-steady manner. At moderate St the vortex sheet began to roll up while at high St vortex roll up occurred quickly resulting in a strong vortex wake. A reduced-order model of the wake due to tail articulation was created which replicated vortex sheet roll up for sinusoidal and non-sinusoidal articulation profiles. A three dimensional propeller unsteady force (PUF) simulation was carried out using both PIV measured and simulated velocity data. Results from PUF simulations showed that reduction in the effective sound pressure level of radiated noise of up to 5 dB was possible using tail articulation. Interestingly, the predicted optimal sinusoidal tail articulation profile was one which, according to the measured St and C_d relationship would produce a high-drag wake. It was not known if this was a meaningful relation or simply a function of that particular movement profile. Estimates of the self induced noise due to tail articulation showed that the additional noise radiated was likely less than the achieved propeller noise reduction allowing for a net reduction in radiated noise.

Chapter 2

Unsteady Propeller Force Experiment

2.1 Experimental Concept

Experimental work done by Opila [6, 7] and Macumber [5] confirmed that tail articulation is able to reduce the wake deficit behind a stator for both high and low Reynolds number regimes. Predictions of blade tonal noise reduction however, were calculated through the use of reduced-order simulations. Several simplifying assumptions were made in order to ease the complexity of the wake generation, convection and interaction models. The wake created by the articulation stator was modeled as two-dimensional and both two and three dimensional propeller interaction simulations were created in order to estimate the ideal sinusoidal movement profile with the greatest reduction in blade tonal noise.

It is unclear however, how the complex three dimensional interactions between a stator wake and downstream propeller would affect the forces generated by the propeller blades. This study attempts to extend the work of Opila and Macumber by directly measuring the effect of an articulated stator-wake on a downstream propulsor. Instantaneous propeller force measurements behind an active wake were necessary to observe the potential effect of tail articulation on blade tonal noise. Forces and moments generated by a propeller in wake flow were measured in all 3 axes. This study concentrated on the impact of sinusoidal tail articulation profiles on potential blade tonal noise reduction.

2.2 Experimental Facility

This study required access to a high-speed water tunnel facility for controlled flow and force measurement experiments. The Naval Undersea Warfare Center in Newport, Rhode Island, NUWC-NPT, has a research water tunnel with a 12" (304.8mm) square cross section and a maximum flow speed of 30 ft/s (8 m/s). The facility is equipped with closed-loop velocity control and has removable plexiglass windows for tunnel access and to permit laser-based flow measurements. The NUWC water tunnel slowly expands in the downstream direction to account for boundary layer growth on the walls, minimizing the acceleration of fluid in the 10' long test section. The tunnel has a 3:1 ratio contraction section and a 6" thick honeycomb mesh with 0.25" cells, giving a 0.5% maximum turbulence intensity in the center of the tunnel. The tunnel is powered by a 24" single stage impeller with a 600 Hp electric motor. Both fresh and salt water testing is possible thanks to two large storage tanks located on-site. Laser PIV and LDV hardware was available to make both time-mean and instantaneous two-dimensional flow velocity measurements.

2.3 Experimental Apparatus Design

Several methods of propeller-force measurement were considered for this work. The mechanical design of the propeller apparatus would heavily depend on the way forces were measured and the fashion in which the propeller was to be actuated so it was critical to make such decisions early in the design process. The force measurement method was chosen first. There are several established ways to directly or indirectly measure propeller forces. A common method of measuring blade forces is instrumenting a propeller blade with an array of surface-skin pressure transducers in order to measure the pressure distribution across the blade. A fine array would allow for accurate calculation of blade forces with the added advantage of being able to observe local pressure changes and visualize hydrodynamic forces at various regions of individual blade sections. This method is extremely well suited for use on larger aircraft propellers and turbines. However, the diameter of the planned propeller blades was in the range of 6"-8" thus requiring a large number of sensors be affixed within an extremely small area. Furthermore, the sensors must be affixed to the blades such that they cause minimal flow disturbance, another challenge given the scale of the propeller blades. Another challenge of such a setup is that it would require the use of an underwater slip-ring in order to transmit data from the rotating propeller to

stationary acquisition equipment. Slip-rings are not typically compact devices making it difficult to incorporate one within the space available inside the 12" square test-section. Lastly, this study intended to use a number of different propellers with different blade sections in order to collect data at various flow velocities and Strouhal numbers. The cost and difficulty of individually instrumenting multiple propellers and the added difficulty of swapping propellers between tests was deemed too great.

A viable alternative to skin-pressure transducers was the use a one or more load-cell devices that could directly measure force. A load-cell is typically a strain-gage based device that is capable of measuring force (in reality strain) to a high degree of accuracy. In order for such devices to accurately measure 'true' forces it is critical that they are placed so that any forces and moments are completely supported by them and not any auxiliary apparatus structure. Load-cells are typically available in multi-axis designs were any forces/moments on the device can be resolved into orthogonal directions by the device's strain bridges. Mounting a propeller and all of its associated support structure directly to such a device which is then fixed to a rigid earth-ground connection would allow for direct measurement of all propeller forces and moments. The disadvantage of such a configuration is that forces and moments cannot be resolved individually by blade or blade-section. In the end, a six-component load cell was chosen as the force sensing device since they are available in a variety of form-factors suitable for placement within the water tunnel's test-section. Waterproof, pressure compensated devices are readily available 'off the shelf'.

The next major decision was choosing a method in which to actuate the spinning propeller. A motor was the obvious choice however there were certain requirements that had to be met. First the motor needed to have enough power to spin an underwater propeller at a rate of up to 1600 RPM. In order to link any measured force data, to the current propeller blade position a high resolution encoder was a necessity. Normally, these requirements could be easily met at a relatively low-cost by a variety of motors from many vendors, however the choice became more difficult once the decision was made that the motor must operate within the water tunnel section, and thus be waterproof. While it would have been feasible to spin the propeller using a motor outside the tunnel test section doing so would have required the use of a flexible drive shaft. Flexible drive-shafts allow the transmission of rotary motion along a curved path. They typically have low twisting and axial stiffnesses however, allowing a propeller to oscillate significantly while spinning. Driving the propeller by means of a motor mounted within the tunnel test-section would allow a rigid shaft connection to be used. A load cell cannot distinguish between inertial

and dynamic loads so removing any eccentric oscillating mass from the system was a priority. Mounting the propeller motor to the load cell would allow torque about the propeller's rotational axis to be measured (i.e. torque required to spin the propeller). It was deemed necessary to encase the propeller support structure, motor, and load cell within a streamlined faring so that only hydrodynamic forces acting on the propeller blades would be measured by the load cell. A custom acrylic window was machined to mount the stator and propeller apparatus.

Figures 2-2 & 2-1 show a CAD model and picture of the finalized propeller-force apparatus. The force-measuring apparatus consists of a six-component load cell rigidly mounted to an acrylic water tunnel window through a machined aluminum base adapter. The propeller motor is attached to the load cell through an aluminum mounting flange which also supports the propeller shaft bearings encased in their own separate aluminum bearing block. The apparatus was designed as a modular system to allow for ease of manufacture, access and modification. All aluminum parts were clear-anodized to protect against corrosion and only stainless steel fasteners were used. The fairing assembly and propellers were all created by a stereo-lithography (SLA) process in stiff, water proof materials for maximum strength and durability. A smooth surface finish on both propellers and fairing was specified to minimize any flow disturbance.

An Advanced Mechanical Technology, Inc. (AMTI) MC1 six-component load cell was chosen to measure the forces generated by the propeller. This transducer is capable of resolving forces and moments in all three axes using multiple internal bridges. The load cell features stainless steel, waterproof construction and is hydrostatically compensated for use underwater. An AMTI MiniAmp was used as a strain bridge excitation amplifier for the load cell. This amplifier was recommended by AMTI for use with the MC-1 load cell and outputted six analog voltage channels with individually selectable channel gains and excitation voltages. The load cell amplifier contained an internal 1 kHz anti-aliasing filter for every channel. Additional external low-pass butterworth filters were used to prevent aliasing from any high-frequency electrical noise that was picked up between the amplifier and the data acquisition system.

A waterproof Stoegra SM56.3 two phase hybrid stepper motor capable of 2500 rpm and with a stall torque of 1.2 Nm was chosen to spin the propeller. An 500 pulses per revolution encoder is integrated into the motor body. A stepper motor was used because at the time, this particular motor was the only easily available waterproof motor with the appropriate functional characteristics and form-factor that fit within the study's fiscal constraints. An Applied Motion 7080 micro-stepping drive was

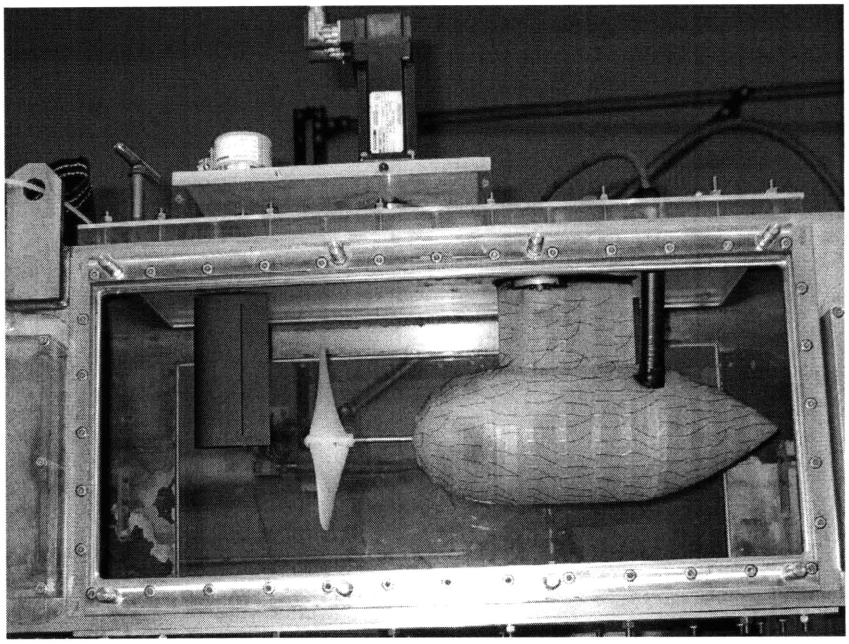

Figure 2-1: Finalized propeller-force & stator flapping apparatus in NUWC water tunnel.

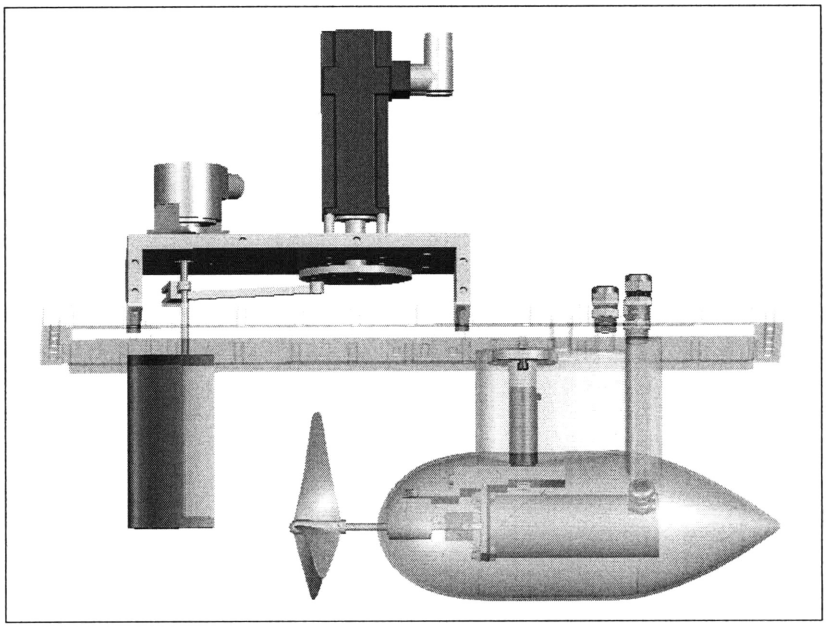

Figure 2-2: CAD model of finalized propeller-force apparatus in NUWC water tunnel.

used to power the motor. The same tail flapping apparatus used by Macumber in [5] was used in this experiment to create an active stator wake. A Kollmorgen Goldline XT brushless servo motor provides the torque and velocity necessary to articulate the stator tail. An AMC DR100E servo drive was used to power the servo motor. The motor is capable of 6000 rpm and 0.44 Nm of stall torque and spins a rotary link which in turn drives a linear linkage thus converting the its rotary motion into sinusoidal angular displacements. The crank rocker mechanism allows the servo motor sinusoidally flap the stator while the motor spins continuously in one direction. The length of the rotary link is adjustable to allow the amplitude of stator oscillation to be changed quickly between experimental tests. A Stegman C16 2000 PPR encoder is coupled directly to the stator tail shaft to allow for direct measurement of tail position.

A National Instruments (NI) PCI-7344 motion control card with 4 separate axis of servo/stepper is used to control the motions of both motors and to read tail encoder position. A National Instruments PCI-6220 data acquisition card was used to measure the six channels of analog voltage produced by the AMTI load cell amplifier. The card is capable of acquiring data at a rate of 250 kilo-samples per second with 16 bit A/D resolution. Both NI cards were linked together using a RTSI-bus cable to allow for real-time synchronization of voltage and position acquisition.

The flapping stator apparatus consists of an EDM machined aluminum hydrofoil with a NACA 0020 profile. This profile was chosen in order to generate a thicker wake deficit. The stator has a span of 6" so that it spans only half the height of the test channel as requested by the sponsor. The stator has a 3" chord length while the length of the articulated trailing portion is 1". More details of the stator apparatus can be found in [5]. Most tests were completed at a tunnel velocity of 1m/s which corresponds to a chord length *Re* of 75,000.

2.4 Experimental Test Scenarios

The reduced-order propeller model created in [5] assumed minimal influence of the propeller blades on wake flow. In order to satisfy this assumption, propellers were chosen that were capable of producing no lift so that they would not introduce further circulation into the flow. Propellers were designed with NACA 0012 profile blade sections. This meant that at every point along the span of a blade, the chord section was symmetric. Blade twist is specified such that at a particular rotation rate the effective angle of attack for each chord section is constant along the propeller span.

As one moves outwards along the span of a propeller blade, the twist of each blade section is increased to account for increasing angle at which the flow impinges on it. At a certain ratio of tunnel velocity to rotation velocity, these propellers produce zero-lift at every point along their span. Figures 2-3 and 2-4 are CAD models of two of the propellers used in testing.

It is necesary to maintain a constant phase angle between stator flapping and propeller blade position during active flapping. The stator was actuated so that the flapping rate was equal to the blade passing rate. I.e. if a three bladed propeller spun at 304 RPM, equivalent to a shaft rate of 5.07 Hz, the flapper motor would spin at 912 RPM equivalent to a flapping rate of 15.21 Hz. This ensures that every blade on a propeller sees an identical wake velocity field. It was desired to maintain the no-lift criteria so various propellers were required in order to achieve a range of flapping rates for a given tunnel velocity. The phase angle was defined by the position of the stator tail within its oscillation period as a propeller blade passed directly behind the wake. Experiments were conducted from $0° - 360°$ phase in $20°$ increments for every propeller. Table 2.1 shows the list of propellers and their no-lift rotation speeds for a tunnel velocity of 1m/s. For a particular Strouhal number, once U and f are specified by choosing a certain propeller, the only available parameter becomes the flapping amplitude. $2°$, $5°$, and $10°$ flapping amplitudes were studied for every test scenario. Table 2.2 shows St as a function of A and f. For every value of St in the table 2.2, tests were conducted with both two and three-bladed propellers over the range of phase angles, resulting in a total of 12 no-lift test scenarios.

Blade #	RPM @ 1m/s		Label	
2	304	456	A	B
3	212	304	C	D

Table 2.1: List of experimental propellers

	Stator Rate f (Hz)	
A (deg)	10.67	15.2
2	0.0187	0.0269
5	0.0468	0.0673
10	0.0932	0.1341

Table 2.2: St as a function of A (deg) and f (Hz) at $U = 1$ m/s

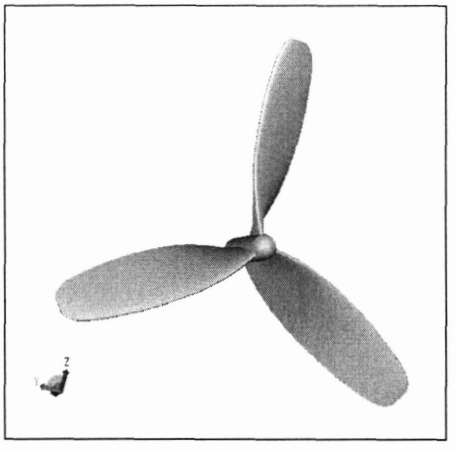

Figure 2-3: Rendering of a three-bladed propeller (8" diameter, 212 RPM @ 1m/s)

Figure 2-4: Rendering of a two-bladed propeller (8" diameter, 456 RPM @ 1m/s)

Chapter 3

Propeller Force Measurements in Baseline Wake

Forces due to the baseline non-flapping stator wake must be accurately measured in order to compare them to those produced due to an active stator-articulated wake. This section outlines those forces and the steps required to measure them accurately.

3.1 Tunnel Calibration

In order to correctly conduct experimental tests inside the NUWC water tunnel it was calibrated so that a known free stream velocity U could be set. The NUWC water tunnel uses a closed-loop controlled electric motor to ensure a constant impeller rotational speed. The relationship of tunnel rotational speed to tunnel free stream varies according to tunnel blockage and head loss created by objects placed within the test section. The propeller force apparatus and fairing was placed in the tunnel and free stream velocity was measured using LDV while the tunnel rotational speed was recorded. Velocity was measured at a point in the center of the test section approximately 26" upstream of the force apparatus. Figure 3-1 shows the results of this calibration. Tests were conducted with the propeller removed, with a spinning propeller, and with the stator removed. The difference between these cases was found to be minimal. As expected from previous calibration tests, the tunnel calibration was found to be linear. The best fit line does not pass through the origin but instead through $U = -.047$ m/s at zero tunnel speed implying that at low tunnel speed, the relationship breaks down as viscous effects become greater.

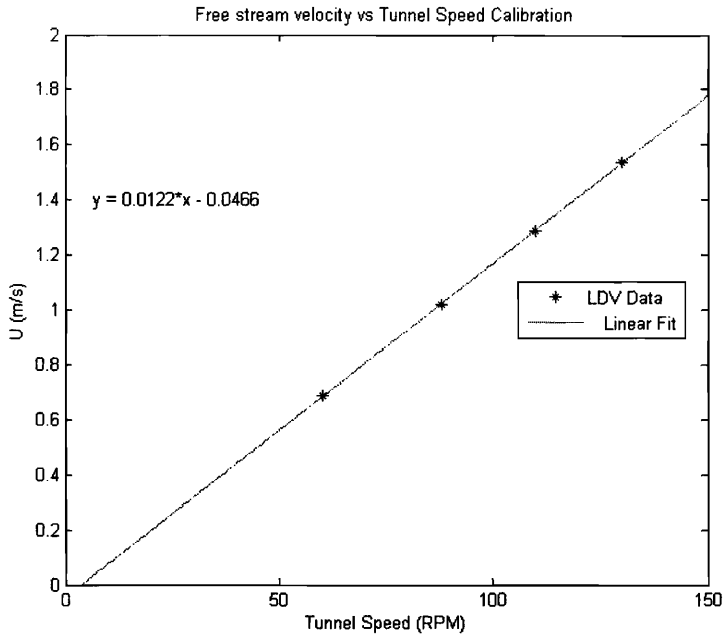

Figure 3-1: NUWC tunnel calibration: U vs RPM

3.2 Fairing Design and its Effect on Propeller Forces

In order to ensure that forces and moments measured by the load cell were due to forces acting on the propeller blades and not hydrodynamic forces acting on the motor and transducer supporting structure, a fairing was used. A fairing was designed so that it would enclose the load cell, motor and supporting structure. A small hole in the front of the fairing allowed a shaft to extend into the tunnel flow to mount a propeller. The fairing was mechanically attached only to the tunnel window so that any hydrodynamic forces acting on the fairing would be transmitted to the window and not the load cell. Great care was taken so that the fairing was large enough to encase the measurement apparatus with a smooth shape to prevent flow separation. The size of the fairing within the tunnel was critical in order to keep its effect on flow within the test section to a minimum. As Bernoulli predicts, when an ideal fluid within a channel encounters a contraction, flow velocity increased in order to maintain a constant mass transport rate. The fairing creates a blockage in the tunnel so as water flows around the fairing it is accelerated. In this region of accelerated flow, fluid pressure drops. Since the fairing is a streamlined body in the flow, it also creates a stagnation point at the leading surface. Near this region the flow is decelerated and pressure increases. Therefore the fairing could potentially have a significant effect on

the fluid flow field and on propeller forces. The fairing is not axi-symmetric, due to the streamlined strut which encloses the load cell. Therefore the stagnation field it creates is not axisymmetric within the tunnel. A propeller blade rotating within an non-axisymmetric flow field will see an unsteady flow field and it will induce unsteady forces in the propeller. Careful design of the fairing reduce this effect to a minimal level.

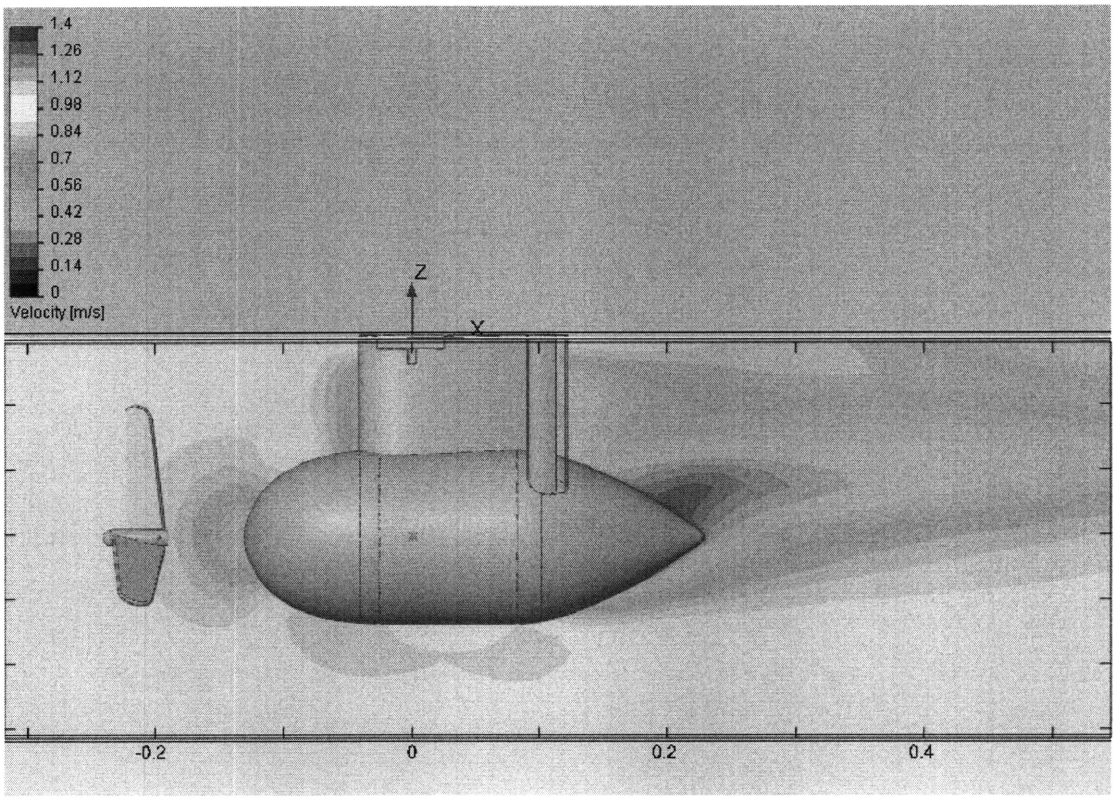

Figure 3-2: Side view of fairing CFD results @ 1m/s

Once an initial fairing design was created, Cosmosworks computational fluid dynamics (CFD) software was used to model the flow of water within the tunnel. The overall fairing diameter and the shape of its leading and trailing surfaces were adjusted in order to reduce its effect on the flow. A crucial parameter was the distance between the fairing leading surface and propeller blades. The greater this distance the lesser the impact the fairing would have on a propeller. This distance was limited by the geometry of the loadcell/motor support structure. In other words, the length of the leading fairing surface could be shortened to increase the propeller separation distance however as this length is shortened the curvature of this surface increases which potentially creating a leading surface separation point. The flow field at po-

sitions corresponding to the leading and trailing propeller edge planes was closely evaluated so that it was as close to uniform free stream flow as possible. Figures 3-2 and 3-3 show images of the fairing after CFD analysis at a tunnel velocity of 1 m/s. Flow separation is noticeable at the aft portion of the fairing, likely due to the disturbance created by the cable struts. Since separation occurs at the aft portion of the fairing, well downstream of the propeller and stator, it was deemed acceptable.

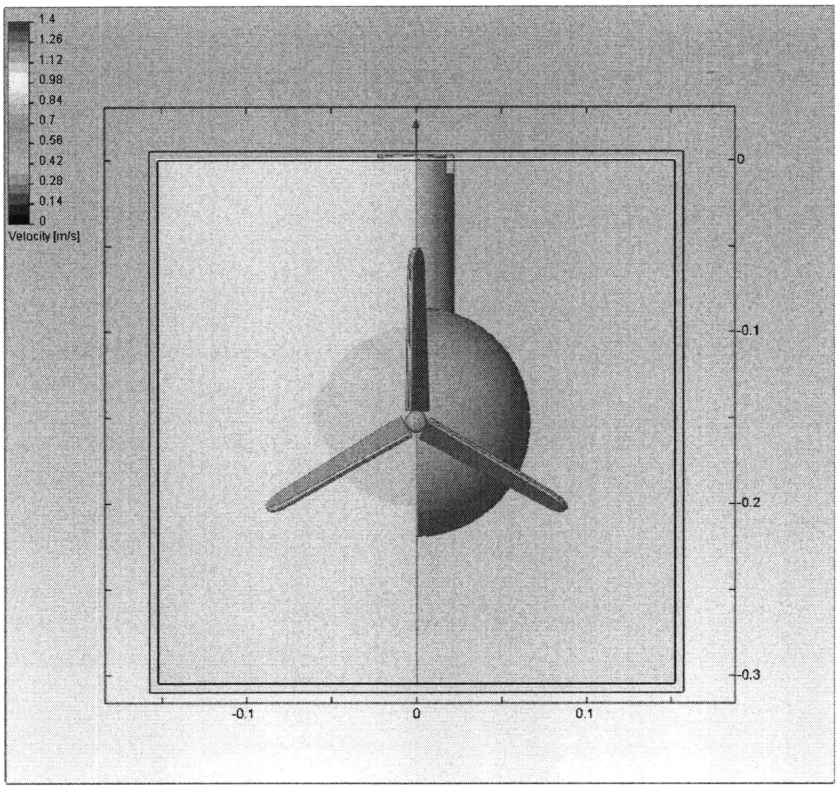

Figure 3-3: Front view of fairing CFD results @ 1m/s

Once a satisfactory design was achieved, it was created using SLA. The flow field due to the fairing at 1 and 2 m/s was measured using LDV. Figure 3-4 shows the effect of the fairing on the flow field at a distance of 1" upstream of the fairing's leading surface. Figure 3-5 shows the velocity field at a vertical plane intersecting the propeller's trailing edge. At this plane, the free stream velocity is reduced by up to 91% of its free stream value. Due to the tunnel blockage effect on this plane, the streamwise velocity can see values as high as 108% of the free stream value. As the distance from the fairing increases its effect on the flow field decreases. As figure 3-6 shows, the stream wise flow velocity is not greatly affected by the fairing's presence due to its separation. It is important to note that the edges of the tunnel close to the horizontal tunnel walls could not be measured with the LDV apparatus.

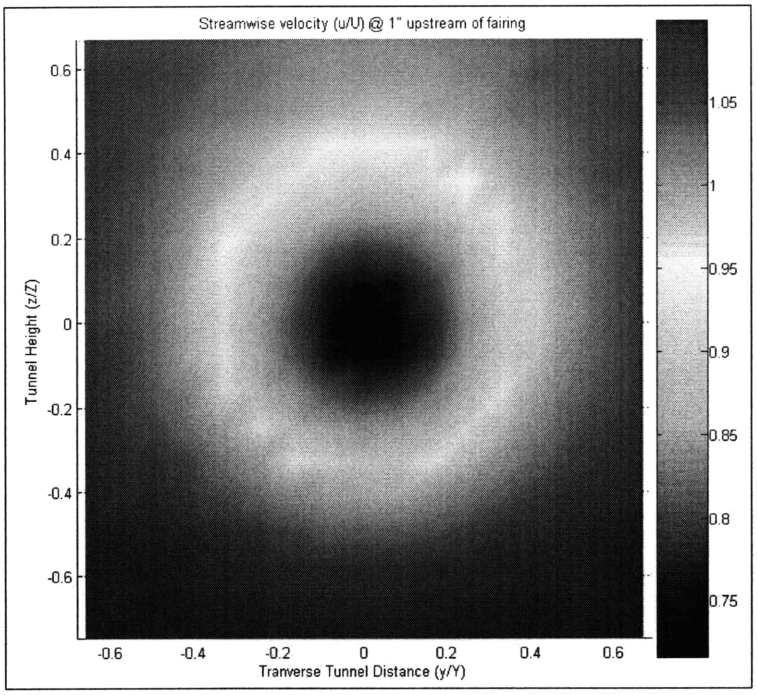

Figure 3-4: u velocity recorded by LDV 1" upstream of fairing @ 1m/s

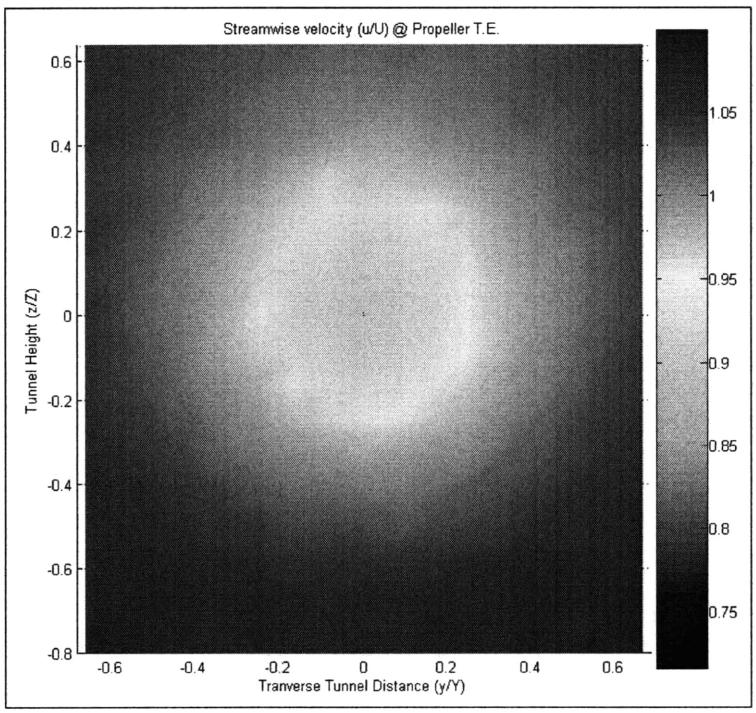

Figure 3-5: u velocity recorded by LDV at propeller T.E. @ 1m/s due to fairing

The ultimate effect of the fairing on unsteady propeller forces was observed through direct force measurement discussed in the following section.

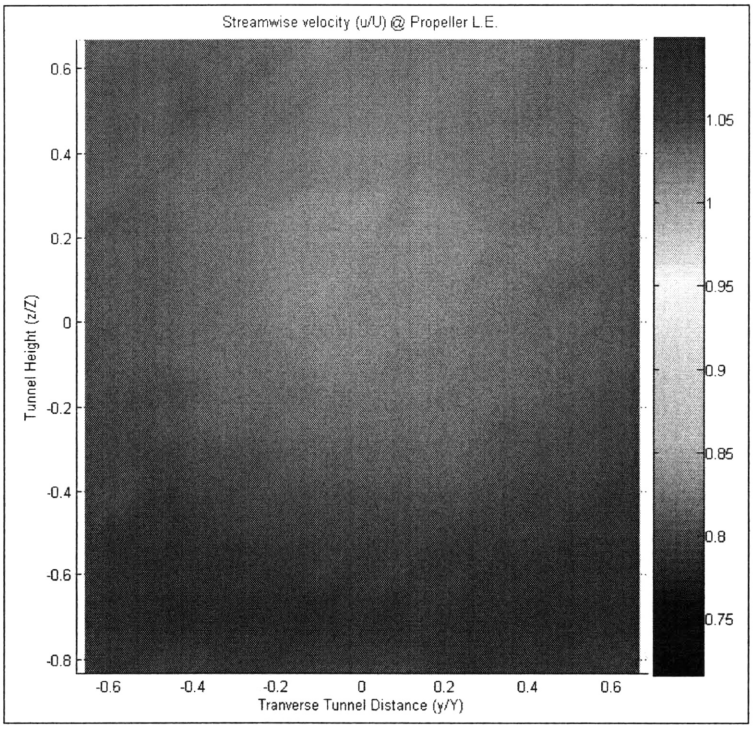

Figure 3-6: u velocity recorded by LDV at propeller L.E. @ 1m/s due to fairing

3.3 Propeller Forces in Free stream

In addition to forces created by the fairing effect, mechanical imbalances and vibrations could be recorded by the load cell as forces and moments since it cannot distinguish between dynamic and purely inertial loads. Rotational eccentricities would be measured as a cyclical forces/moments. Additionally, the measurement apparatus' vibrational response could introduce significant inertial loads at the apparatus' damped natural frequency. It is crucial that this effect be accounted for when analyzing force data. The tunnel test section is square and not axisymmetric so it was possible that there could be a wall effect on the forces generated near the propeller blade tips. For these reasons, the apparatus was used to measure the unsteady propeller forces present when the propeller is spinning in wake-free flow (i.e. the removed stator). As mentioned previously, radiated noise is related to the temporal derivative of hydrodynamic forces. This study will concentrate on the unsteady characteristics of the thrust force generated by a propeller. This corresponds to the x axis force channel which measures forces in the direction parallel to the tunnel's axis. Using the data acquisition system all six channels of force/moment data were recorded at 2500 Hz. The propeller-driving motor's angular position was recorded simultaneously

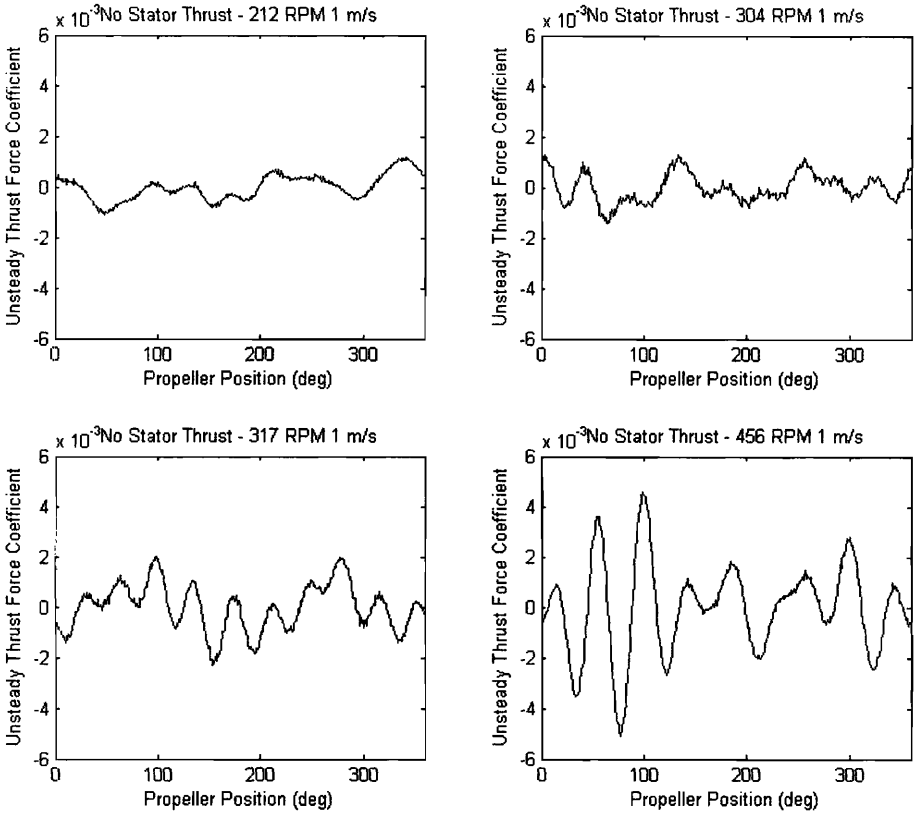

Figure 3-7: Unsteady Thrust Force Coefficient for various propellers spinning at their no-lift speeds at 1m/s in a stator-less wake

so that forces acting on the propeller could be correlated to blade position. Data is software filtered with a butterworth low-pass filter to remove any signals which occur at greater than ten times the shaft rate. The filter is applied using the the Matlab function *filtfilt* which applies the digital filter twice in the forward and backwards directions. This removes any phase distortion introudced by the forwards filtering. Data is sorted into 1° bins and averaged, which filters out any noise or force which does not occur at multiples of the propeller's shaft rate. Figure 3-7 shows the thrust force measured using all four propellers spinning at their no-lift velocities in 1m/s flow. In this case, there was no stator upstream of the propeller so it experienced a relatively uniform flow field except for that created by the fairing. Measured force has been nondimensionalized by dividing it by $\frac{1}{2}\rho U^2 A$, where ρ is the density of water, U is the free stream velocity, and A is the swept area of the propeller.

In figure 3-7 one can see that the maximum unsteady thrust coefficient seen in

stator-less flow is 0.005. The largest value unsteady thrust was seen in the propeller with the greatest design speed. Although each individual propeller will has a slightly different force signature due to manufacturing imperfections, as expected the propeller spinning at the largest rate showed with the largest instantaneous thrust coefficient.

The following section quantifies the propeller forces generated downstream of a stator and it will demonstrate that the forces due to mechanical imbalance, vibration and fairing are small in comparison.

3.4 Propeller Forces in baseline stator wake

The purpose of this study was to explore the effect that stator tail articulation would have on unsteady forces generated by a downstream propeller. This section will concentrate on discussing those forces. As mentioned in section 1.2, the thrust created by a propeller blade varies over a period of rotation if it encounters an unsteady flow field. The boundary layer on the surface of an upstream stator creates a wake defect in the flow field were the velocity in the stream wise direction, u is significantly reduced from the free stream value U. As a propeller blade enters the wake, the incoming velocity vector seen by each blade section changes ao the angle of attack of each blade section decreases. For the propellers used in this study, a negative in angle of attack creates of positive thrust. As a blade leaves the wake, the angle of attack on the blade increases so the thrust generated falls once more.

The sudden change in lift occurs at every blade-wake crossing. Therefore one would expect the measured thrust force versus propeller position signal to be periodic showing the same number of peaks as blades. Figure 3-8 illustrates the thrust coefficient versus position for each of the four propellers observed. As expected, the three bladed propellers (two uppermost graphs) demonstrate force trace patterns that repeat three times per cycle, once for every blade. The two bottom graphs correspond to two-bladed propellers which show a pattern that repeats twice per rotation cycle. The stator and propeller were oriented so at a propeller position of 90° a blade is directly inline with the stator. For a two-bladed propeller, the second blade becomes aligned behind the stator 180° later at 270°. For a three-bladed propeller, the second and third blades cross directly behind the stator at 210° and 330° respectively. Closer inspection of figure 3-8 reveal that the highest force peaks occur at the angular position where a propeller blade is aligned with the stator. In other words, spikes in thrust occur when propeller blades cross the stator induced wake. Furthermore it becomes apparent that as one compares propellers of increasing velocity, from left

to right, the force peak becomes larger. As a propeller's velocity increases, the span of time spent within the wake decreases. This also means, however that the rate of change of velocity per time increases as the flow disturbance seen in each cycle occurs in a shorter span. An additional way to explain why the disturbance due to the wake increases with propeller speed is simply that flow velocities increase. Simple linearized foil theory predicts that lift due to a foil section is directly related to fluid velocity over that foil and the angle of attack of the fluid. In other words, on the propellers with a greater design speed, each blade section sees an incoming flow with a greater magnitude which would lead to a greater change in lift for a given change in angle of attack.

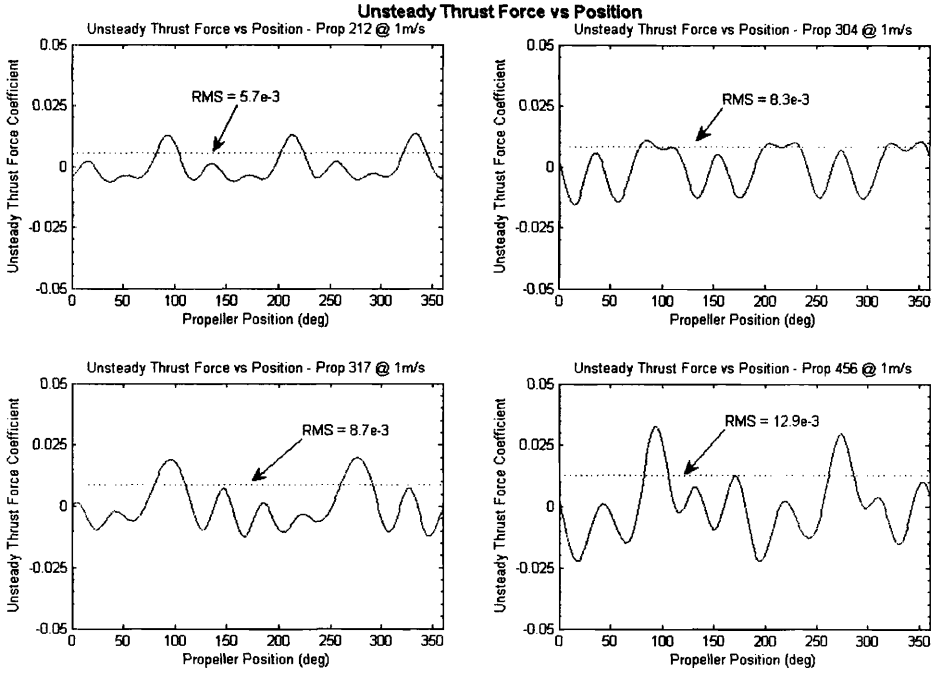

Figure 3-8: Unsteady Thrust Coefficient vs propeller position for various propellers in a baseline stator wake @ 1m/s

Figure 3-8 also exhibits secondary peaks within the recorded data. The figures suggest that immediately after a propeller blade encounters the wake there are secondary forces of smaller magnitude. These force oscillations to decay before the next blade-wake crossing. It is unlikely that these secondary peaks are due to flow phenomena given the relatively large separation between blades on a propeller. Instead these peaks are likely forces measured due to mechanical vibrations of the apparatus.

As a propeller blade crosses the wake, it encounters what is essentially an impulsive

lift force. Such an impulse is likely exciting structural vibrations in the propeller force apparatus. In the upper left graph of figure 3-8 these secondary peaks occur about 10° later than the phase crossing resulting in what appears to be a much wider wake crossing peak than the other three graphs. Due to the design of the measurement apparatus, the loadcell is the main structural member of the system. The vibrational response of the device was measured underwater in order to determine its natural frequency, which could interfere with accurate force measurement confused. Figure 3-9 shows the spectrum of the force measured by the load cell after the apparatus was tapped in water with a wrench. From the figure it is apparent that the apparatus has a strong vibrational response at 45 Hz which must be taken into account when considering recorded force data.

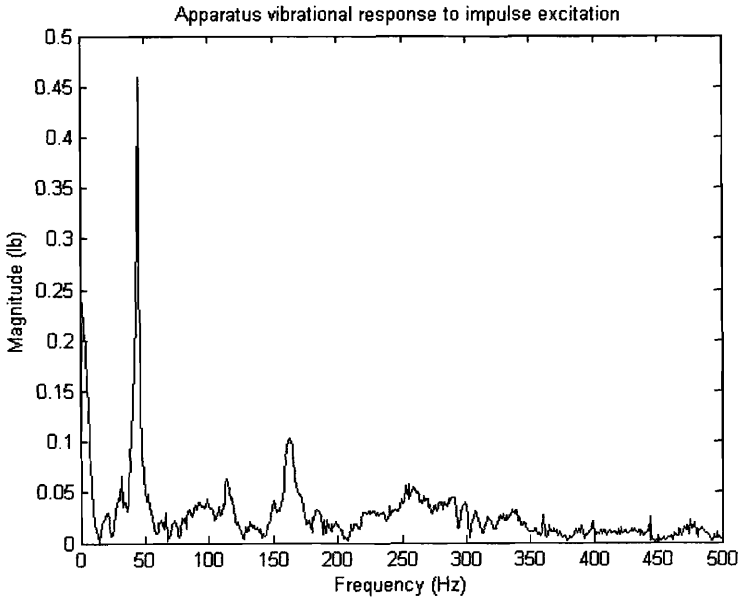

Figure 3-9: Vibrational response in water due to an impulse excitation in the x direction.

Figure 3-10 shows the force spectra of the propellers in figure 3-8. These graphs represent the discrete fourier transforms of raw unfiltered force measurements. The upper graphs showing the response of three-bladed propellers display peaks corresponding to the 3rd, 6th, and 9th shaft harmonics. These correspond to the 1st, 2nd, and 3rd blade harmonics. The two-blades propellers also show peaks at the first four blade harmonics which correspond to the 2nd, 4th, 6th, and 8th shaft harmonics. When comparing active stator flapping to the baseline wake, attention is concentrated on the relative magnitudes of these harmonic peaks.

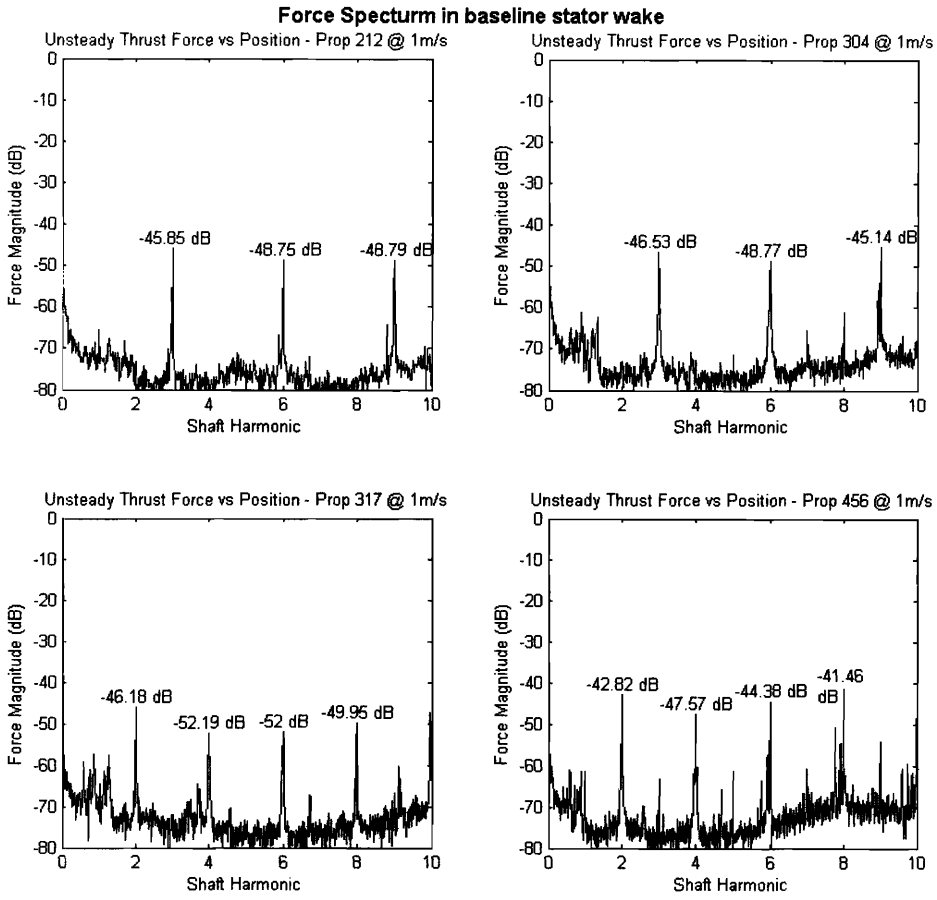

Figure 3-10: Unsteady thrust force spectra for propellers in baseline stator wake

The temporal derivative of both the phase-averaged force and the spectrum data are shown in figures 3-11 and 3-12. Similar patterns emerge in these figures. Patterns can be seen that repeat two or three times per cycle depending on the number of blades. The discrete fourier transform shows repeating harmonics based on the blade rate as was seen in the original force data.

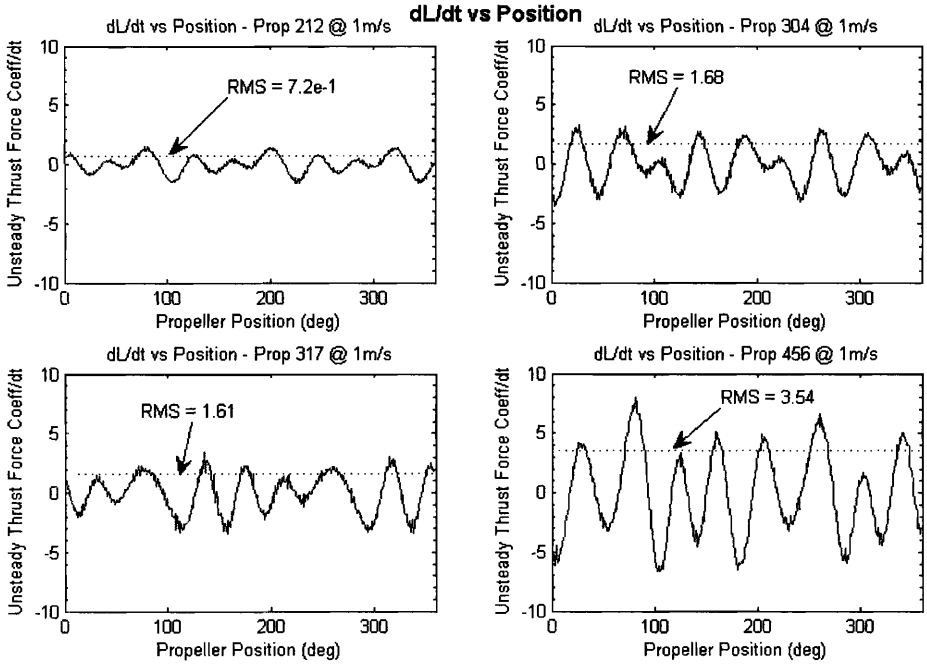

Figure 3-11: Time derivative of the measured thrust force coefficient for various propellers in baseline stator wake.

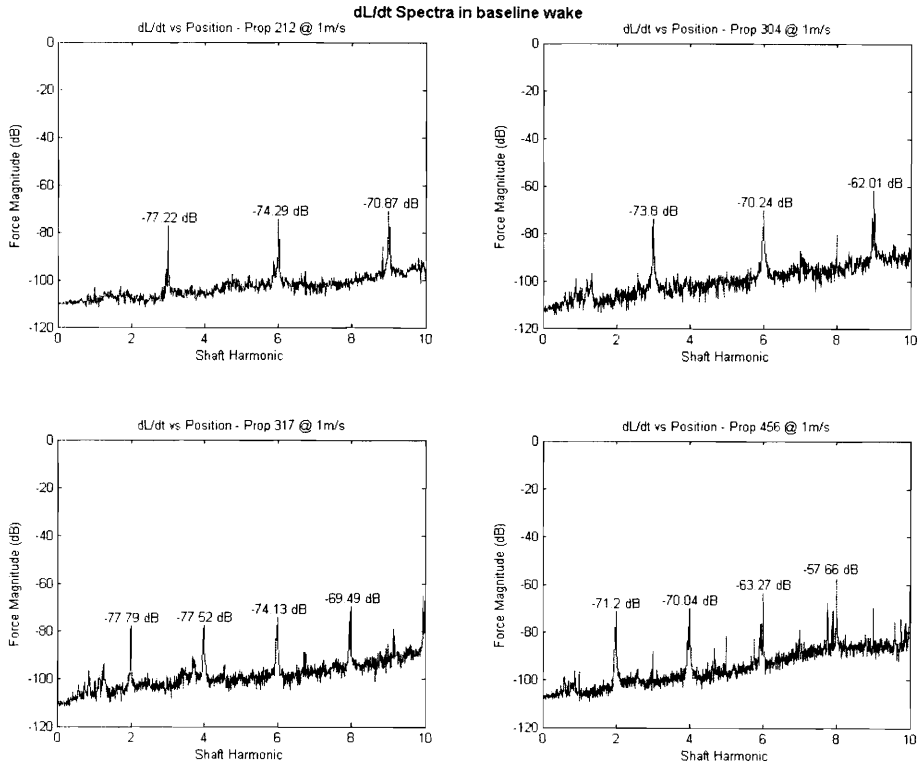

Figure 3-12: Discrete fourier transform of the temporal derivative of measured thrust data.

Chapter 4

Propellers forces due to active wake

This section discusses the force measurements recorded from propellers spinning downstream of an articulating stator.

4.1 Tail Articulation

This experimental study looked at sinusoidal stator tail articulation. The stator tail is articulated by means of a servo motor driving a rotary linkage. The articulation amplitude can be adjusted by means of tapped holes in the rotary linkage. For every full rotation of the servo motor the stator completes one oscillation. The servo motor is commanded to spin at a rate so that one full stator oscillation occurs for every blade passing. The stator motor and propeller motors are controlled by a NI motion controller so that their positions and velocities are synchronized in the proper ratio. The phase between the propeller and the stator is defined as the position the stator is within its oscillation when a propeller blade crosses the wake. For every propeller tested at each of the three flapping amplitudes, the phase of the stator is varied from 0° to 360°.

4.2 Unsteady Forces due to Active Wake

Figures 4-1 through 4-12 show the measured unsteady thrust force data for all the propellers tested at 2°, 5°, and 10° amplitudes. Each figure shows the measured unsteady thrust force versus position at each phase angle tested. In each three-

dimensional view, the dotted line shows the thrust force of the baseline unarticulated wake. The RMS of the thrust force for each phase angle is shown in the lower right of each figure.

Observing these figures it becomes apparent that stator articulation had a significant effect on the measured propeller thrust forces. As expected the effect of tail articulation on each propeller depends on the amplitude of tail articulation and the phase angle between the stator and blade crossing. One can see that there are certain phases where the RMS of the unsteady thrust force is greater than the baseline stator wake and others where it is reduced. Tail articulation shifts the angular position of the force peaks corresponding to the wake crossing. The graphs in the lower left of each figure show how the position and amplitude of the unsteady thrust force changes with stator phase angle.

In figure 4-1 one sees a significant break in the force pattern generated by propeller A, occuring between 240°-260°. At this phase angle the RMS of the unsteady thrust is much lower than the RMS thrust in the baseline wake. In figure 4-2 there is a similar pattern at 220°-240° where the unsteady RMS thrust force is also reduced. In this figure, however, at 5° amplitude, certain phase angles show a more significant increase in the RMS thrust force than at 2° amplitude. 10° flapping, shown in figure 4-3, results in greater RMS unsteady thrust force across the whole phase space. Interestingly, for this flapping case, between 180° and 220° there is a local minimum in the unsteady thrust RMS. Another local minimum occurs between 60° and 80°. Local maxima occur at 120° and 320°. The extrema are separated by approximately 200° phase. Figures 4-4 through 4-6 show the recorded force data for propeller B at 304 rpm. 5° and 10° flapping amplitudes show local minima and maxima that are separated by approximately 200°. The extrema are located at the same phase angle for both flapping amplitudes. As with propeller A, 10° shows an increase in RMS unsteady thrust across the complete phase range. 5° flapping amplitude in figure 4-5 shows phases RMS where the RMS unsteady propeller force is significantly reduced as in figure 4-1. Propellers C and D,seen in figures 4-7 to 4-12, are two-bladed. They show similar behavior as propellers A and B. 5° and 10° amplitudes show local extrema approximately 200° part in phase angle. 10° amplitudes show increases in RMS thrust across the phase range.

Figures 4-13 through 4-24 show the instantaneous rate of change of thrust with respect to time in the same manner as the previous set of figures. The time derivative of the thrust force displays almost the identically the same patterns as the unsteady thrust force with respect to phase, propeller speed and flapping amplitude.

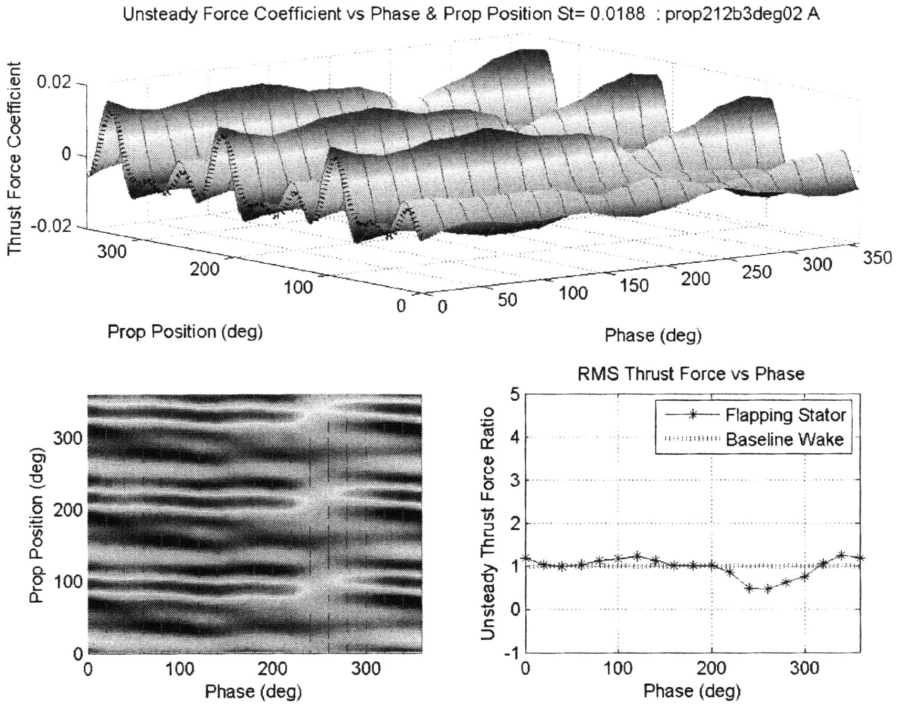

Figure 4-1: Propeller 212 RPM @ 1m/s, 2° flapping amplitude, $St = 0.0187$

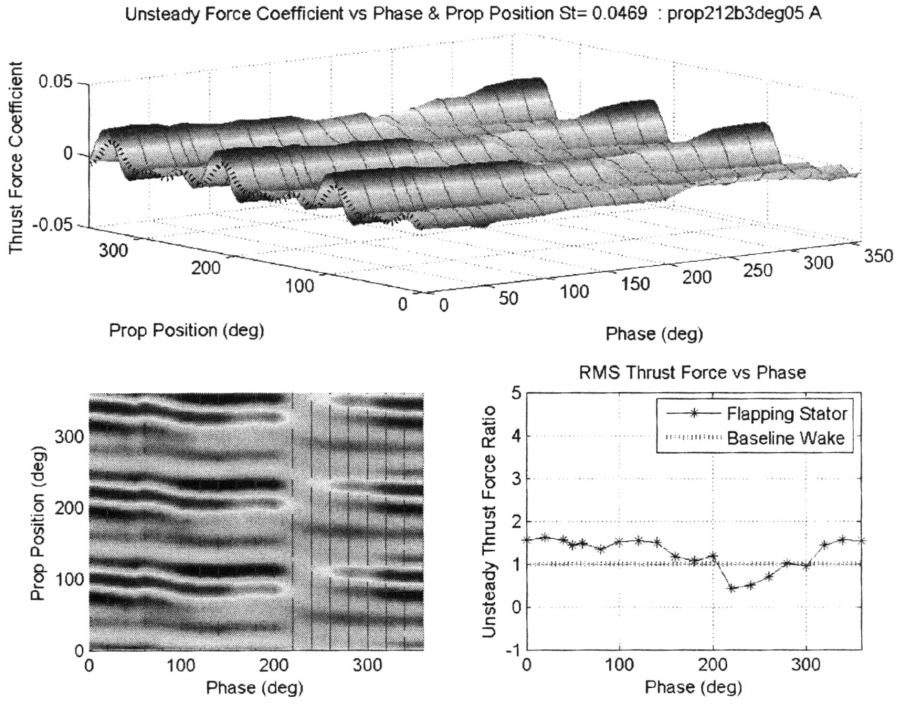

Figure 4-2: Propeller 212 RPM @ 1m/s, 5° flapping amplitude, $St = 0.0468$

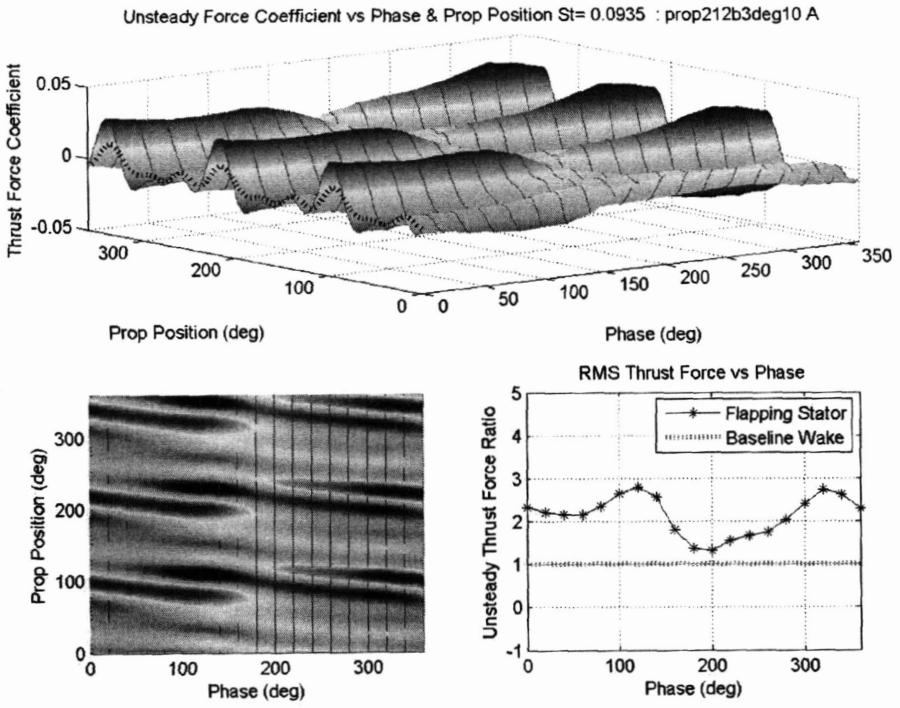

Figure 4-3: Propeller 212 RPM @ 1m/s, 10° flapping amplitude, $St = 0.0932$

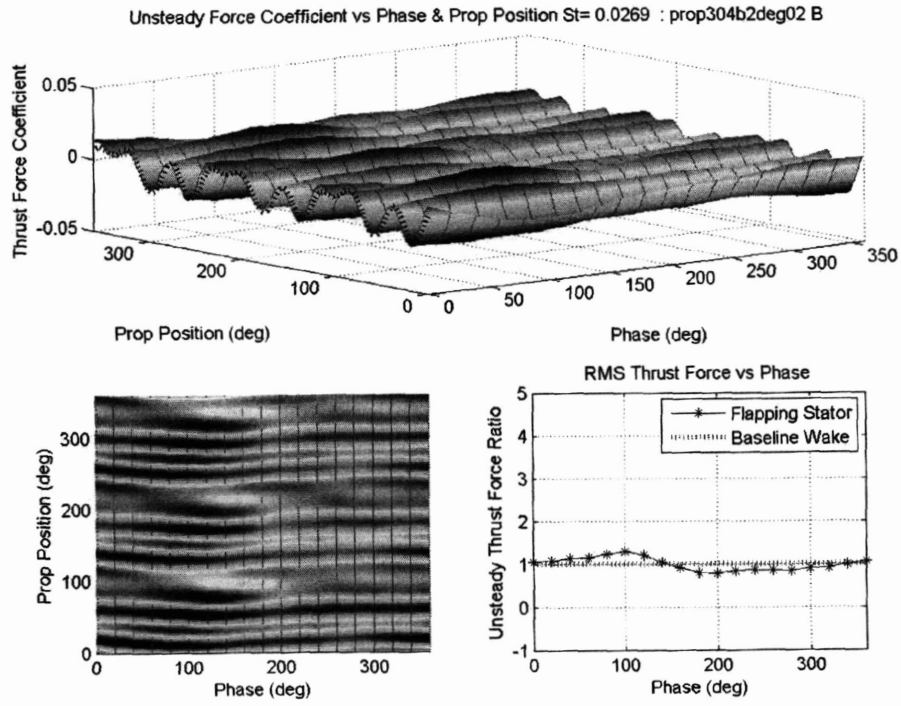

Figure 4-4: Propeller 304 RPM @ 1m/s, 2° flapping amplitude, $St = 0.0269$

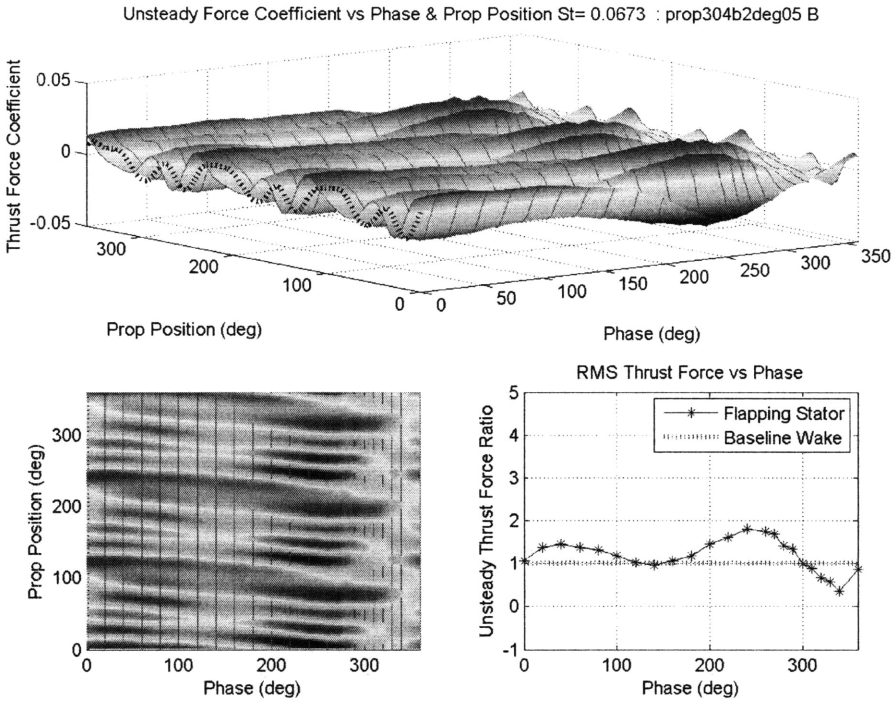

Figure 4-5: Propeller 304 RPM @ 1m/s, 5° flapping amplitude, $St = 0.0673$

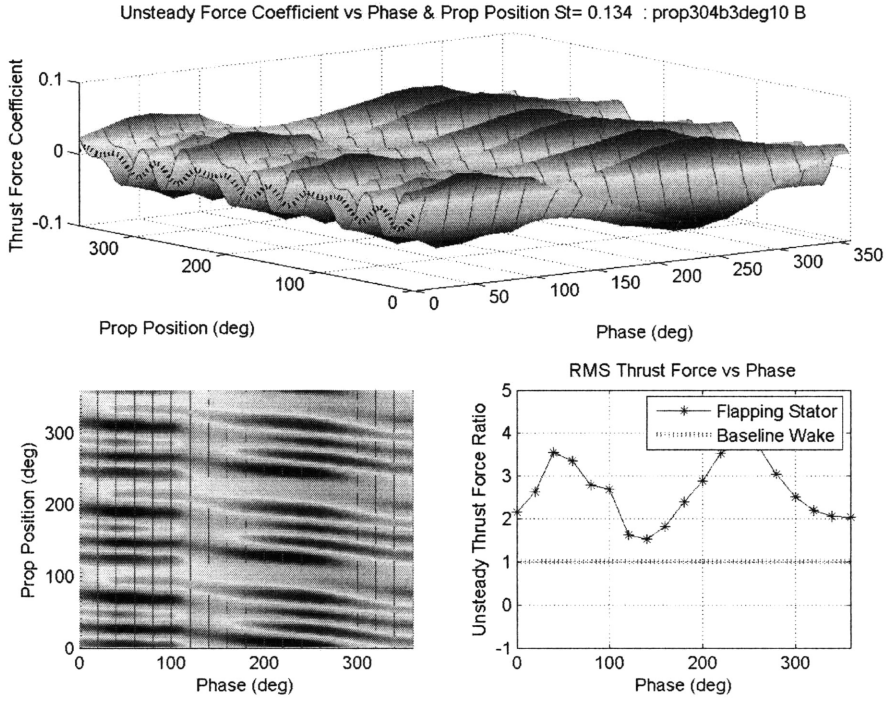

Figure 4-6: Propeller 304 RPM @ 1m/s, 10° flapping amplitude, $St = 0.1341$

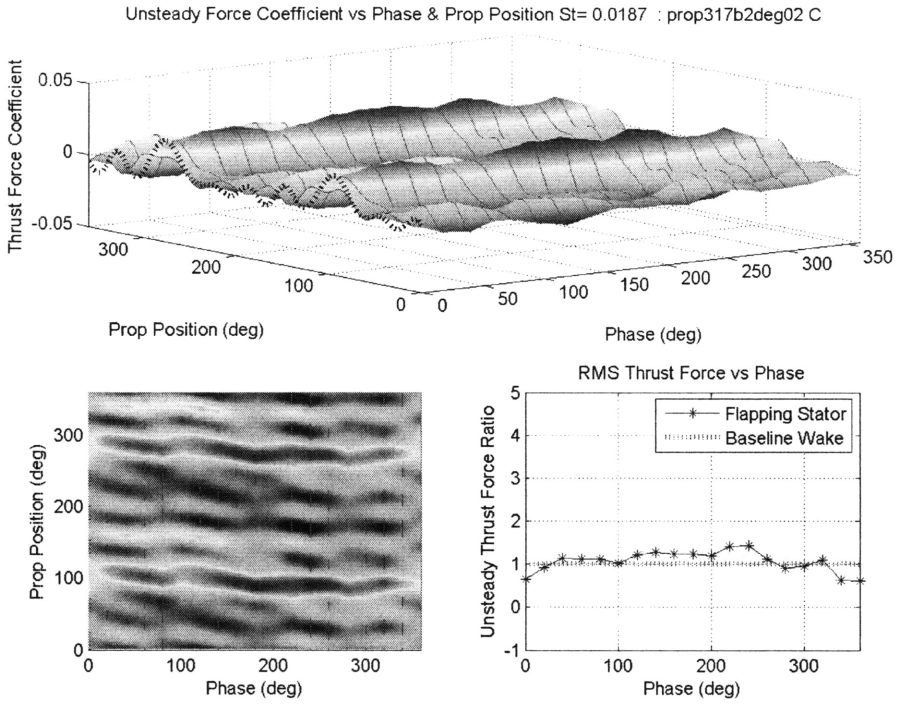

Figure 4-7: Propeller 317 RPM @ 1m/s, 2° flapping amplitude, $St = 0.0187$

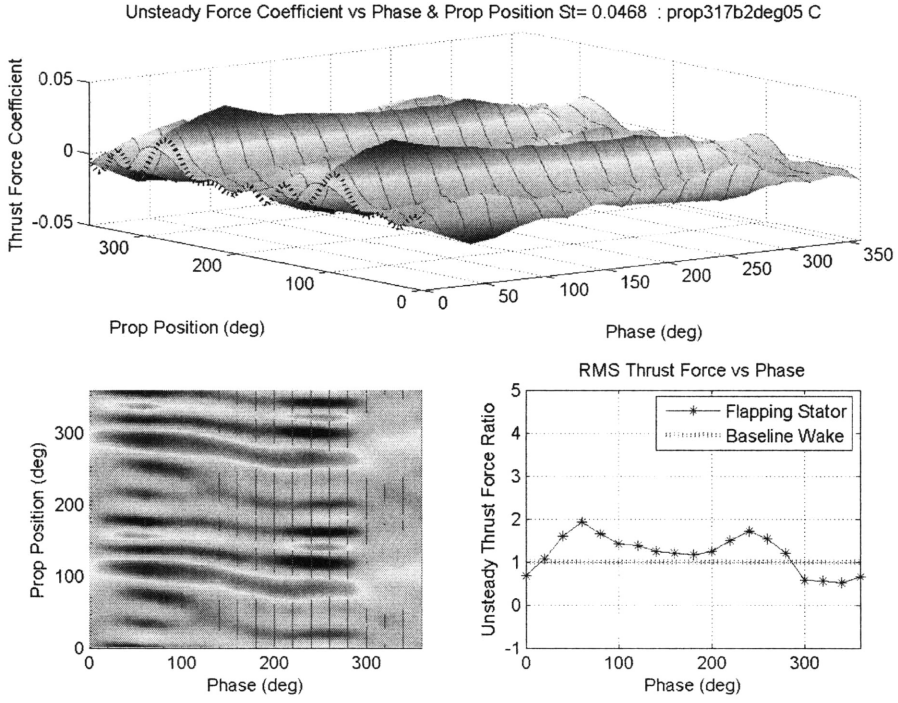

Figure 4-8: Propeller 317 RPM @ 1m/s, 5° flapping amplitude, $St = 0.0468$

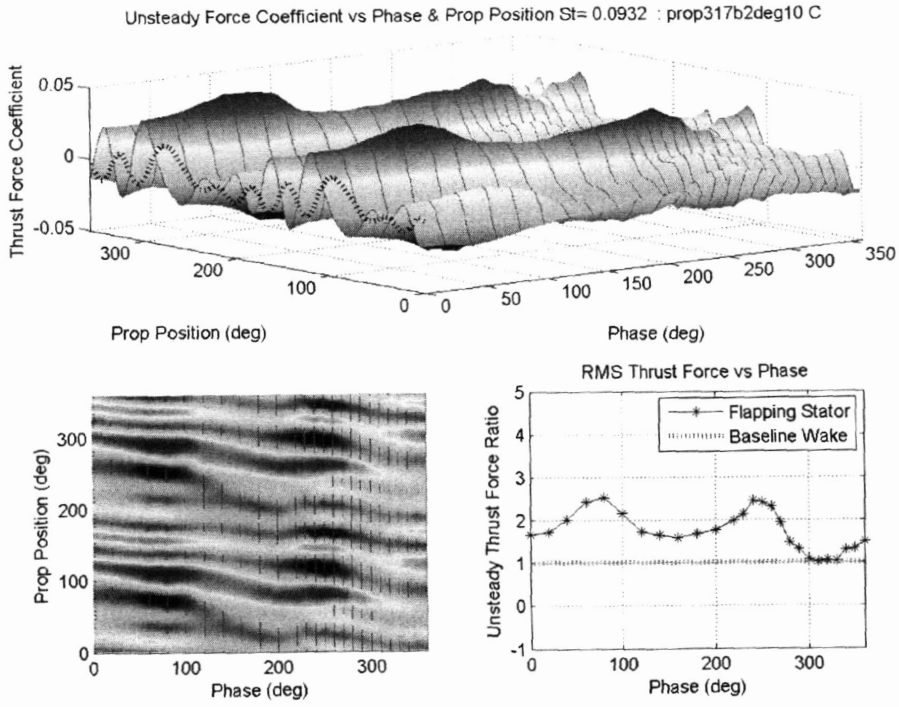

Figure 4-9: Propeller 317 RPM @ 1m/s, 10° flapping amplitude, $St = 0.0932$

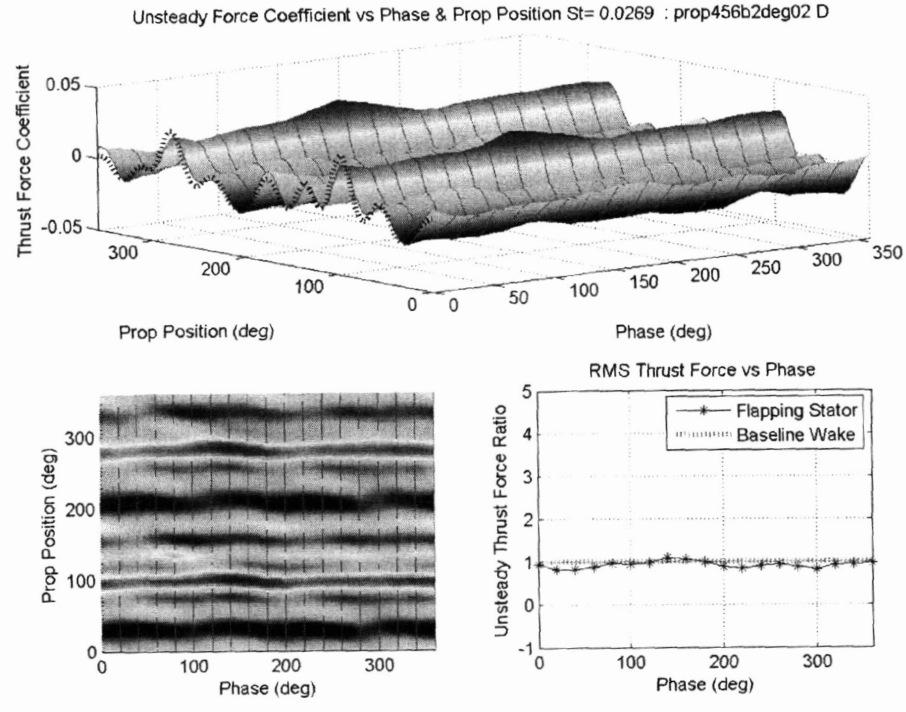

Figure 4-10: Propeller 456 RPM @ 1m/s, 2° flapping amplitude, $St = 0.0269$

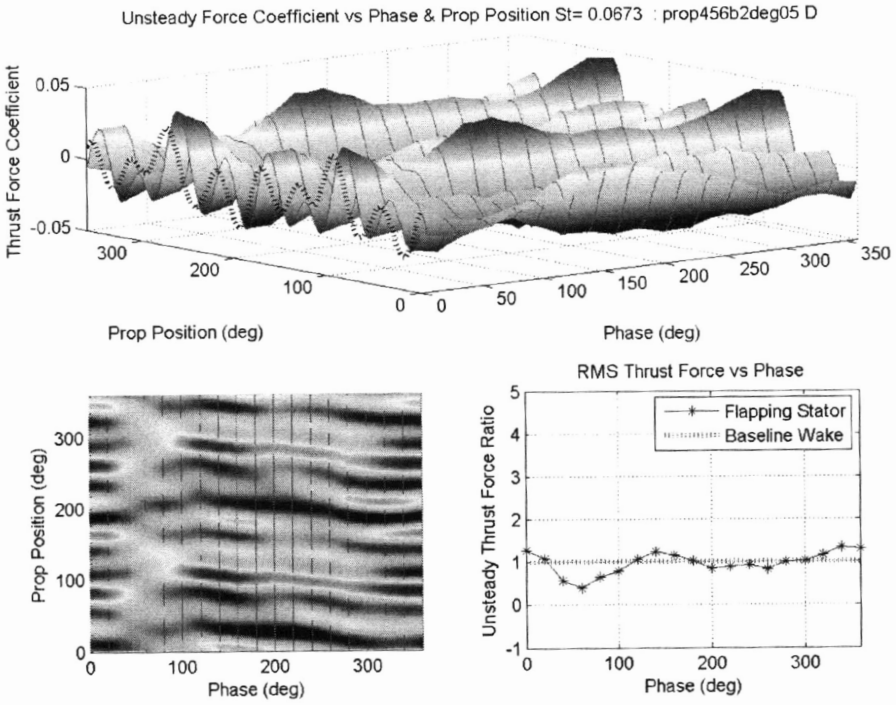

Figure 4-11: Propeller 456 RPM @ 1m/s, 5° flapping amplitude, $St = 0.0673$

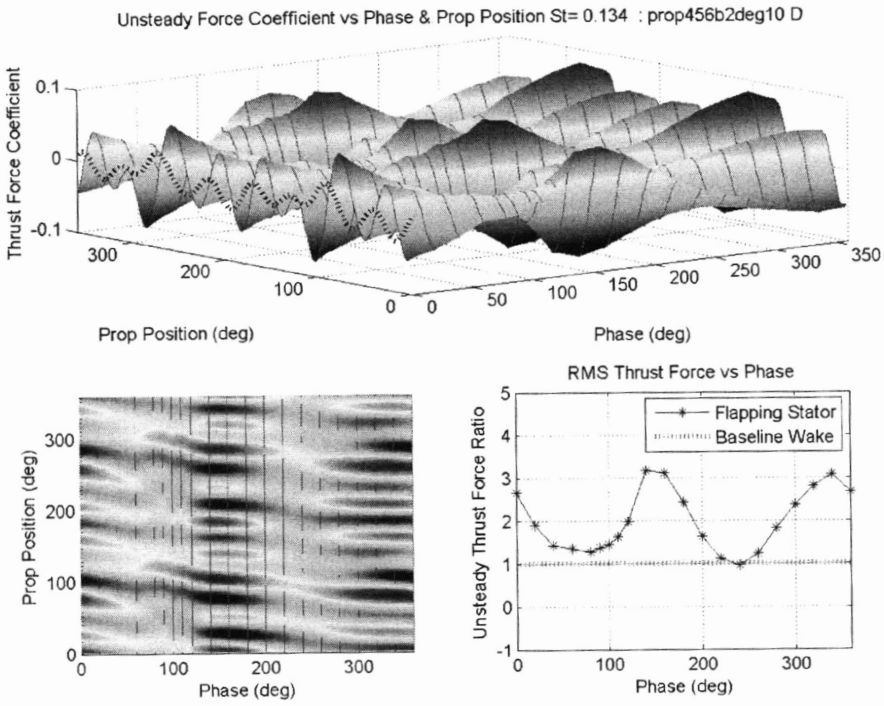

Figure 4-12: Propeller 456 RPM @ 1m/s, 10° flapping amplitude, $St = 0.1341$

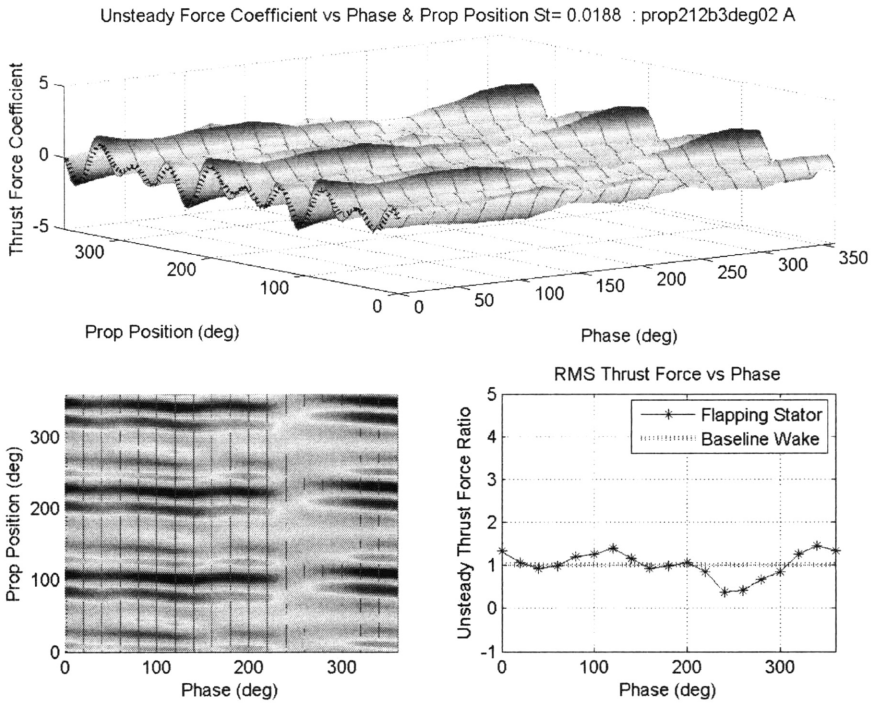

Figure 4-13: Thrust derivative w.r.t. time: Propeller 212 RPM @ 1m/s, 2° flapping amplitude, $St = 0.0187$

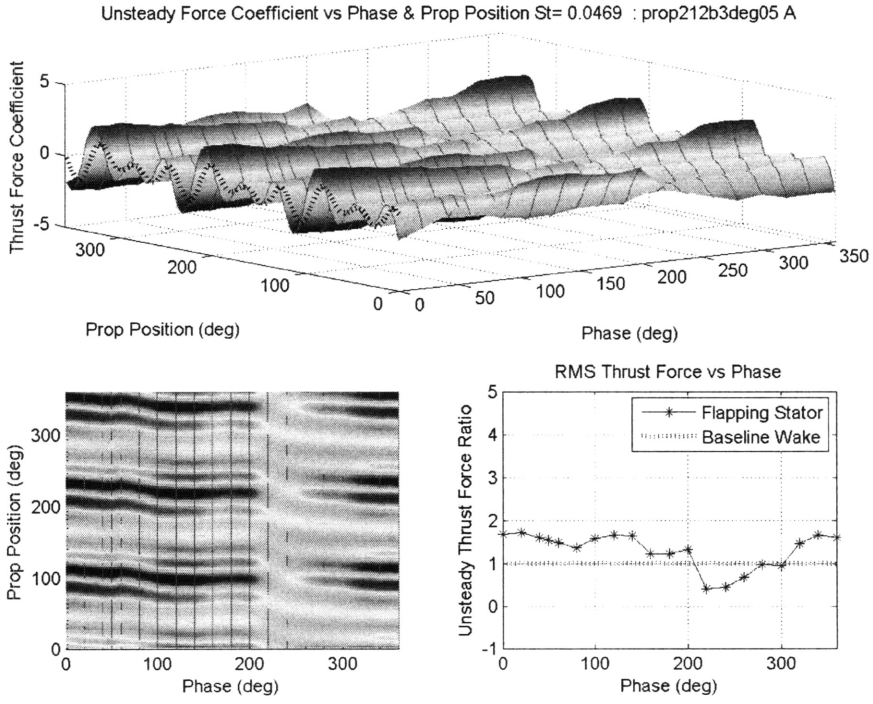

Figure 4-14: Thrust derivative w.r.t. time: Propeller 212 RPM @ 1m/s, 5° flapping amplitude, $St = 0.0468$

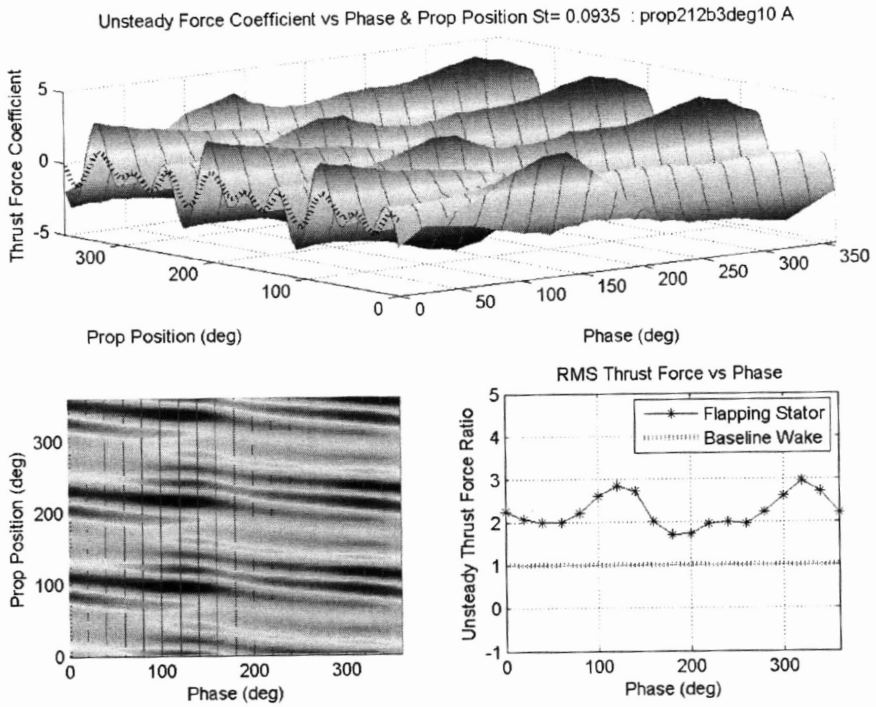

Figure 4-15: Thrust derivative w.r.t. time: Propeller 212 RPM @ 1m/s, 10° flapping amplitude, $St = 0.0932$

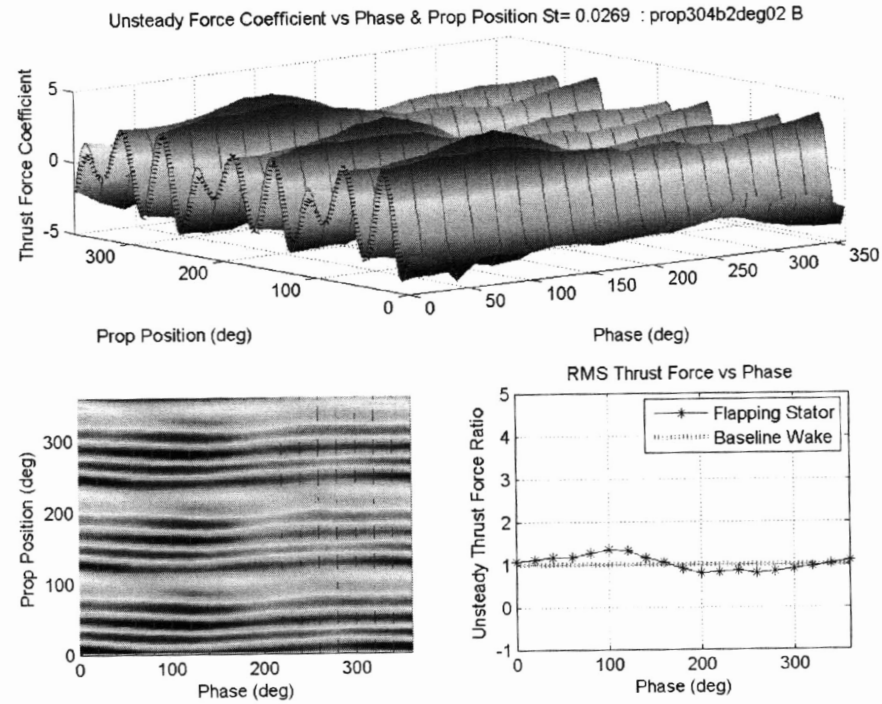

Figure 4-16: Thrust derivative w.r.t. time: Propeller 304 RPM @ 1m/s, 2° flapping amplitude, $St = 0.0269$

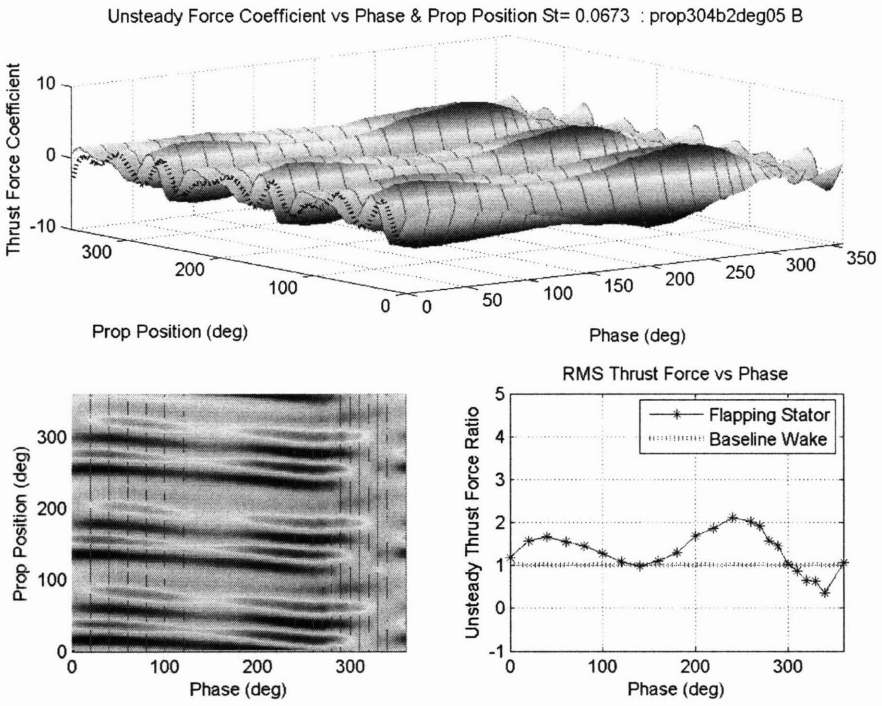

Figure 4-17: Thrust derivative w.r.t. time: Propeller 304 RPM @ 1m/s, 5° flapping amplitude, $St = 0.0673$

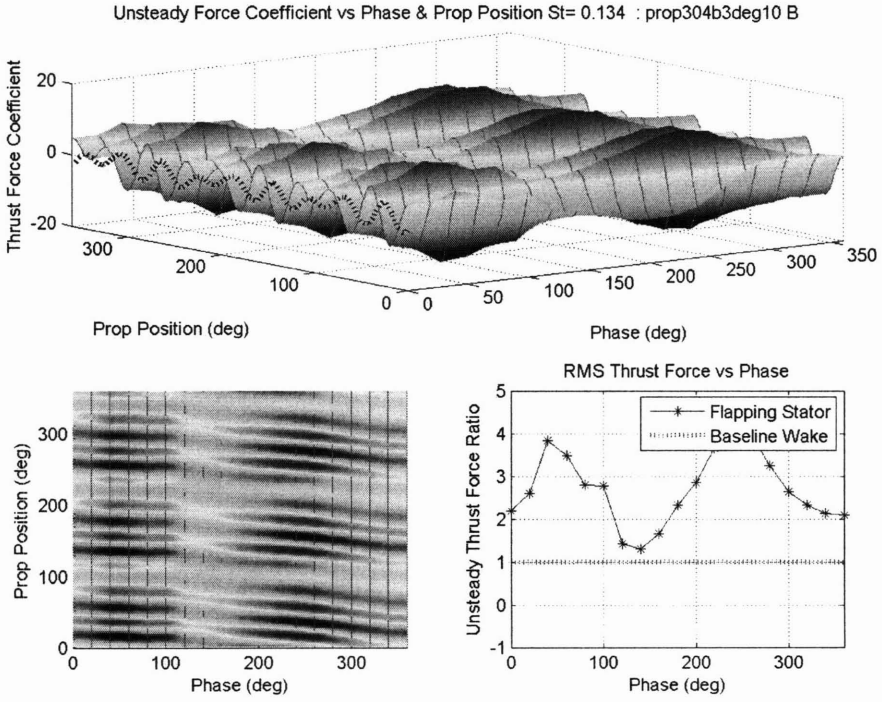

Figure 4-18: Thrust derivative w.r.t. time: Propeller 304 RPM @ 1m/s, 10° flapping amplitude, $St = 0.1341$

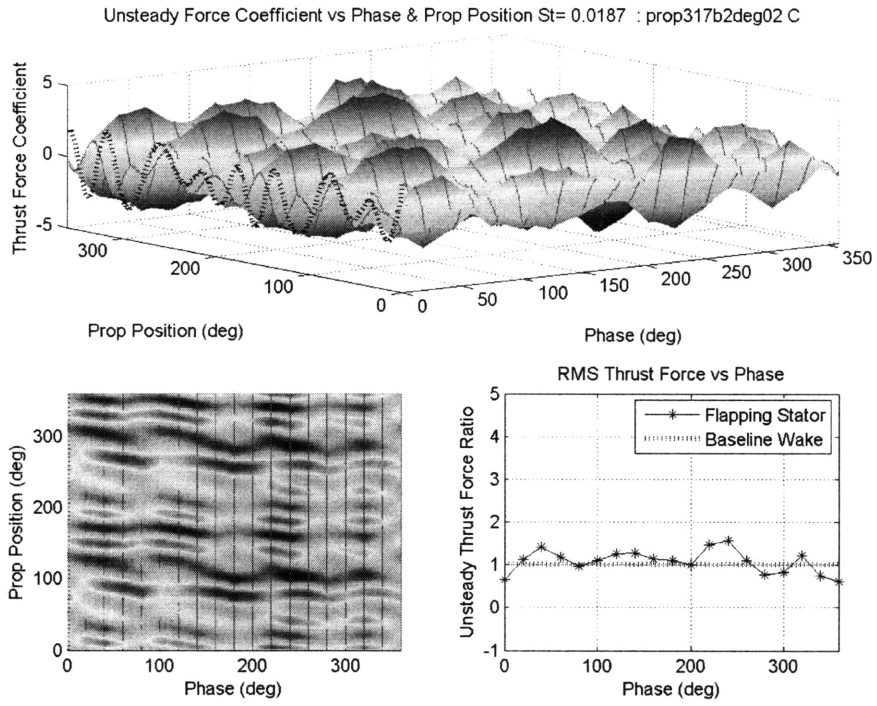

Figure 4-19: Thrust derivative w.r.t. time: Propeller 317 RPM @ 1m/s, 2° flapping amplitude, $St = 0.0187$

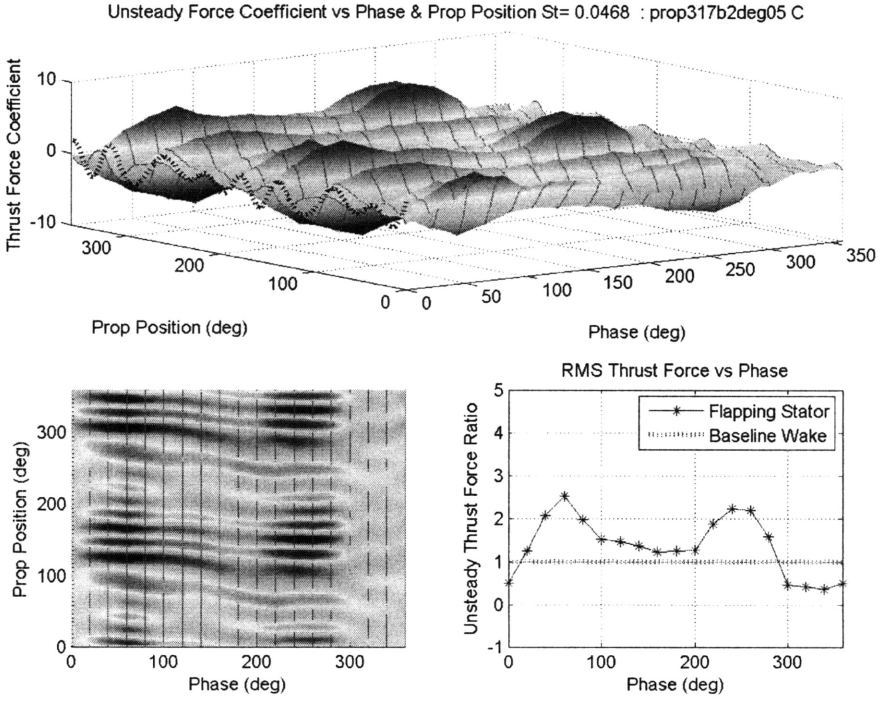

Figure 4-20: Thrust derivative w.r.t. time: Propeller 317 RPM @ 1m/s, 5° flapping amplitude, $St = 0.0468$

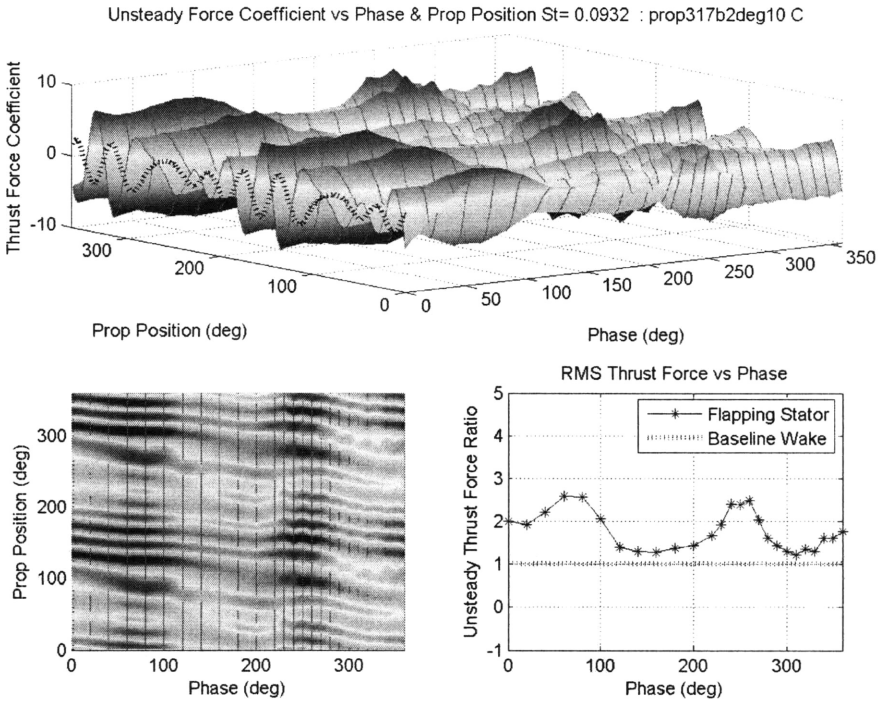

Figure 4-21: Thrust derivative w.r.t. time: Propeller 317 RPM @ 1m/s, 10° flapping amplitude, $St = 0.0932$

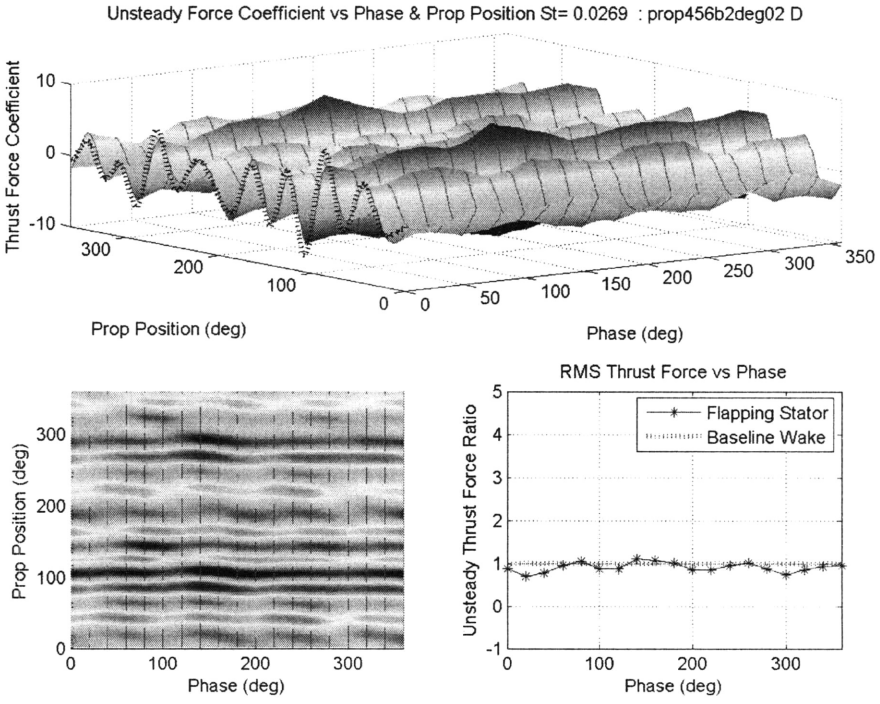

Figure 4-22: Thrust derivative w.r.t. time: Propeller 456 RPM @ 1m/s, 2° flapping amplitude, $St = 0.0269$

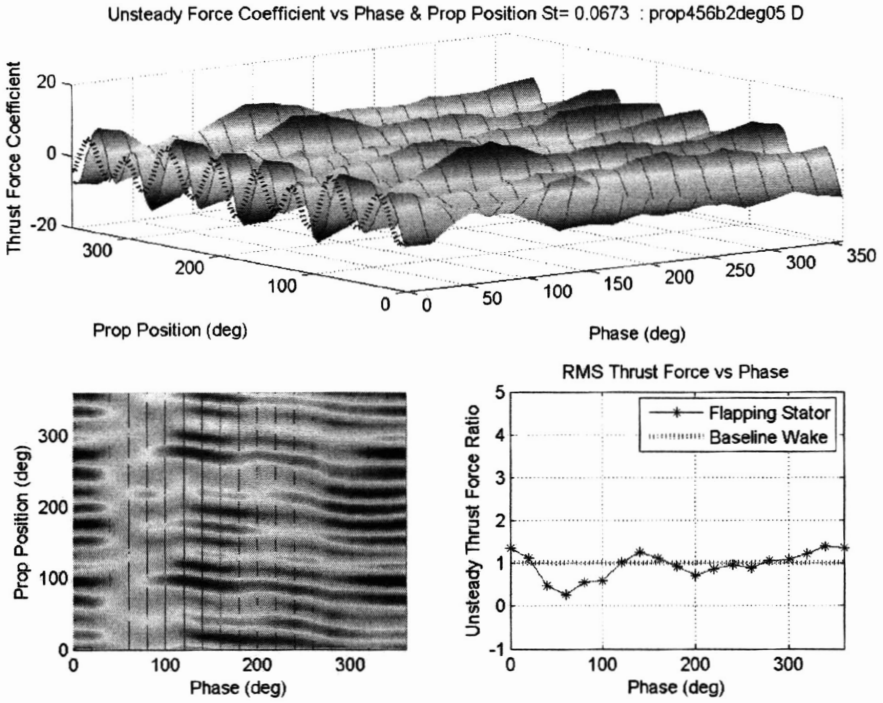

Figure 4-23: Thrust derivative w.r.t. time: Propeller 456 RPM @ 1m/s, 5° flapping amplitude, $St = 0.0673$

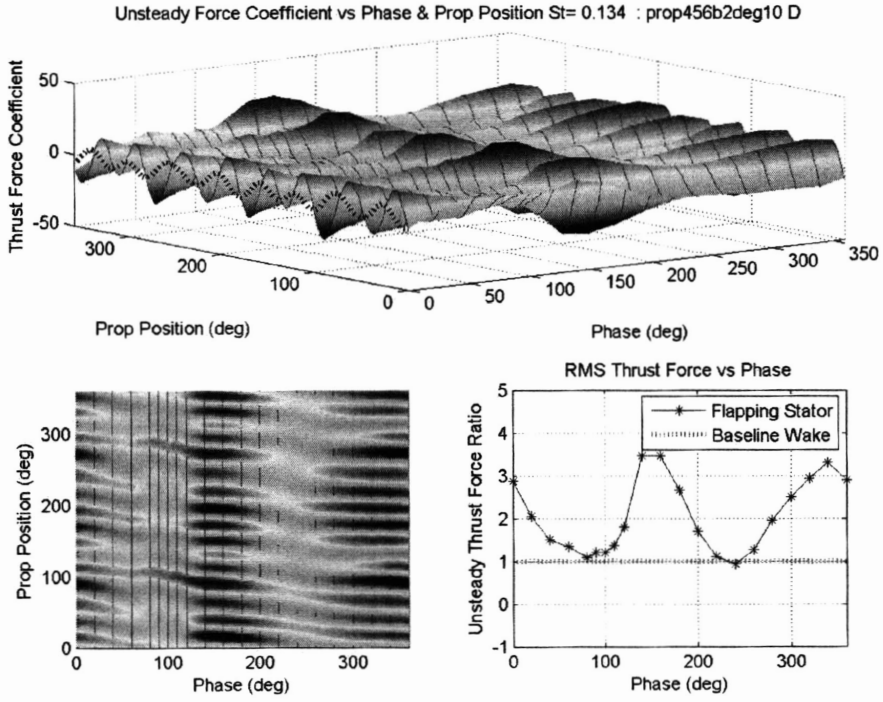

Figure 4-24: Thrust derivative w.r.t. time: Propeller 456 RPM @ 1m/s, 10° flapping amplitude, $St = 0.1341$

4.3 Unsteady Force Spectra

Figures 4-25 through 4-36 show the discrete transform (dfft) of the unsteady thrust force due the baseline wake and of those articulated cases exhibiting the largest and smallest RMS unsteady force. In the upper portion of figure 4-26, the magnitude of all four blade rate harmonics is smaller than for the baseline wake. The highest RMS thrust case in the middle of the figure shows in increase in all four blade rate harmonics over the baseline wake. The largest unsteady thrust force in figure 4-27 shows the four blade harmonics with a larger magnitude than those in the baseline wake case. The lowest thrust phase case in the upper portion of figure 4-27 shows a decrease in the magnitude of the first blade harmonic over the baseline case. Other harmonics show an increase in magnitude over the baseline wake case. This was expected since at this flapping amplitude, all phase angle scenarios showed an increase over the baseline wake. In figure 4-29, once again, the highest RMS unsteady thrust case shows that the first three blade harmonics are greater in magnitude than in the baseline wake case. The first blade harmonic of the lowest RMS thrust case is smaller in magnitude than the baseline case. The higher order magnitudes however are greater in magnitude. Figure 4-30 similarly shows that the lowest RMS thrust case sees a lower magnitude in the first blade harmonic over the baseline wake while higher order harmonics have a greater magnitude. In this test case however, even at the minimum thrust phase angle, stator articulation creates a higher RMS unsteady thrust than the baseline wake. The highest thrust phase angle case shown in the middle of figure 4-30 has a higher magnitude for all the blade rate harmonics. In figure 4-31 one sees an decrease in all the blade rate harmonics over the baseline wake for the lowest RMS thrust force case. The highest RMS thrust force case shows the magnitude of all blade rate harmonics increasing as expected. Figure 4-32 shows identical behavior. Figure 4-33 shows a decrease in the first and second blade rate harmonics for the lowest RMS thrust case over the baseline wake. The highest RMS thrust force case shows a greater magnitude for all the blade rate harmonics over the baseline case. Figure 4-34 shows little difference in blade harmonic amplitude of the lowest RMS thrust case as compared with the baseline wake. The highest unsteady force phase angle shows a magnitude increase of the second and third blade harmonics. Figure 4-35 shows an increased magnitude of the second and third blade harmonics for the highest unsteady force case. The lowest RMS force case shows decreased magnitude of the first through third blade harmonics. The third harmonic shows a significant magnitude reduction. Lastly, in figure 4-36 there is a significant

increase in the magnitude of the first three blade harmonics in the highest unsteady thrust force case. The lowest unsteady thrust case sees a increase in the magnitude of the first and third blade harmonics. The second blade harmonic, however sees a significant increase in magnitude.

4.4 Unsteady Forces and Strouhal Number

Figures 4-49 and 4-50 show the RMS thrust and RMS thrust derivative versus phase angle for each propeller. The time derivative of the thrust force shows similar patterns versus phase angle. Figure 4-51 shows the smallest RMS thrust ratio for each propeller at each flapping amplitude versus St. For a St smaller than 0.08 the smallest RMS thrust ratio for each propeller is smaller than unity, in other words for a certain phase angle it is possible to obtain a smaller unsteady thrust than the baseline wake. For St greater than 0.08 the smallest RMS thrust ratio is greater than unity, so stator articulation always produces greater unsteady forces. The data points at $St > 0.08$ correspond to 10° flapping amplitudes which showed no decrease in RMS thrust in figures 4-1 through 4-12. Figure 4-52 shows the greatest RMS thrust ratio for every propeller at each flapping amplitude. Every data point is greater than unity. For every represented case the RMS thrust force is greater than that measured in the baseline wake. The trend in the graph shows that the greatest RMS thrust force for each propeller increases with St number. The same trends are present in the time derivative of the thrust force seen in figures 4-53 and 4-54

The relationship between St number and wake structure is discussed in [5]. As the stator Strouhal number increases, the relative strength of wake vortices increases. The stator reintroduces energy into the wake that was removed by its boundary layer. At high Strouhal numbers the stator can recover its own drag penalty and create net thrust. At a Strouhal number of approximately 0.1 the stator is re-energizing the flow to fill in its own wake defect (in a time-mean sense). At these Strouhal numbers however, there are still large instantaneous wake structures that can interact with an impinging propeller blade. This explains why unsteady propeller forces are greater at these Strouhal numbers; there will be local regions of velocity defect and regions where the wake velocity is actually greater than the free stream velocity.

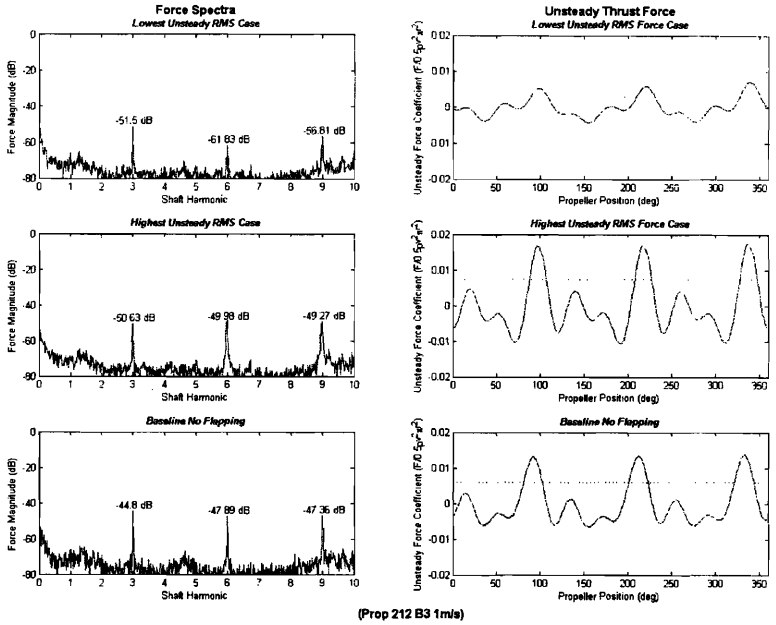

Figure 4-25: Discrete Fourier Transform of the highest, lowest and baseline RMS thrust force cases for propeller A (212RPM), 2° amplitude @ 1m/s

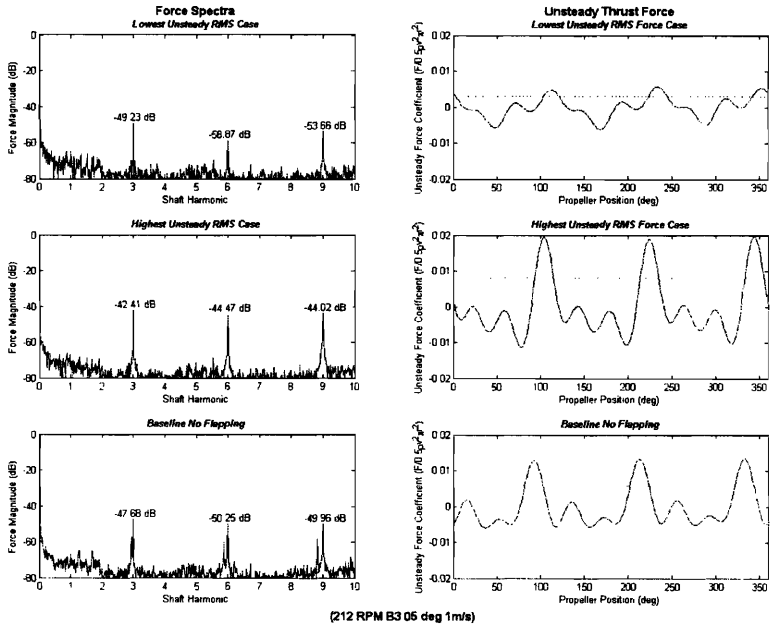

Figure 4-26: Discrete Fourier Transform of the highest, lowest and baseline RMS thrust force cases for propeller A (212RPM), 5° amplitude @ 1m/s

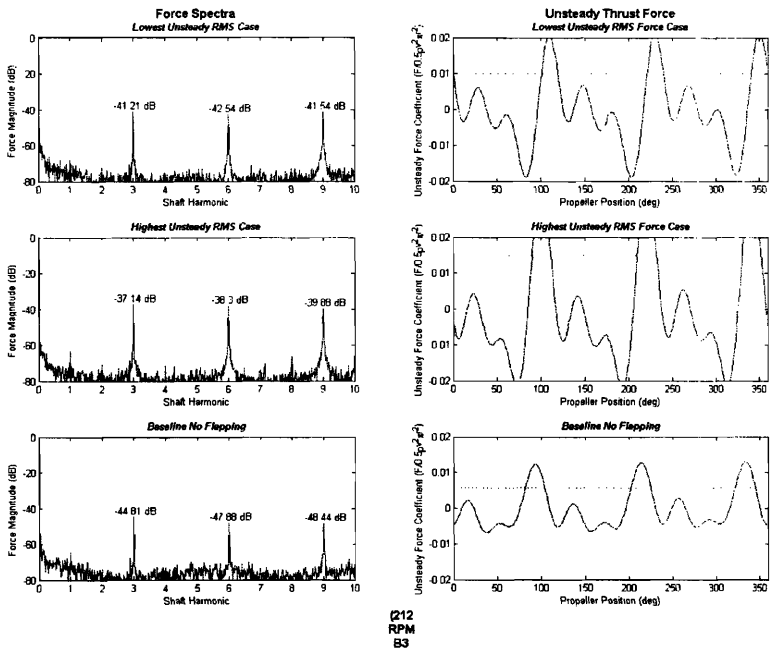

Figure 4-27: Discrete Fourier Transform of the highest, lowest and baseline RMS thrust force cases for propeller A (212RPM), 10° amplitude @ 1m/s

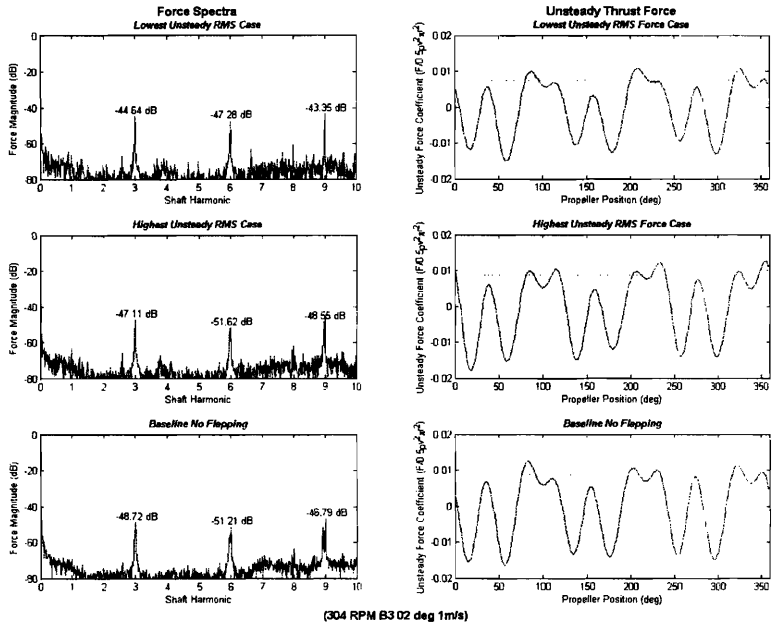

Figure 4-28: Discrete Fourier Transform of the highest, lowest and baseline RMS thrust force cases for propeller B (304RPM), 2° amplitude @ 1m/s

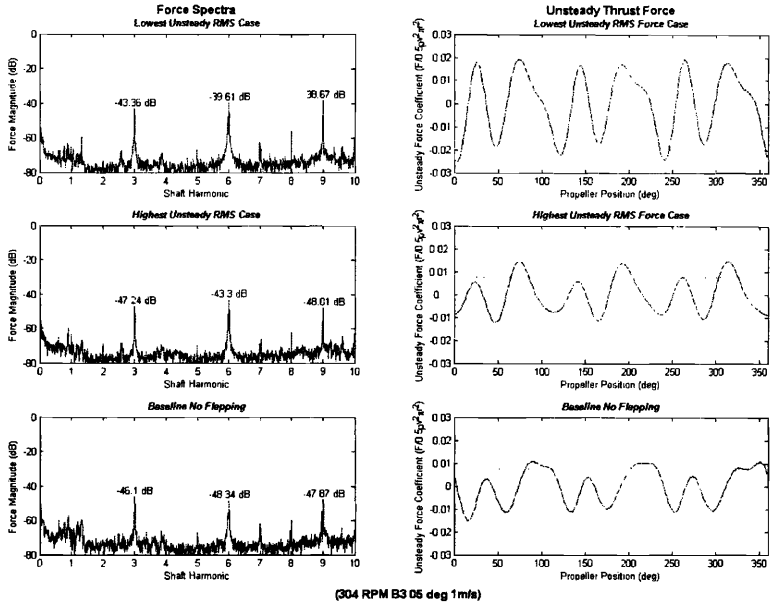

Figure 4-29: Discrete Fourier Transform of the highest, lowest and baseline RMS thrust force cases for propeller B (304RPM), 5° amplitude @ 1m/s

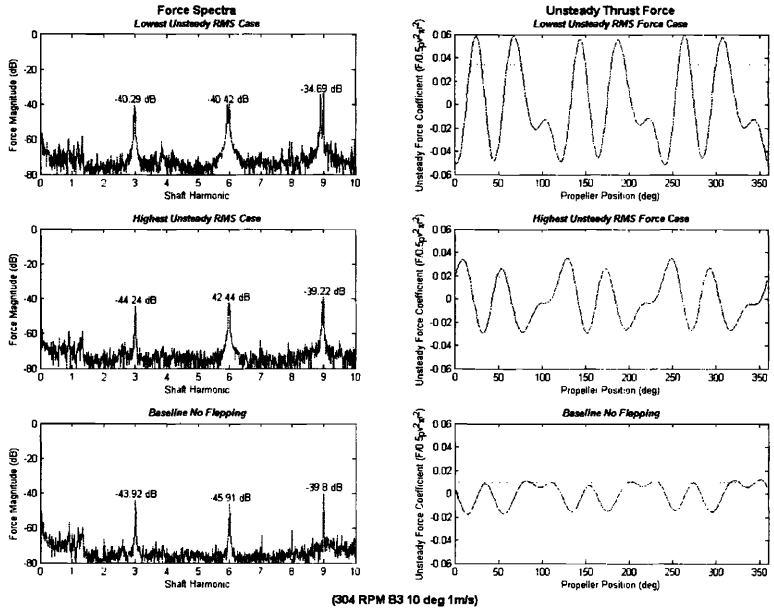

Figure 4-30: Discrete Fourier Transform of the highest, lowest and baseline RMS thrust force cases for propeller C (304RPM), 10° amplitude @ 1m/s

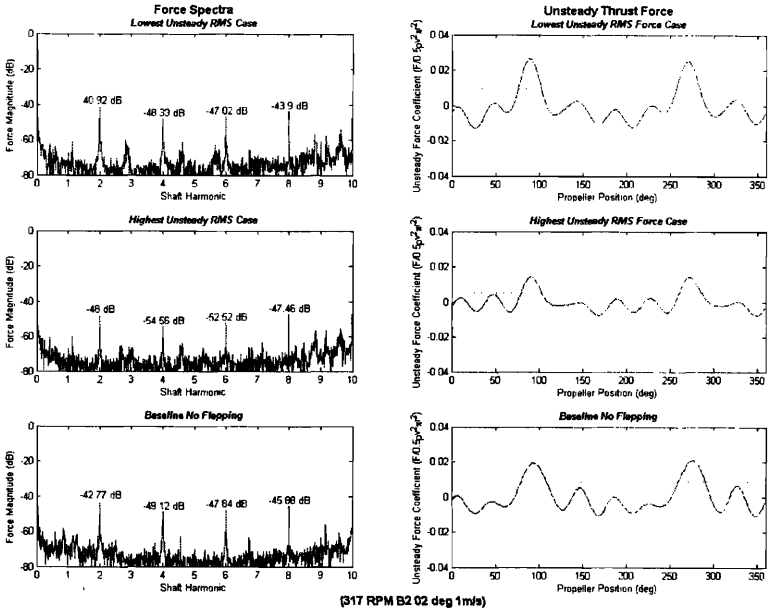

Figure 4-31: Discrete Fourier Transform of the highest, lowest and baseline RMS thrust force cases for propeller C (317RPM), 2° amplitude @ 1m/s

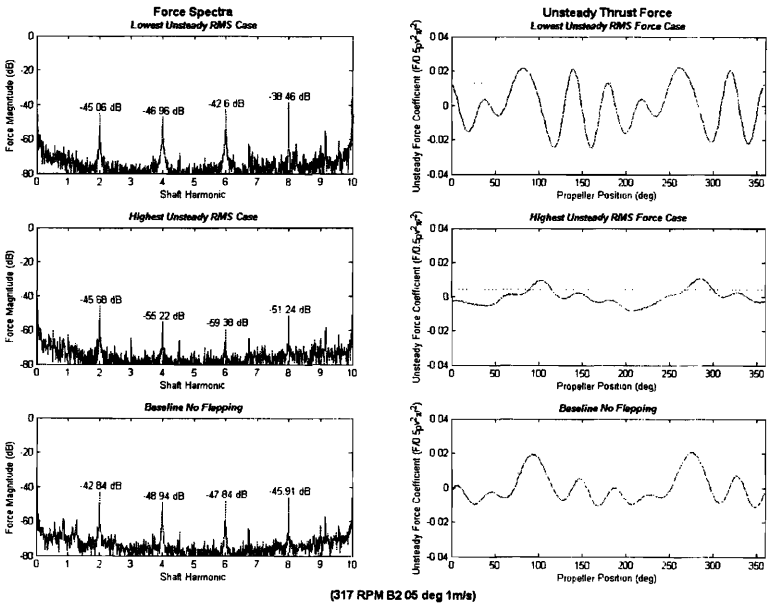

Figure 4-32: Discrete Fourier Transform of the highest, lowest and baseline RMS thrust force cases for propeller C (317RPM), 5° amplitude @ 1m/s

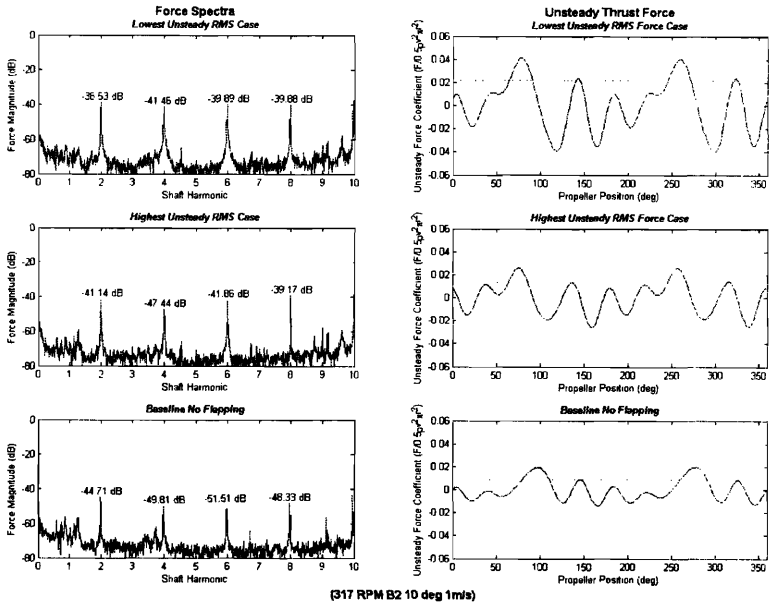

Figure 4-33: Discrete Fourier Transform of the highest, lowest and baseline RMS thrust force cases for propeller C (317RPM), 10° amplitude @ 1m/s

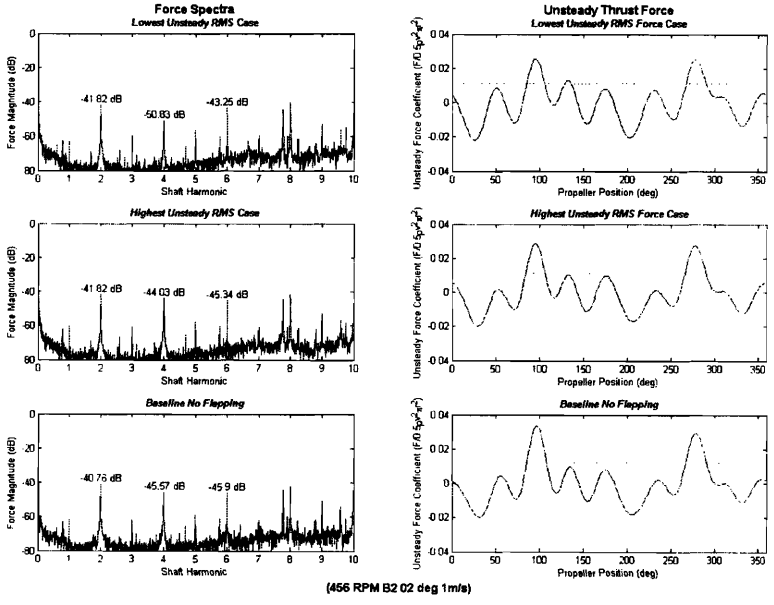

Figure 4-34: Discrete Fourier Transform of the highest, lowest and baseline RMS thrust force cases for propeller D (456RPM), 2° amplitude @ 1m/s

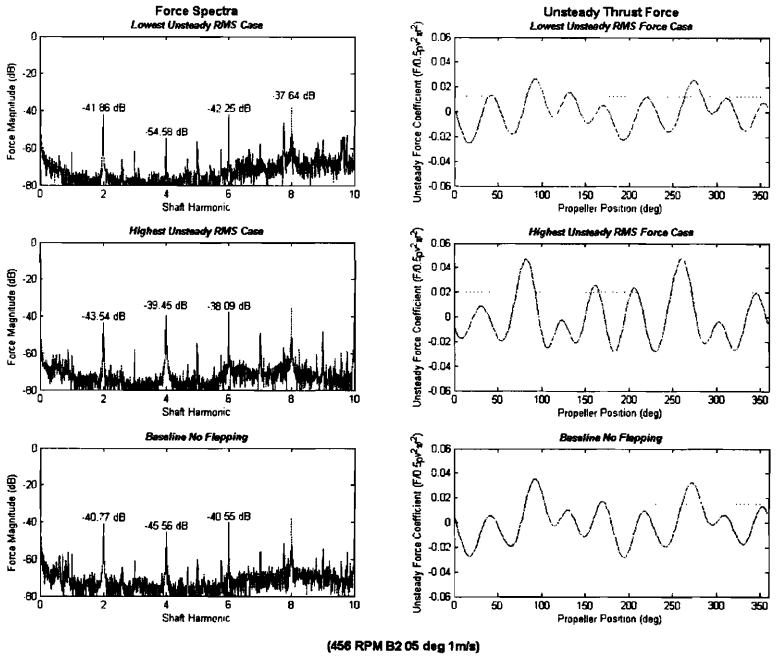

Figure 4-35: Discrete Fourier Transform of the highest, lowest and baseline RMS thrust force cases for propeller D (456RPM), 5° amplitude @ 1m/s

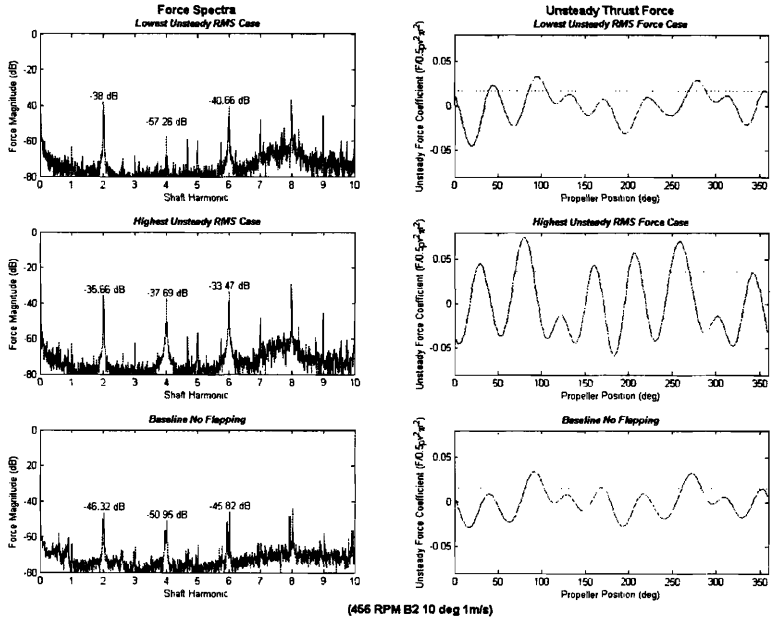

Figure 4-36: Discrete Fourier Transform of the highest, lowest and baseline RMS thrust force cases for propeller D (456RPM), 10° amplitude @ 1m/s

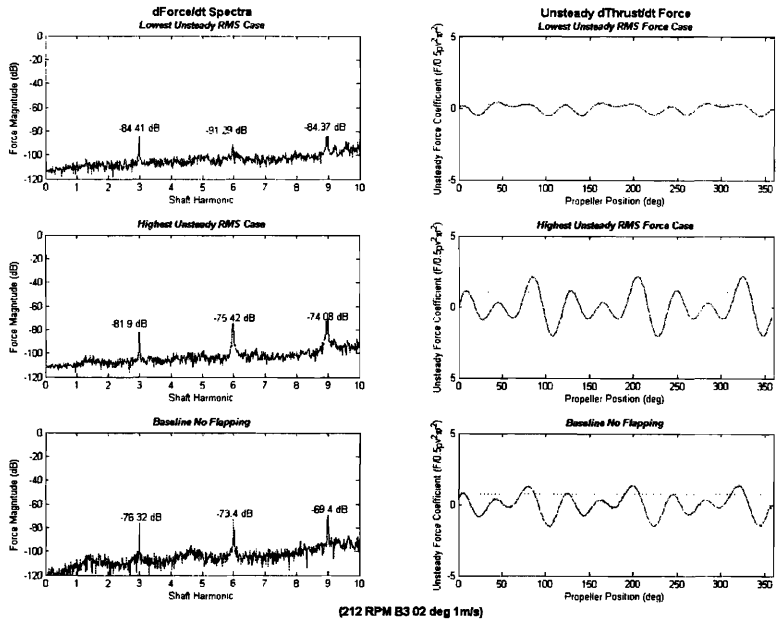

Figure 4-37: Discrete Fourier Transform of the time derivative of the highest, lowest and baseline RMS thrust force cases for propeller A (212RPM), 2° amplitude @ 1m/s

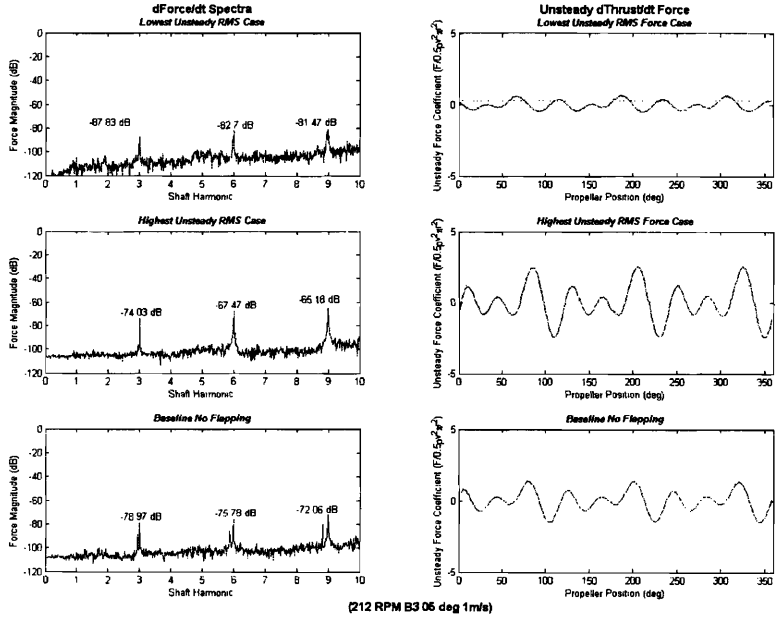

Figure 4-38: Discrete Fourier Transform of the time derivative of the highest, lowest and baseline RMS thrust force cases for propeller A (212RPM), 5° amplitude @ 1m/s

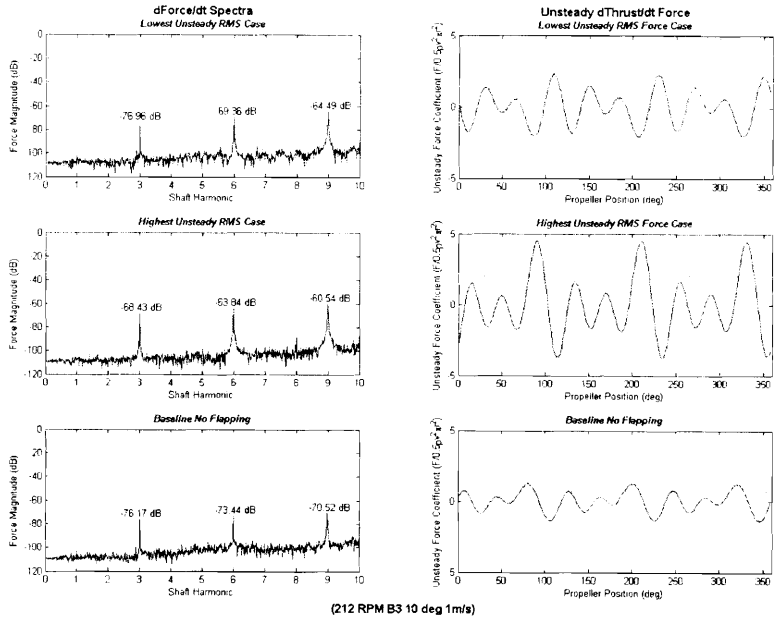

Figure 4-39: Discrete Fourier Transform of the time derivative of the highest, lowest and baseline RMS thrust force cases for propeller A (212RPM), 10° amplitude @ 1m/s

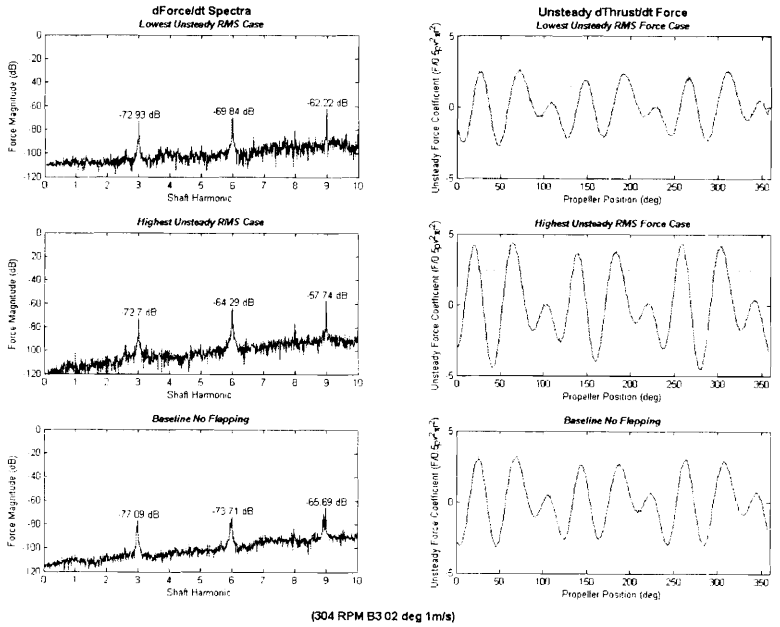

Figure 4-40: Discrete Fourier Transform of the time derivative of the highest, lowest and baseline RMS thrust force cases for propeller B (304RPM), 2° amplitude @ 1m/s

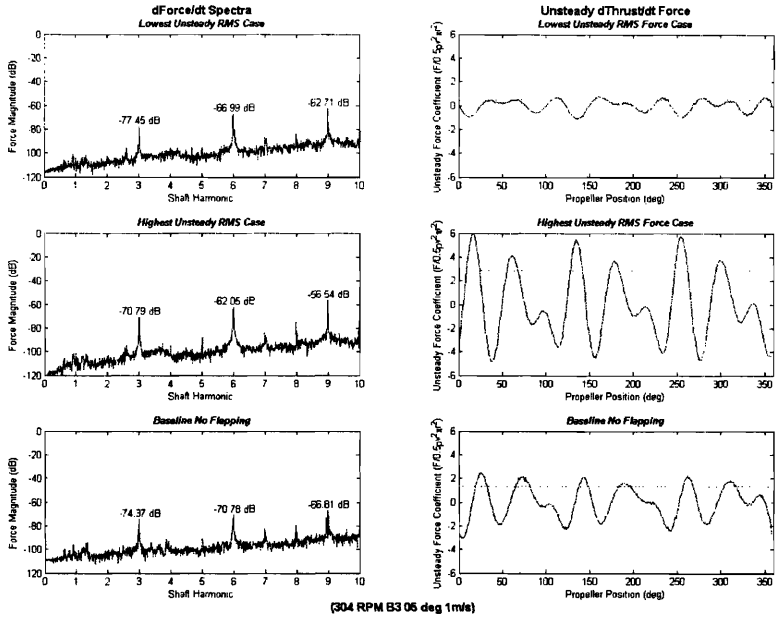

Figure 4-41: Discrete Fourier Transform of the time derivative of the highest, lowest and baseline RMS thrust force cases for propeller B (304RPM), 5° amplitude @ 1m/s

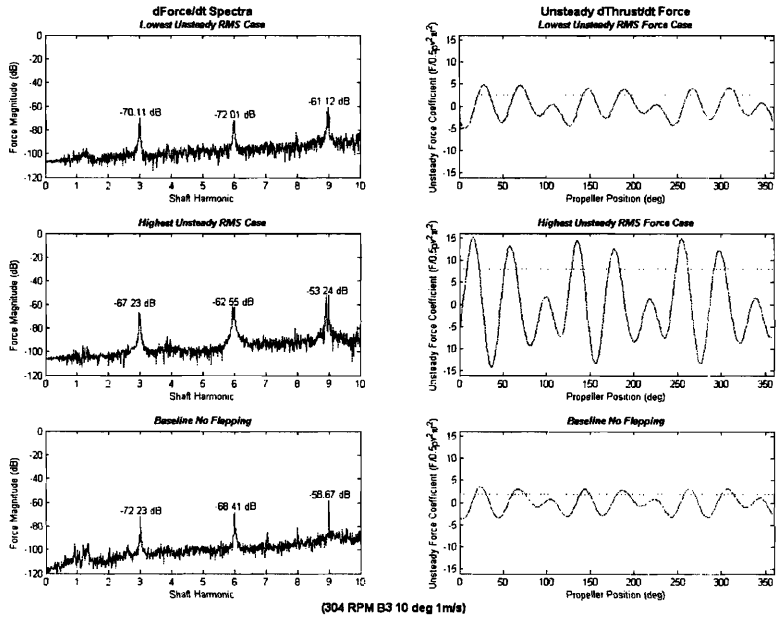

Figure 4-42: Discrete Fourier Transform of the time derivative of the highest, lowest and baseline RMS thrust force cases for propeller C (304RPM), 10° amplitude @ 1m/s

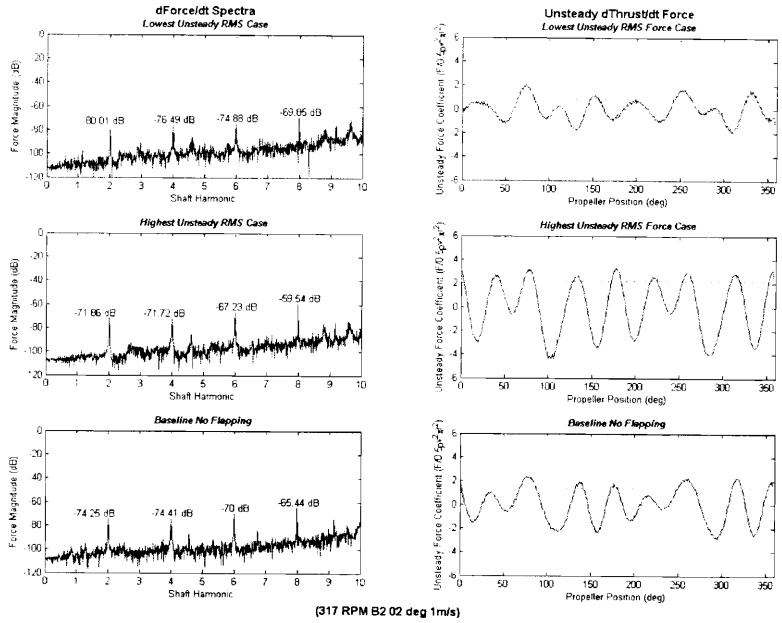

Figure 4-43: Discrete Fourier Transform of the time derivative of the highest, lowest and baseline RMS thrust force cases for propeller C (317RPM), 2° amplitude @ 1m/s

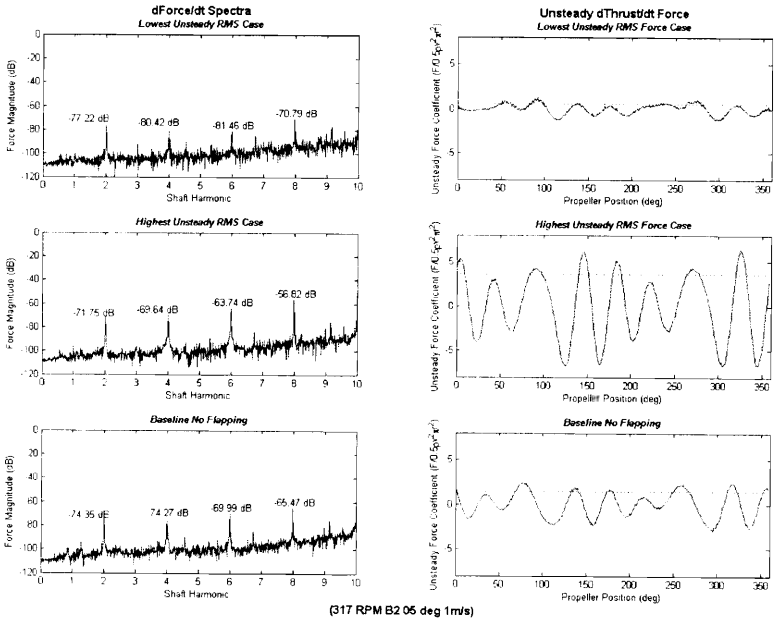

Figure 4-44: Discrete Fourier Transform of the time derivative of the highest, lowest and baseline RMS thrust force cases for propeller C (317RPM), 5° amplitude @ 1m/s

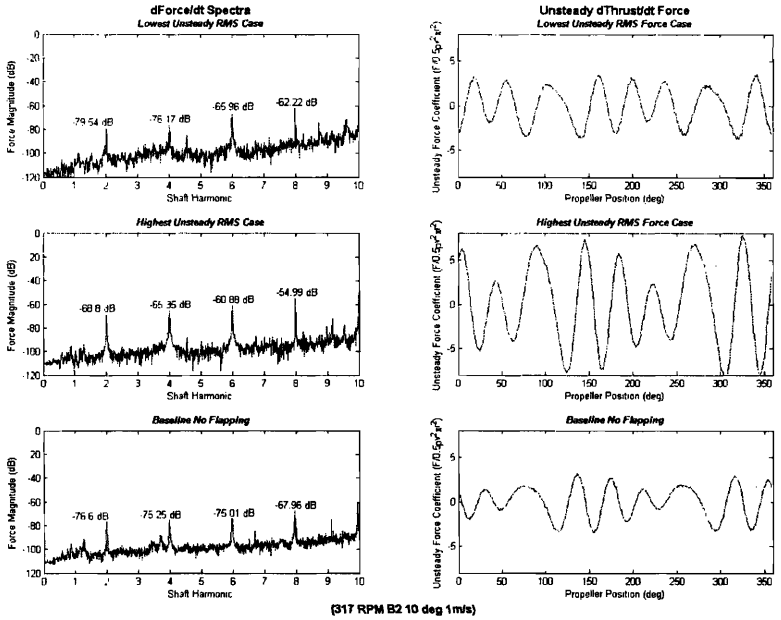

Figure 4-45: Discrete Fourier Transform of the time derivative of the highest, lowest and baseline RMS thrust force cases for propeller C (317RPM), 10° amplitude @ 1m/s

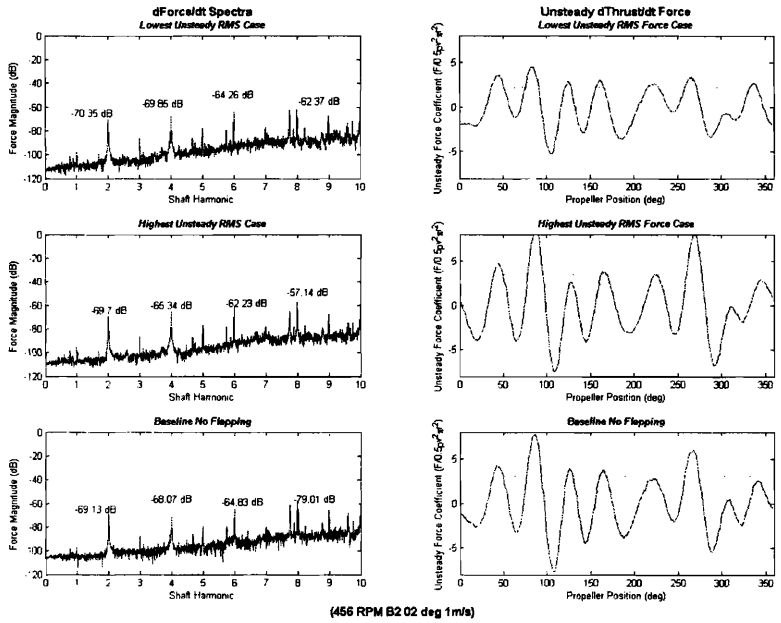

Figure 4-46: Discrete Fourier Transform of the time derivative of the highest, lowest and baseline RMS thrust force cases for propeller D (456RPM), 2° amplitude @ 1m/s

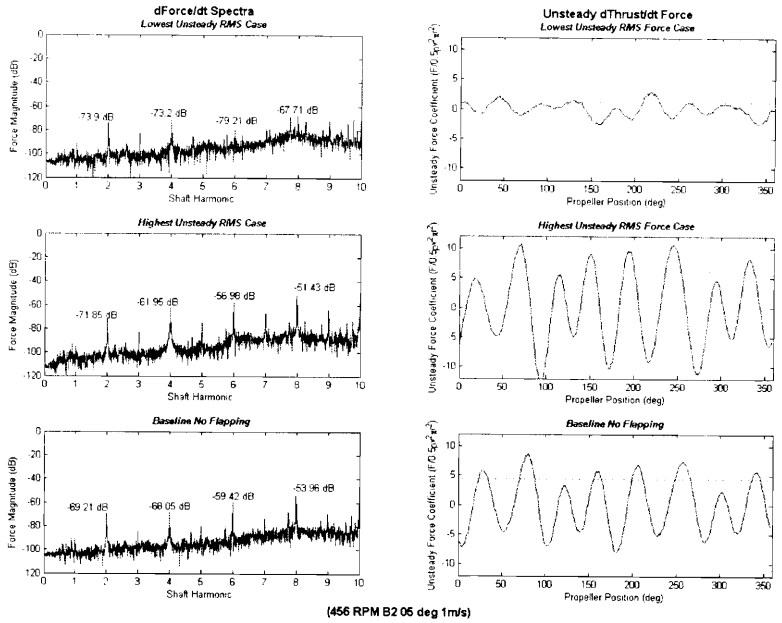

Figure 4-47: Discrete Fourier Transform of the time derivative of the highest, lowest and baseline RMS thrust force cases for propeller D (456RPM), 5° amplitude @ 1m/s

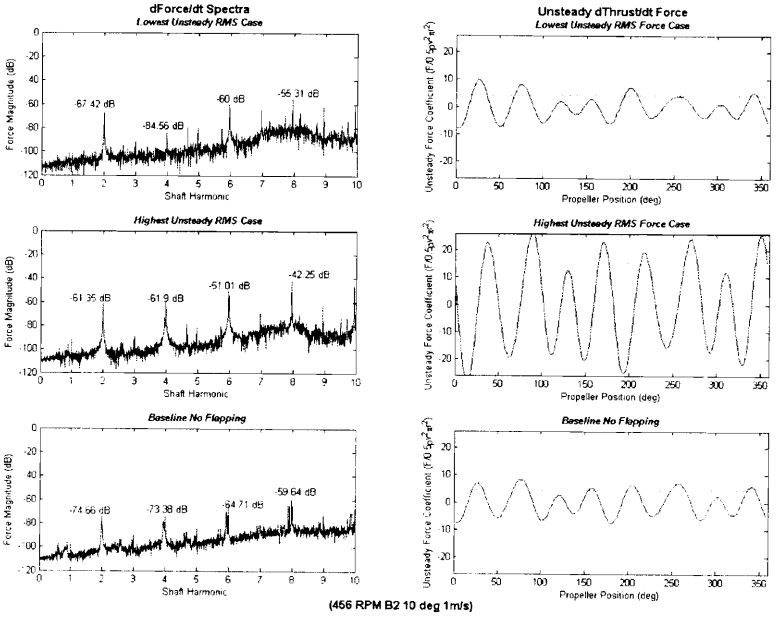

Figure 4-48: Discrete Fourier Transform of the time derivative of the highest, lowest and baseline RMS thrust force cases for propeller D (456RPM), 10° amplitude @ 1m/s

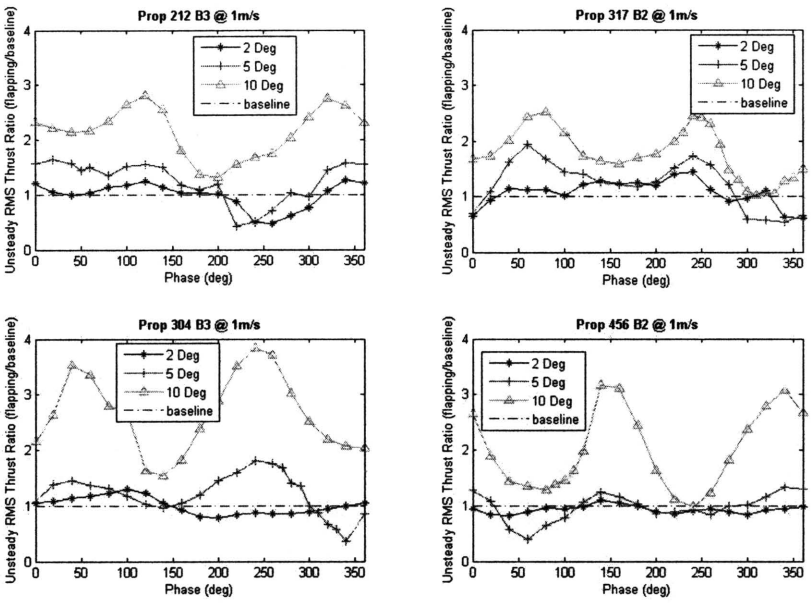

Figure 4-49: The RMS thrust force coefficient versus phase for every propeller at different flapping amplitudes

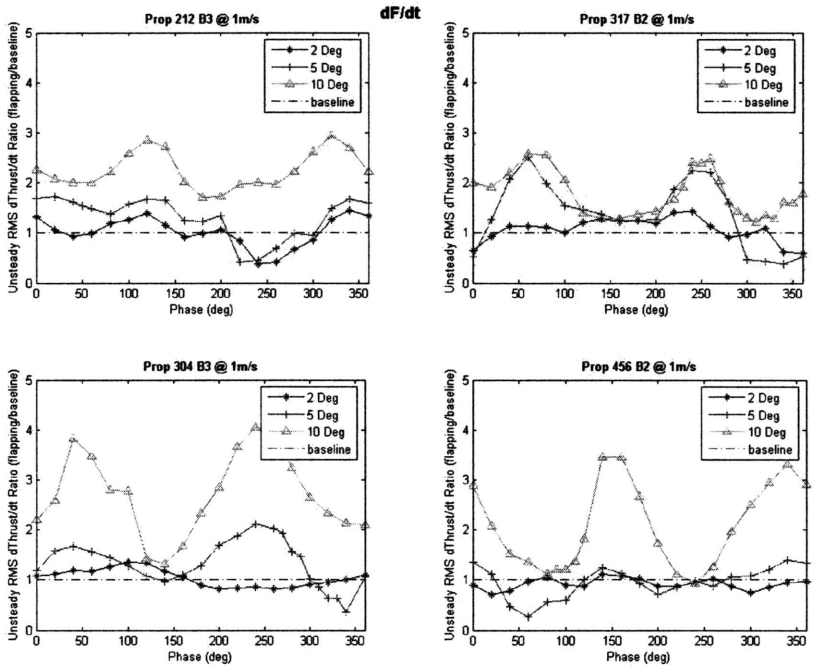

Figure 4-50: RMS of the time derivative of the thrust force coefficient versus phase for various propellers at different flapping amplitudes

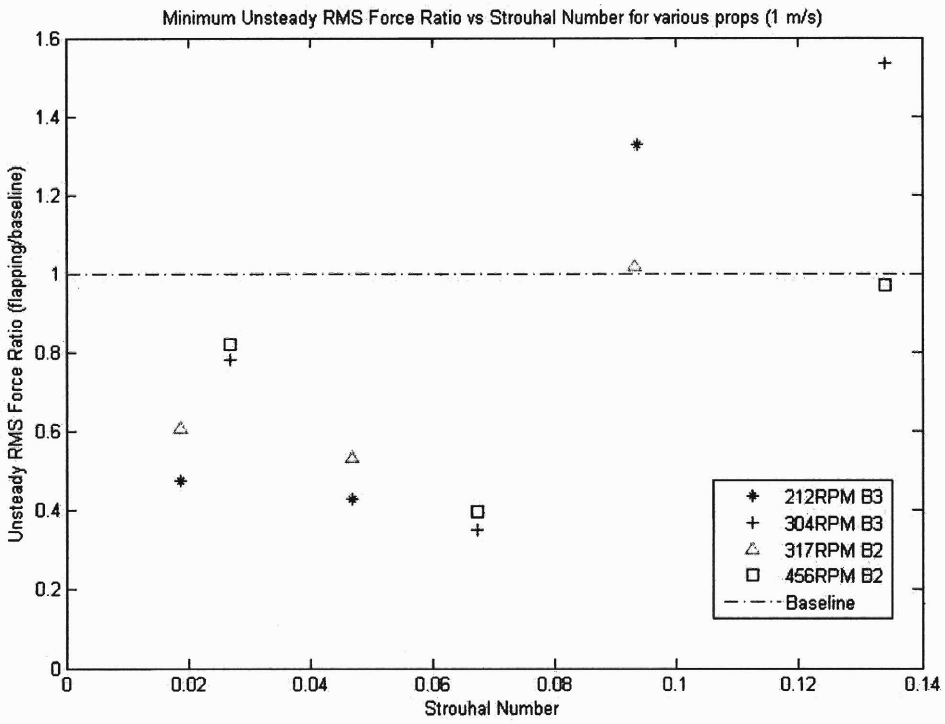

Figure 4-51: For every propeller and flapping amplitude the stator phase with the lowest RMS thrust force is shown as a ratio of the baseline wake

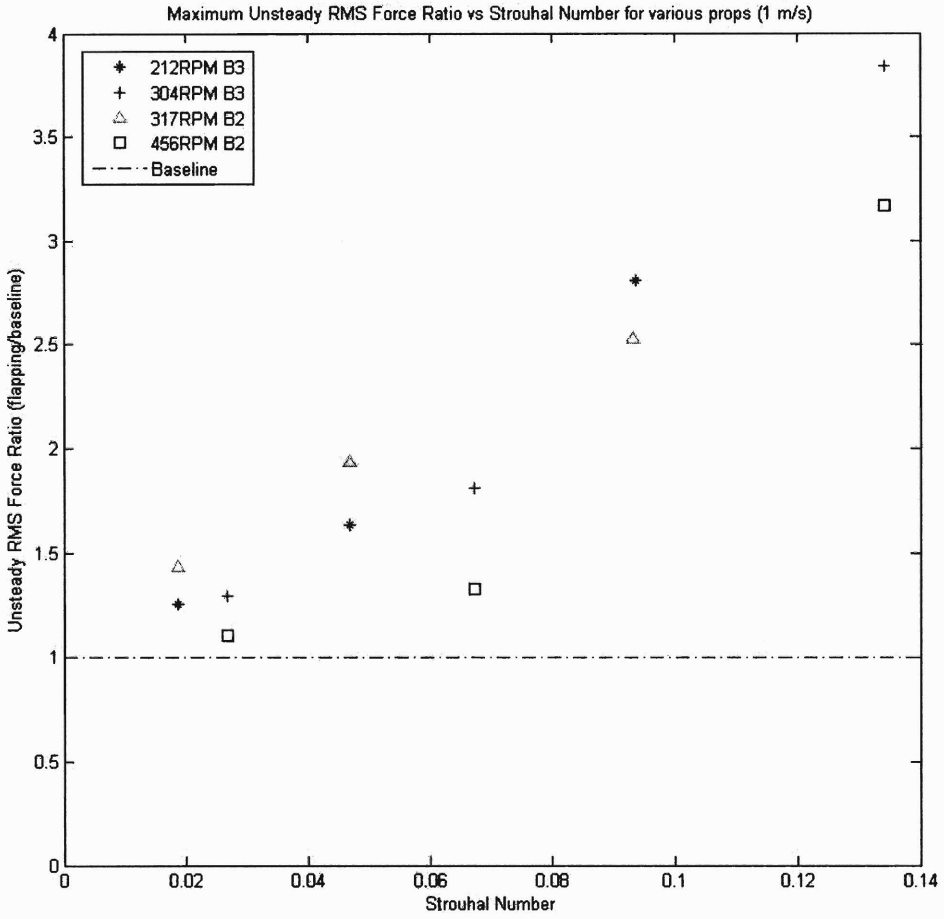

Figure 4-52: For every propeller and flapping amplitude the stator phase with the largest RMS thrust force is shown as a ratio of the baseline wake

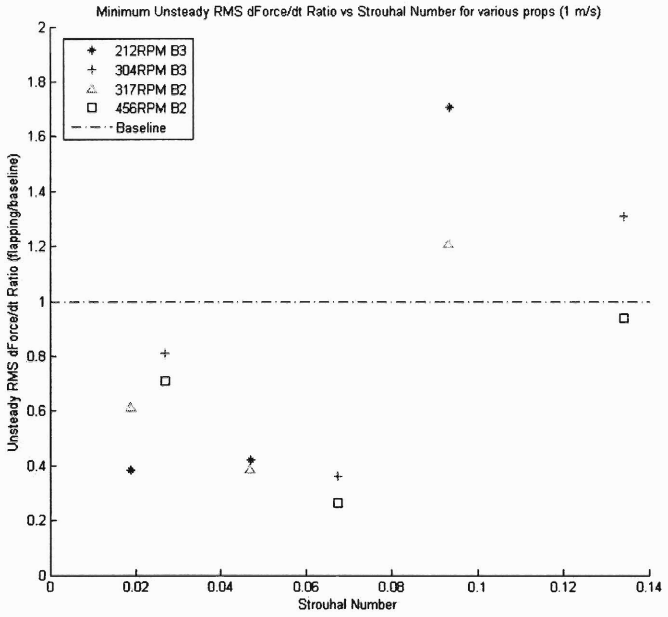

Figure 4-53: For every propeller and flapping amplitude the stator phase with the lowest RMS of the time derivative of the thrust force is shown as a ratio of the baseline wake

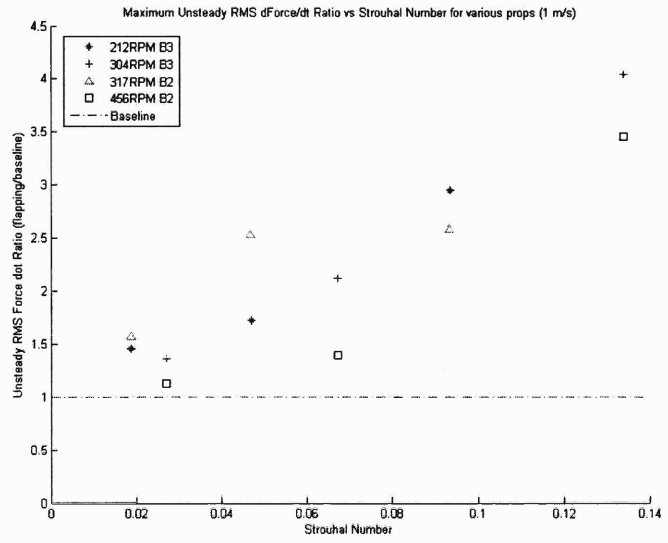

Figure 4-54: For every propeller and flapping amplitude the stator phase with the largest RMS of the time derivative of the thrust force is shown as a ratio of the baseline wake

4.5 Asynchronous Stator Flapping

Until now, any mention of tail articulation in this document referred to synchronized flapping, i.e. the articulation of the stator was controlled so that the phase angle between the stator and propeller blades remains constant for any given experimental trial. This section however, discusses the effect that uncontrolled articulation may have on unsteady propeller forces. The idea behind this concept would be to explore the potential of using a simple stator system that would not require any sort of active control to increase a vehicle's stealth.

In asynchronous flapping, propeller blades would see a wake whose configuration is different at every wake crossing. In a purely mathematical sense, asynchronous stator flapping could be thought of as tail articulation that has a constantly varying phase angle in time. In synchronized flapping, for a given Strouhal number, the configuration of the wake seen by the propeller depends only on the phase between the propeller and stator. For asynchronous flapping each blade crossing would experience a wake at a different phase angle. For sinusoidal stator flapping, over a period of time, the phase angle seen by any particular blade would be linearly distributed from 0° to 360°. One could re-run the same experimental cases described in this section using asynchronous flapping of the stator and propeller, permitting the slight variations in velocity of the two motors to inject an asynchronicity or beating between the stator and propeller. Such tests would be equivalent to a continuously varying phase angle as mentioned previously so the result can be predicted mathematically by simply averaging the unsteady forces produced at each phase angle for a particular test case. The RMS thrust force can be similarly be predicted by averaging the RMS force measured at each phase angle. A second look at figures 4-49 and 4-50 reveals that at worst asynchronous flapping would lead to unsteady forces higher than the baseline case and at best they would show negligible improvement. Such a system of articulation would have little practical value in a stealth application however, since invariably for certain cycles, propeller blades would be generating unsteady forces of the same magnitude as those in the noisiest phase angle cases (seen in figure 4-52).

4.6 Summary of Unsteady Force Results

- For all St, the relative magnitude of unsteady forces varies with the stator-propeller phase angle and St. RMS unsteady force exhibits local minima and maxima related to phase angle.

- At $St < 0.08$ certain phase angles exhibit unsteady force (and the time derivative of unsteady force) reduction as compared with the baseline wake.
- At $St > 0.08$ unsteady forces are greater than the baseline wake for all phase angles. These cases correspond to a 10° flapping amplitude.
- For all St, the highest unsteady forces produced (corresponding to certain phase angles) are greater than force in the baseline wake and they become larger with increasing St.
- Unsteady thrust force and its time derivative exhibit the same trends with respect to St, phase, and flapping amplitude.
- Spectra of unsteady force and its time derivative exhibit changes in the magnitudes of blade rate tonals consistent with changes in measured RMS unsteady force versus St, phase angle and flapping amplitude.
- Asynchronous stator flapping is discussed as sinusoidal articulation with a varying phase angle. Unsteady forces are the mean of those measured across all phase angles for a particular case leading to greater forces than the baseline wake.

Chapter 5

Analysis of Propeller - Wake Effect using Reduced Order Model

This chapter discusses the use of a reduced order wake model to calculate the stator generated velocity field in order to determine the blade-wake effect. Blade-wake interaction is observed through the visualization of relative vortex-blade positions.

5.1 Theory

A reduced-order model relating tail motion to the resulting unsteady wake was proposed by Macumber in [5]. The model is based on the simplifying assumptions of potential flow. Potential flow assumes that a fluid is inviscid and irrotational. These are typically reasonable assumptions to make when dealing with underwater flows. Velocity fields in potential flows can be expressed as the gradient of the scalar potential function, ϕ, which satisfies Laplace's equation:

$$\vec{u} = \nabla\phi = \left(\frac{\partial\phi}{\partial x}\hat{x}, \frac{\partial\phi}{\partial y}\hat{y}\right), \nabla^2\phi = 0$$

Although potential flow requires irrotational flow, velocity fields containing vorticity can be presented by various potential functions which specify zero vorticity and divergence everywhere except at a singular point. Linear superposition holds for potential functions so velocity fields can be constructed by the placement of a combination of potential functions. Two-dimensional vortex sheets are commonly modeled by a distribution of point vortex elements whose potential functions are: $\phi = -\frac{\gamma}{2\pi}\theta$, where γ is the vortex strength and θ is the angular coordinate. Free vortex points move with the local fluid velocity at its singularity so the velocity of individual vortex elements

is the sum of the induced velocities due to other vortices and the free stream velocity. This can be written as:

$$\begin{bmatrix} \dot{x}_i \\ \dot{y}_i \end{bmatrix} = \begin{bmatrix} U \\ V \end{bmatrix} + \sum_{j=1, j\neq i}^{N} \frac{\gamma_j \left(1 - exp\left(-r_{ij}^2/\delta^2\right)\right)}{r_{ij}^2} \begin{bmatrix} 0 & -1 \\ 1 & 0 \end{bmatrix} \begin{bmatrix} x_i - x_j \\ y_i - y_j \end{bmatrix}$$

where r_{ij} is the radial seperation between vortex j and vortex i. $1 - exp\left(-r_{ij}^2/\delta^2\right)$ is a smoothing kernel used to prevent numerical instability as r goes to 0. δ is the boundary layer thickness at the stator trailing edge which is defined simply using the empirical expression: $\delta = L_{chord}\frac{0.37}{Re^{0.2}}$ Two-dimensional vortex sheets are unstable and patches of like signed vorticity tend to roll up into discrete vortices. The vorticity shed by the stator was modeled as a simple function of the velocity of the stator tail tip:

$$\gamma_{net}(t) = -\frac{UL_{tip}\Delta t}{\delta} v_{tip}(t)$$

The shed vorticity due to the baseline wake is modeled as:

$$\gamma_0 = U^2 \delta t$$

At each time step, half of the vorticity due to stator flapping and the half of the vorticity due to the baseline wake are added to discrete vortices introduced at the upper and lower surfaces of the stator trailing edge. These discrete vortices are separated by a distance δ. This reduced order model is able to replicate the vortex sheet roll up observed experimentally by PIV wake measurements. Figure 5-1 shows a visual example of the wake calculated using this reduced order model. A more detailed derivation and explanation of this reduced order model can be found in [5].

5.2 Propeller - Wake Visualization

The reduced order model presented in section 5.1 assumes that the velocity field created by the stator is two dimensional. This is a fair simplification to make when observing a lone stator. Once a propeller is introduced however, the velocity fields become inherently three dimensional. In order to aid understanding of the effect of the stator wake on a propeller, a simplified three-dimensional propeller-wake visualization was created. Due to a lack of PIV data for the test cases studied, the reduced order model was used to calculated the velocity field in a two dimensional grid downstream of the stator. The flow field vorticity is calculated and the two-dimensional grid is

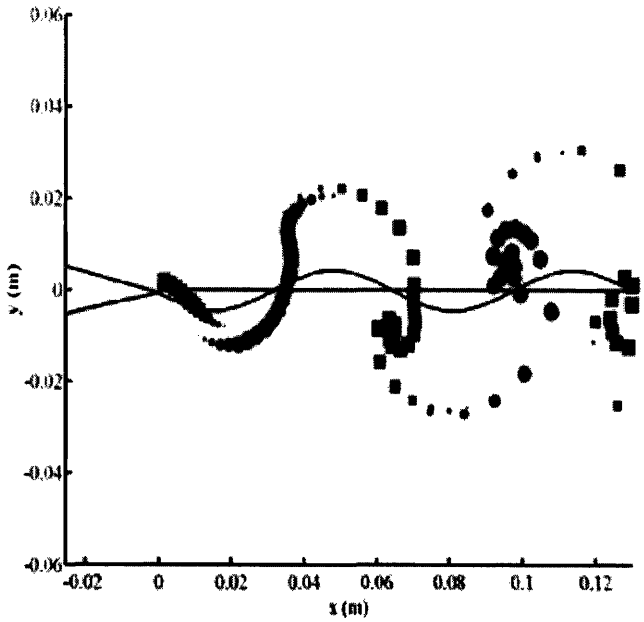

Figure 5-1: Example of stator wake calculated using reduced order model. $St = 0.023$

extended in 3D so that vorticity due to the wake is extruded down the span of the stator toward the center of the water tunnel. Vorticity is plotted as iso-surfaces in order to visualize the wake as a three dimensional object. By placing an animated three-dimensional model of a propeller in this velocity field, the relative position of wake vortices and propeller blades can be seen visualized. The instantaneous velocity and effective angle of attack at any pre-defined points on a propeller blade can be calculated to gain further insights into the blade-wake interaction. The flow field generated by the stator is simply displayed and not calculated 'in-situ' thus the flow field is not coupled to the simulated propeller. Any effects the propeller may have on the wake itself are not captured. Furthermore, in real fluid flows, vortex tubes cannot end in the middle of a fluid region, they must either end at a wall or form a closed vortex ring. The simulation, however, is useful in visualizing the timing of vortex and blade passing.

Figure 5-2 shows a simulation of propeller A spinning behind a stator flapping with a 10° amplitude and a phase of 0°. Figure 5-3 shows a top view of the orientation of wake vortices when a propeller blade crosses through the wake. Starting from the upper left, the phase angles corresponding to the extrema of the RMS thrust force for that test case are represented. Figures 5-4 and 5-5 show the corresponding images for propeller B in a 5° wake and propeller C in a 2° wake respectively. Figure 5-6 presents views of the wake at phases corresponding to the discernible global extrema

if the RMS thrust of propeller C spinning in a 2° amplitude wake. These figures clearly show why the phase angle of stator articulation is of critical importance in blade-wake interaction. The phase angle determines the orientation and position of wake vortices relative to propeller blades for a given stator Strouhal number.

5.3 Unsteady Force, Strouhal Number and Phase Relationship

Closer observation of figures 5-3 through 5-6 reveals the relationship between the RMS thrust force produced and the configuration of the wake as it is traversed by a propeller wake. Lowest RMS forces occur when a propeller blade traverses the wake so that is passes between vortices. Highest RMS forces occur when propeller blades pass though a wake vortex as they traverse the wake region. This result makes physical sense because the flow field of the area between wake vortices has a relatively constant fluid velocity. Conversely, within wake vortices themselves the fluid velocity varies greatly from the free stream value. Within a vortex, the velocity field is directed so that it rotates around the vortex center and its magnitude increases with greater proximity to the center. A propeller blade slicing through a vortex would see a velocity field whose intensity would increase as the blade approaches the vortex's center. The velocity field on the opposite side of the vortex center is directed in an opposite direction hence a blade would suddenly encounter a field oriented in the opposite direction that then decreases in magnitude as the separation distance from the center increases. Figure 5-7 demonstrates this effect by plotting the velocity field due to a vortex along a line AB. These extreme changes in both direction and magnitude of the flow field seen by the propeller explain why crossing a vortex can create large unsteady in propeller force. The rate of change of the flow field in time depends directly on the speed a blade traverses the wake. A propeller spinning at a high angular rate would experience this change in velocity field over a shorter time period than a propeller spinning at a slower rate. Reviewing figure 3-8, where the effect of a stationary stator is measured, RMS thrust force indeed increases as the propeller's angular velocity is increased. Figure 5-8 shows the absolute value of the RMS thrust force and its derivative for the best and worst case phase angles of each propeller versus Strouhal number. For a given Strouhal number, the greater the propeller's velocity the higher the RMS thrust (or derivative of the thrust) is measured.

From figures 5-3 through 5-6 it is apparent that the stator wake vortex changes

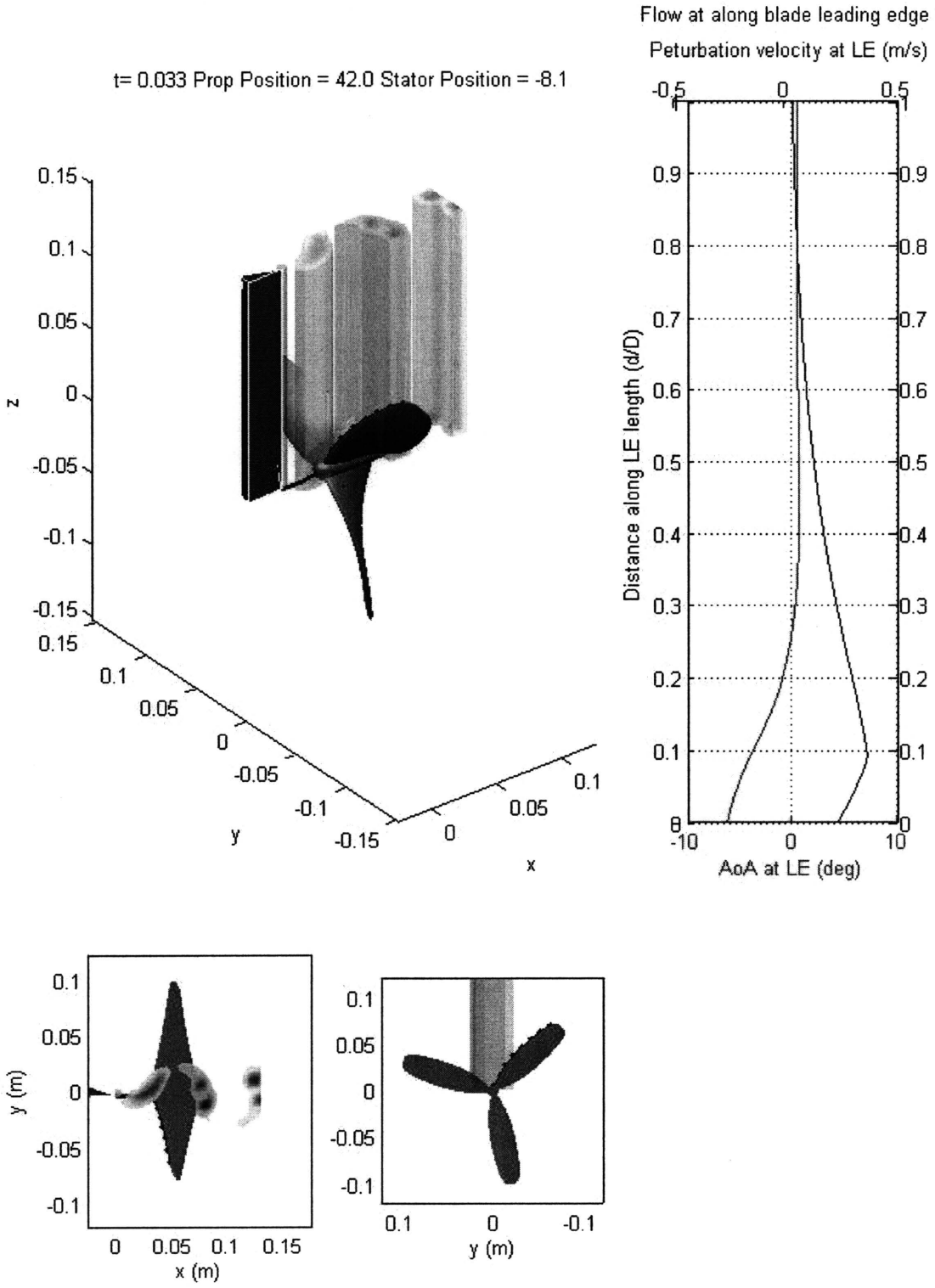

Figure 5-2: Visualization of a propeller behind articulating stator

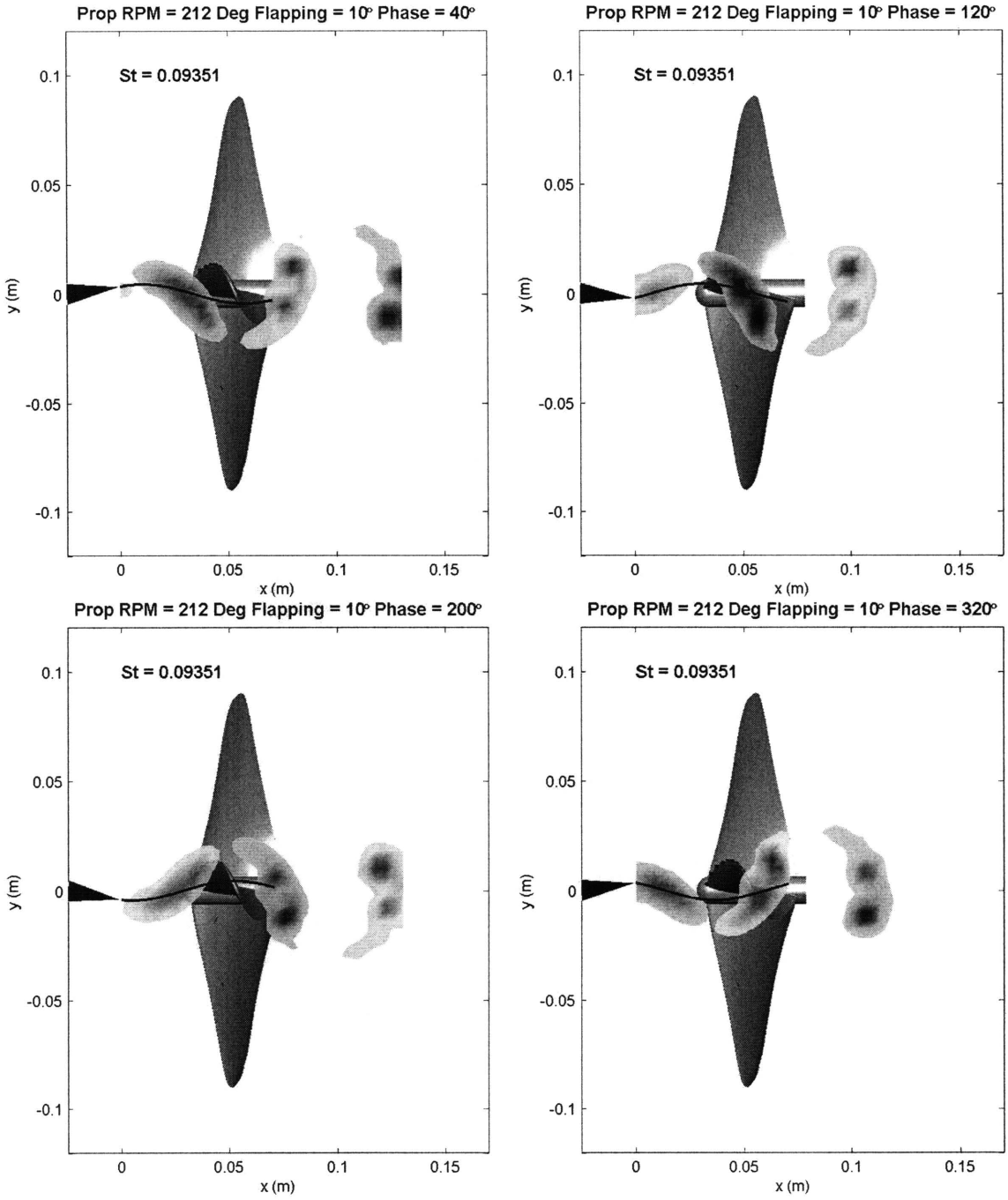

Figure 5-3: Position of vortex wake as propeller blades cross the stator wake for various phase angles corresponding to the extrema of the RMS thrust force: Propeller A 10° amplitude at 1m/s

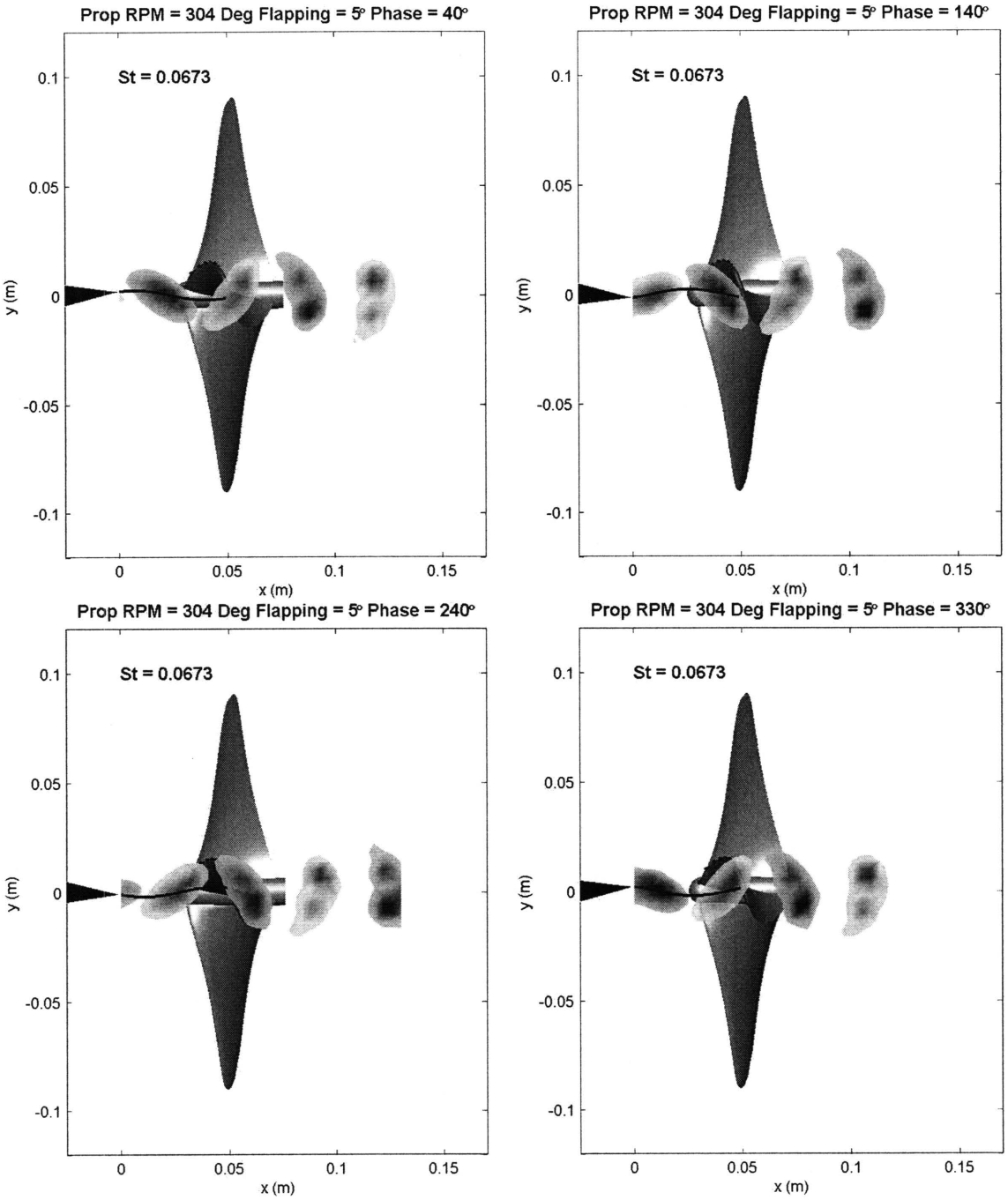

Figure 5-4: Position of vortex wake as propeller blades cross the stator wake for various phase angles corresponding to the extrema of the RMS thrust force: Propeller B 5° amplitude at 1m/s

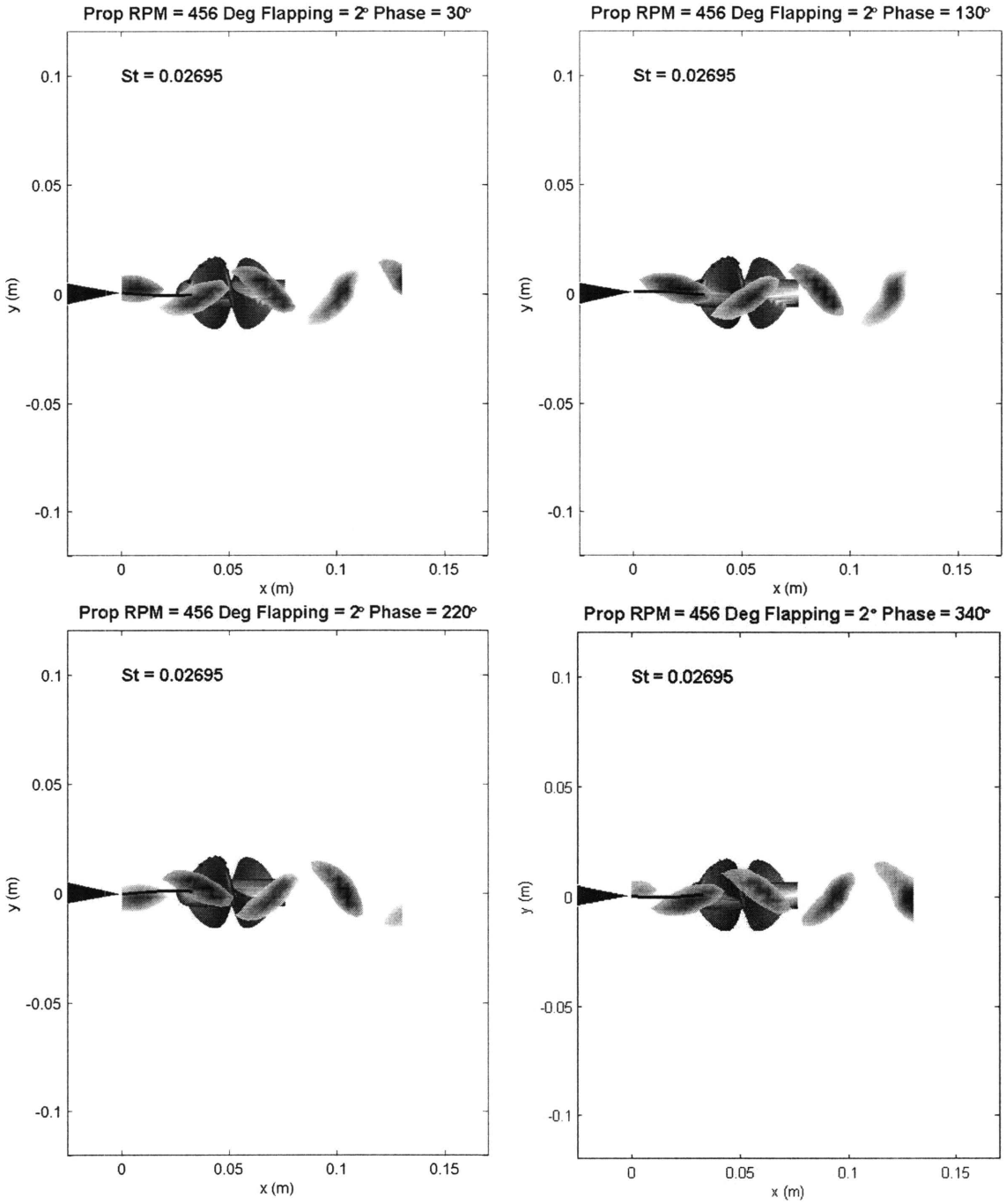

Figure 5-5: Position of vortex wake as propeller blades cross the stator wake for various phase angles corresponding to the extrema of the RMS thrust force: Propeller D 2° amplitude at 1m/s

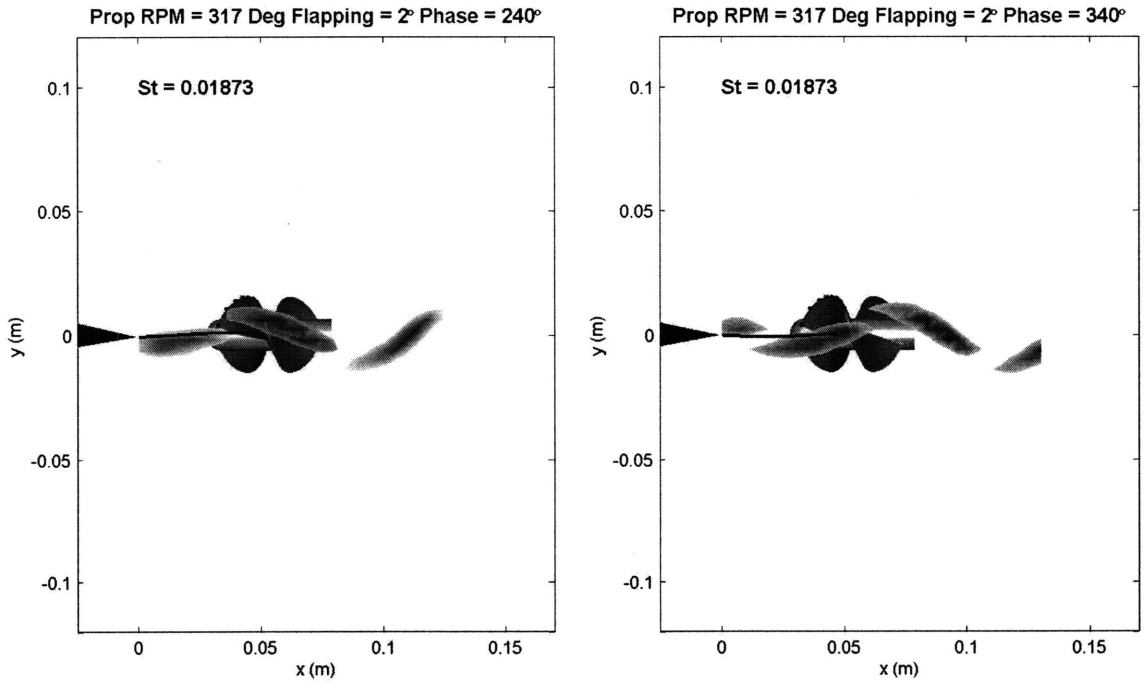

Figure 5-6: Position of vortex wake as propeller blades cross the stator wake for various phase angles corresponding to the extrema of the RMS thrust force: Propeller C 2° amplitude at 1m/s

with the flapping amplitude and flapping frequency (which is a fixed ratio of propeller speed). Macumber showed that the shape and other characteristics of the wake are related to the Strouhal number the stator operates at [5]. As the Strouhal number of the wake increases, the wake vortex sheet shows greater roll up into discrete vortices. The strength of these discrete wake vortices relative to the wake geometry increases with Strouhal number. For a given flapping rate, a flapping amplitude of 10° shows tighter and stronger vortices than those at 2° and 5° amplitude. As the strength of a vortex increases, its effect on the surrounding flow field becomes greater. This phenomenon reveals a clue as to why stator flapping at 10° only had the detrimental effect of increasing unsteady thrust forces. At this amplitude the generated wake has very large and strong discrete vortices that exert a large influence on the surrounding fluid. Thus the velocity field in regions of the wake between vortices is not as uniform and will exhibit large velocity gradients generating large unsteady propeller forces. At lower amplitudes the wake region between vortices is much 'calmer' by comparison, allowing a reduction of unsteady forces. The results presented in this and previous sections imply that the instantaneous characteristics of the the local wake interacting with the propeller blade determine the unsteady propeller forces produced. It was

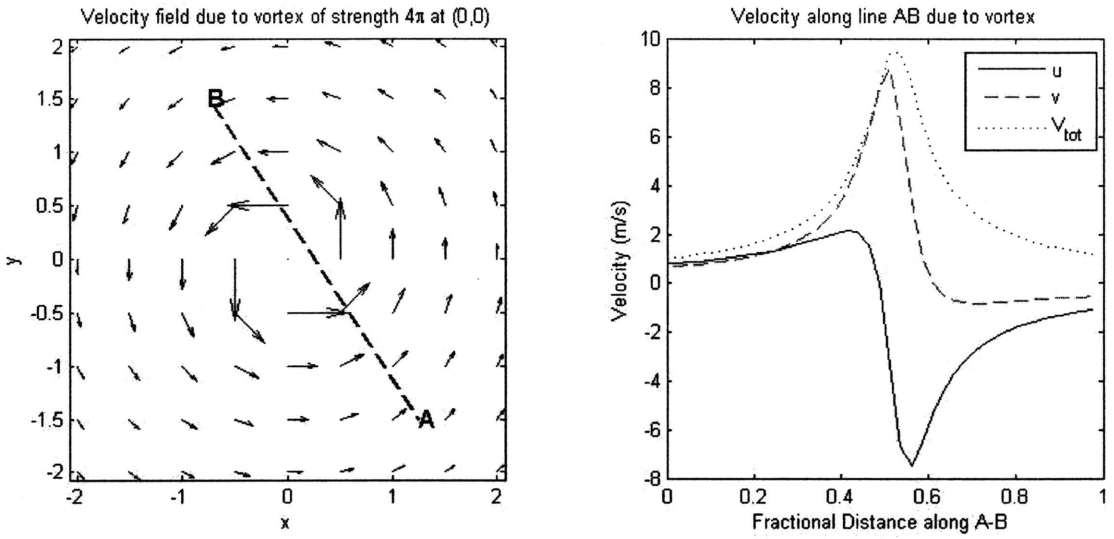

Figure 5-7: Velocity field due to vortex and its effect along a path AB

previously believed that stator flapping that fills the wake deficit in a time-mean sense might exhibit force reduction potential. When the wake is filled in a time-mean sense the stator introduces enough energy into the flow to cancel out the energy removed by its own boundary layer. While the time-mean of the wake may show no defect, instantaneously however, local fluid regions will show a strong rolled up vortex sheet that is quite different from the free stream fluid surrounding it.

5.4 Propeller Inflow Velocity due to Wake

In section 5.3 the effect of a vortex on a fluid's velocity field was mentioned. Using the 3D propeller-wake visualization simulation, the velocity field can be calculated at any point on a propeller blade as it rotates within the wake defect. Figures 5-9 through 5-12 show the velocity field calculated at a point on a propeller blades' leading edge. This point is at a distance along the blade span corresponding to the propeller's mean-area radius. As a blade crosses the wake, both the local u and v velocities are affected by the proximity and strength of any wake vortices. As seen in equation 1.1, the effective angle of attack of a blade section changes with u and v, so as a blade section crosses the wake its angle of attack changes throughout the crossing. According to linearized airfoil theory, the lift generated by an airfoil section at low angles of attack, is proportional to its angle of attack and fluid velocity. It becomes apparent from the lower graphs in figures 5-9 through 5-12 how the lift generated by a blade can vary according the the configuration of the wake as it is

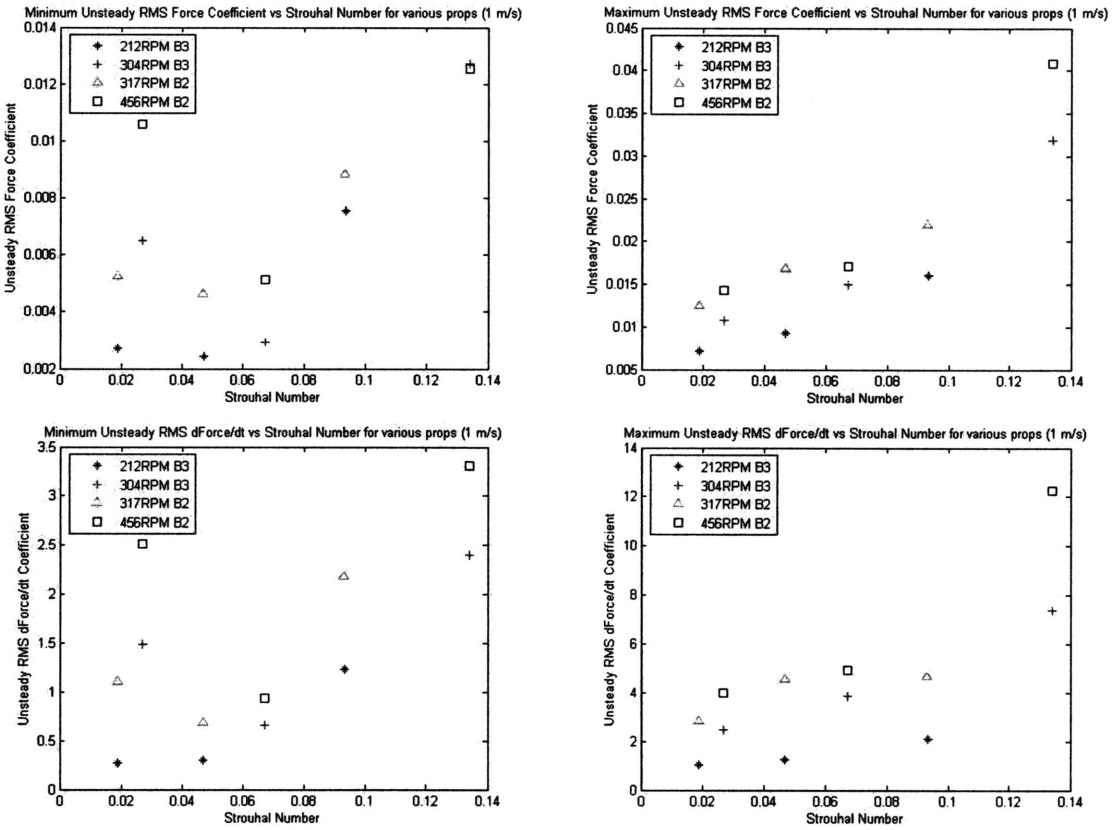

Figure 5-8: Absolute value of both RMS force and RMS derivative of thrust force versus St for the best and worst-case scenarios for each propeller

traversed. The phases shown in each figure correspond to the extrema in RMS thrust force for the test cases displayed. All of the flapping cases show fluctuations in both the velocity and angle of attack at this point on the blade leading edge. In reality, the lift generated by a blade section depends on the fluid velocity at all points along its surface, so it is still possible for the overall blade section unsteady lift to be smaller than in the baseline wake case. This fact implies that for a complete understanding of the interaction between a propeller blade and the wake, a three-dimensional analysis along the entire blade surface must be pursued.

5.5 Summary of Propeller - Wake Effect

- 2D reduced-order model was used to calculate velocity field due to stator articulation. Using 3D visualization, relative propeller-wake vortex position was observed to determine effect of instantaneous wake on propeller blade forces.
- Strength, shape, and separation of wake vortices varied with St. Wake vortex sheet shows increasing roll up with high St.
- Phase angles showing the lowest RMS unsteady forces correspond to wake-blade timing such that propeller blades traverse wake between vortices. Phase angles exhibiting the highest RMS unsteady forces correspond situations where propeller blades 'slice' through wake vortices.
- 2D analysis of wake velocities at a point on blade leading edge was insufficient in fully describing the effect of the wake on blade forces.

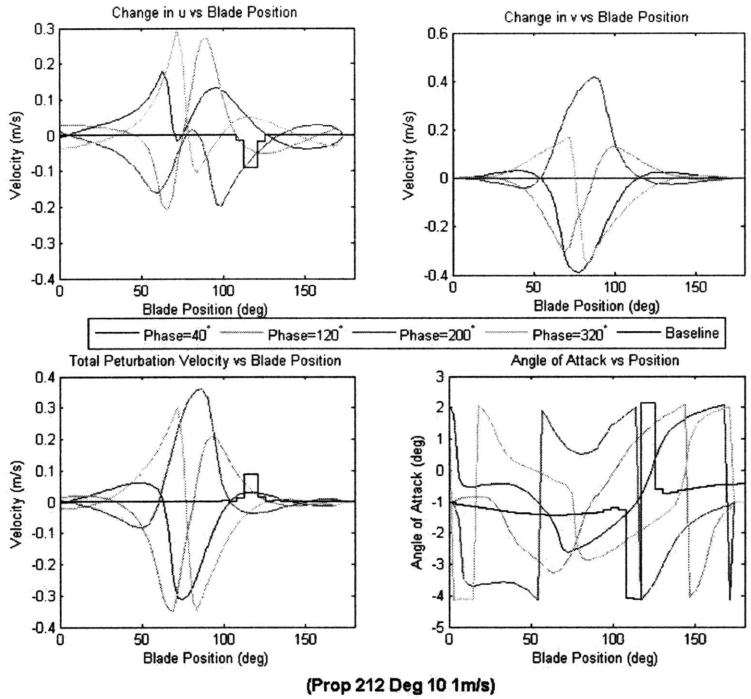

Figure 5-9: Velocity field seen by a point on propeller leading edge versus position as it crosses the wake at different phase angles. Propeller A, 10° flapping, 1m/s

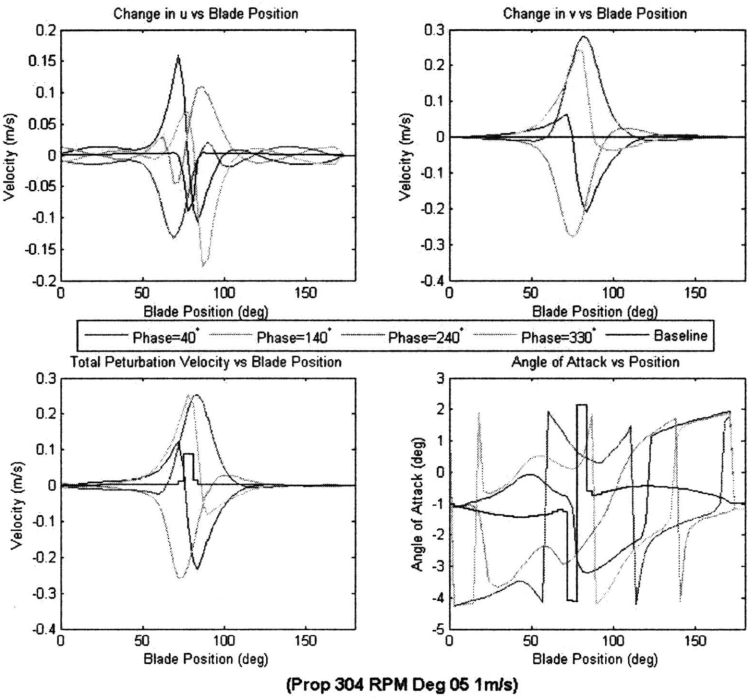

Figure 5-10: Velocity field seen by a point on propeller leading edge versus position as it crosses the wake at different phase angles. Propeller B, 5° flapping, 1m/s

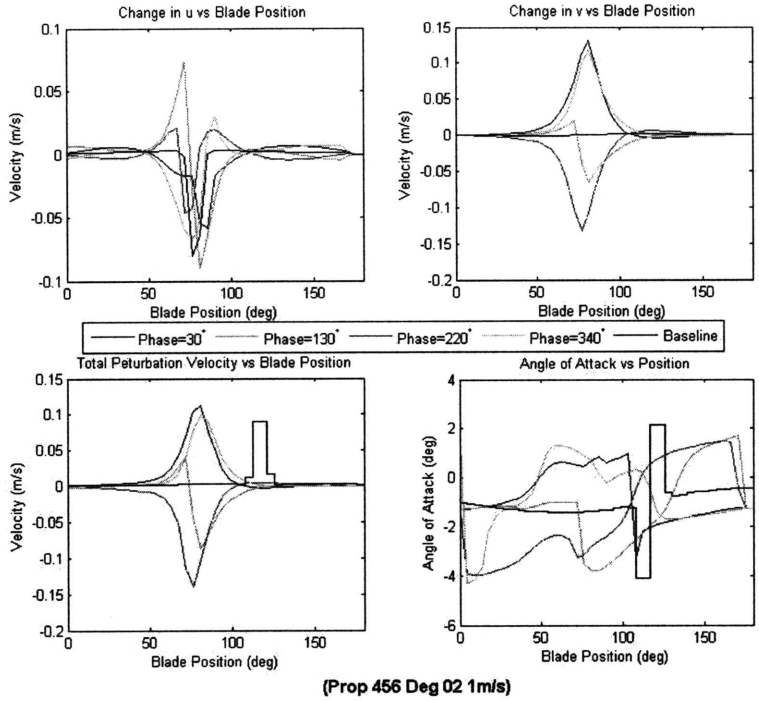

Figure 5-11: Velocity field seen by a point on propeller leading edge versus position as it crosses the wake at different phase angles. Propeller D, 2° flapping, 1m/s

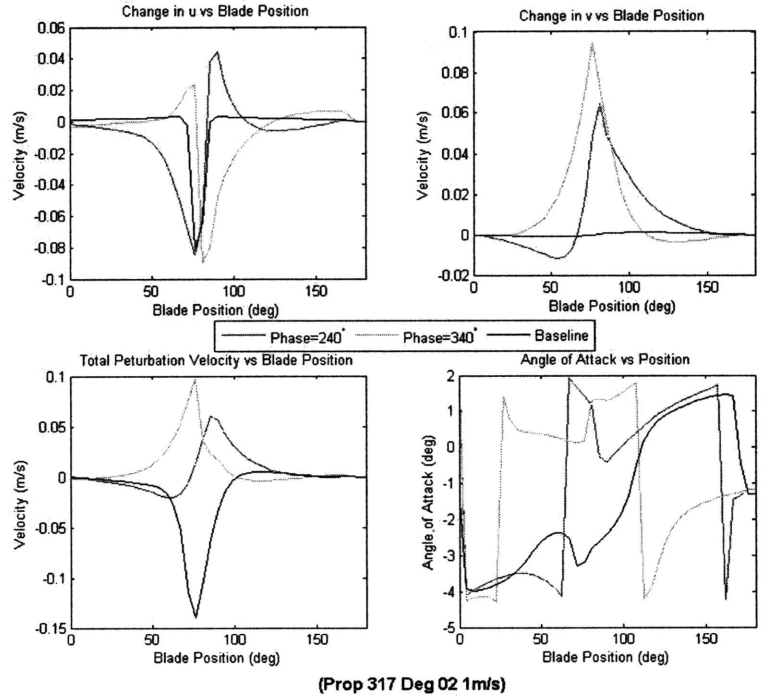

Figure 5-12: Velocity field seen by a point on propeller leading edge versus position as it crosses the wake at different phase angles. Propeller C, 2° flapping, 1m/s

Chapter 6

Conclusion

6.1 Conclusion

The work presented in this thesis shows the potential of using stator tail articulation to reduce the noise created by the interaction of a propeller blade with a wake deficit. Previous work by Macumber and Opila [5, 6] demonstrated that the wake downstream of a stator can be controlled using tail articulation for a wide range of Reynolds numbers and that the deficit can be filled by articulation at a sufficient Strouhal number. This thesis reaffirms the work in [5, 6] and in particular confirms the ability of sinusoidal stator tail articulation to effectively reduce unsteady thrust forces of non-lifting propellers operating within a wake. For a given propeller, the Strouhal number and phase angle of articulation can be specified so that a significant unsteady thrust reduction is accomplished over the baseline static stator wake, Figures 4-49 & 4-50.

This study was experimental in nature so a propeller-force measurement apparatus was designed to detect the forces generated by a propeller within a water tunnel using a six component load cell as described in chapter 2. The apparatus uses a fairing designed to shield the load cell from the surrounding flow and minimize the disturbance of the fluid region surrounding the propeller. The apparatus was capable of accurately controlling the velocity and position of both the flapping stator tail and rotating propeller so that a constant phase angle could be precisely specified. Non-lifting propellers were designed to operate at a variety of angular rates so that a range of flapping Strouhal numbers could be explored. The vibrational characteristics of the apparatus were measured so that their effect on recorded data could be appropriately noted.

The effect of stator articulation on the instantaneous thrust force generated by

two and three bladed propellers versus propeller angular position was explored in chapter 4. Four propellers were tested which were designed to operate in a range of speeds (212-456 RPM in 1 m/s flow). Stator articulation was controlled so that each propeller blade would encounter an identical wake by fixing the flapping rate to be equal to the particular propeller's blade rate. Experiments were conducted by varying the phase angle and flapping amplitude of stator articulation for each particular propeller in section 4.2 Figures 4-1 through 4-24. It was found that the unsteady thrust force generated by each propeller was indeed affected by the specific tail articulation tested. For the propellers tested, stator articulation at a Strouhal number of 0.08 and below was capable of significantly reducing the RMS of both the unsteady thrust force and its time derivative as compared with the baseline wake. At Strouhal numbers above 0.08, stator flapping created increased unsteady thrust forces for every propeller as discussed in section 4.3. It was found that phase control between propeller and stator was necessary. At a given tail articulation amplitude and rate, the phase angle of the stator controls the configuration of the wake when a blade crosses it. At all Strouhal numbers tested, certain phase angles generated high unsteady thrust forces, creating the potential of increases unsteady forces and hence noise even when operating at $St < 0.08$, Figures 4-49 through 4-54. Similar results were found when the spectra of the measured thrust force was analyzed in section 4.3, Figures 4-25 through 4-48. Below $St < 0.08$ at certain phase angles, articulation was capable of reducing the magnitude of the first several blade harmonics as compared with the baseline case. Certain phase angles of $St < 0.08$ and all phase angles when operating at $St > 0.08$ showed an increase in the magnitude of these blade harmonics over the baseline case, Figures 4-25 though 4-48. The concept of using asynchronous stator flapping was explored in section 4.5. It is believed that articulation of this nature would lead to beating and the unsteady forces generated at certain cycles would be higher than the baseline wake, making it ill-suited for a stealth application.

The relationship between stator flapping phase and unsteady forces was further examined through the use of a reduced order articulation model created by Macumber [5]. This two-dimensional model was used to generate a three-dimensional representation of the stator wake flow field. Superposition of an animated 3D propeller model allowed the relative position between propeller blades and wake vortices to be visualized. From these simulations it was found that the phase angles which demonstrated minimum unsteady forces correspond to phases where propeller blades cross the wake between vortices. Conversely, increased unsteady forces corresponded to phase angles where propeller blades 'slice' through wake vortices as they traverse the

region directly downstream of the stator. The effect of wake vortices on the velocity field surrounding propeller blades was explored, however it became apparent that only a three dimensional analysis would yield an complete understanding of the relationship between instantaneous propeller forces and relative wake-blade position and vortex strength.

As a final note, in previous work it was hypothesized that the most significant noise reduction occured at Strouhal numbers corresponding to a maximum drag stator wake. In this work, significant reduction in unsteady forces was seen up to a Strouhal number of 0.08, which corresponds to a stator with a reduced drag wake.

6.2 Recommendations for Future Work

This section outlines several improvements that should be made in order to advance the concept of stator articulation for propeller noide reduction:

- This study focused only on sinusoidal stator articulation for unsteady force reduction. Previous work has shown that non-sinusoidal articulations may also show potential for force reduction so a future study exploring the effect of non-periodic and transient flapping is advised.

- Non-lifting propellers were used in this work in order to reduce the potential influence propeller blades would have on the wake itself. Obviously non-lifting propellers have no practical use in real vehicles, thus exploring the unsteady forces generated by lifting propellers (including those that have a non-symmetric blade profile) would certainly be useful.

- In this study the distance between the stator tail and propeller leading edges was kept constant. In viscous fluid flows, viscosity serves to spread and dissipate wake vortices, thus the blade-stator seperation distance is another experimental variable worthy of future study.

- Testing for this study was done at a constant tunnel velocity of 1 m/s. Exploring the Reynold's number dependence and laminar-turbulent flow transition on propeller-wake interaction merits exploration.

- In order to truly determine the overall impact on a vehicle's noise signature, the noise radiated by stator flapping must be accurately determined, although it is theorized that these forces are much smaller than unsteady propeller forces due to the lower fluid velocities in the vicinity of the stator.

- The reduced order model used to help visualize propeller-wake interaction due to a lack of PIV data for the test cases studied. The reduced order model presented is 2D, which for the purposes of devising a control scheme for active control of propeller forces is likely sufficient, it is not sufficient to fully capture inherently 3D flow phenomena when considering a rotating propeller in a wake.
- Practical applications of stators use cambered stators which are mounted at a non-zero angle of attack. The effect of a cambered and/or non-aligned stator is likely sufficiently different from the one presented in this study to require their own experimental study.

Appendix A

Apparatus Drawings

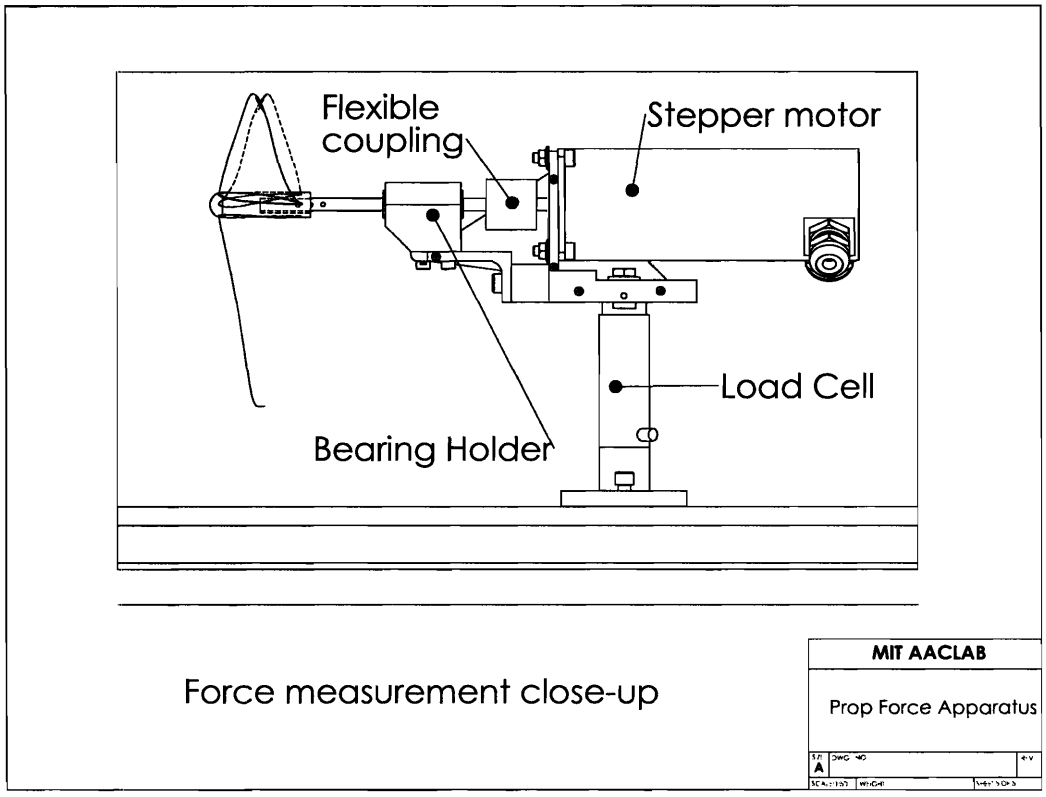

Figure A-1: Close up view of force measurement apparatus

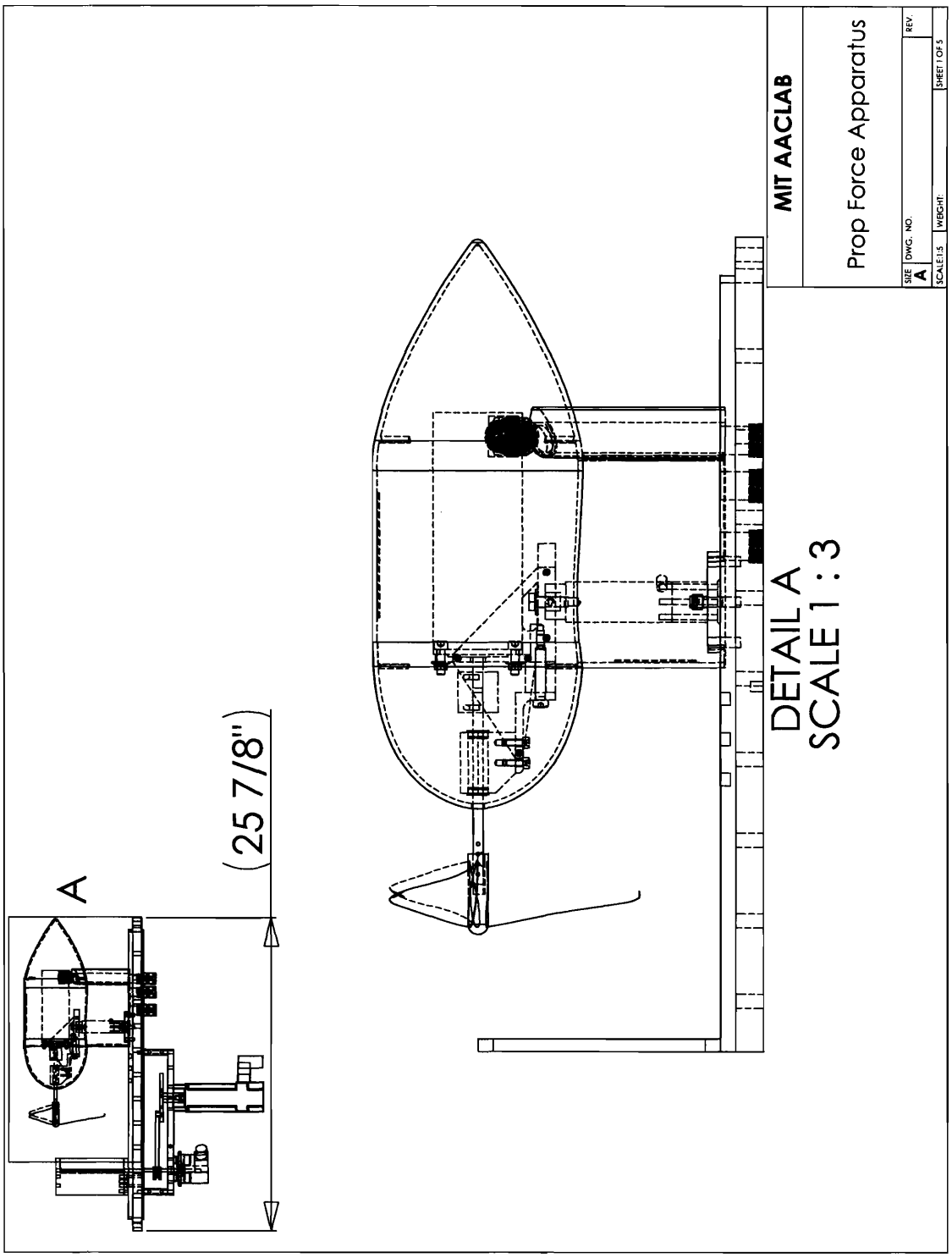

Figure A-2: View of complete apparatus

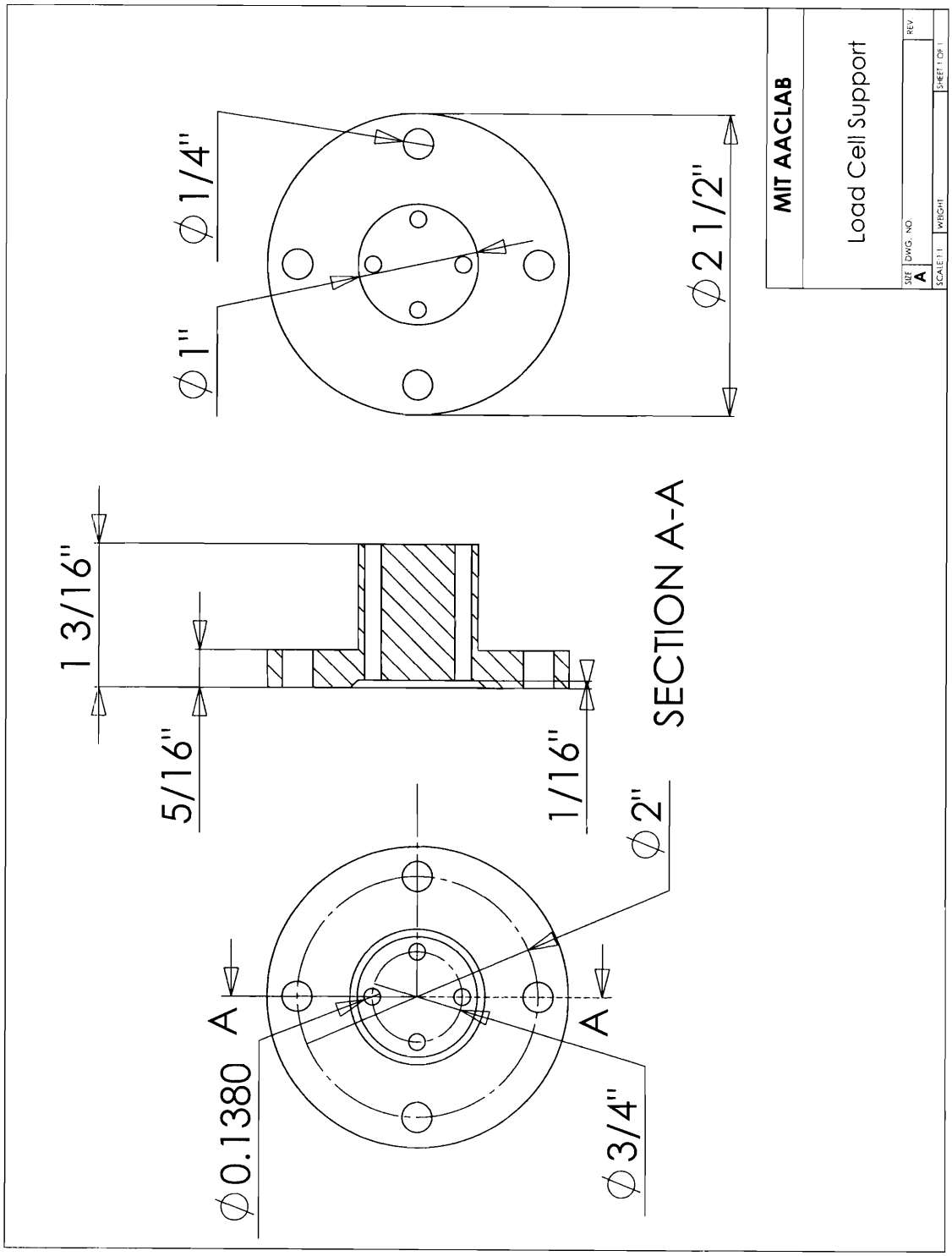

Figure A-3: Loadcell support

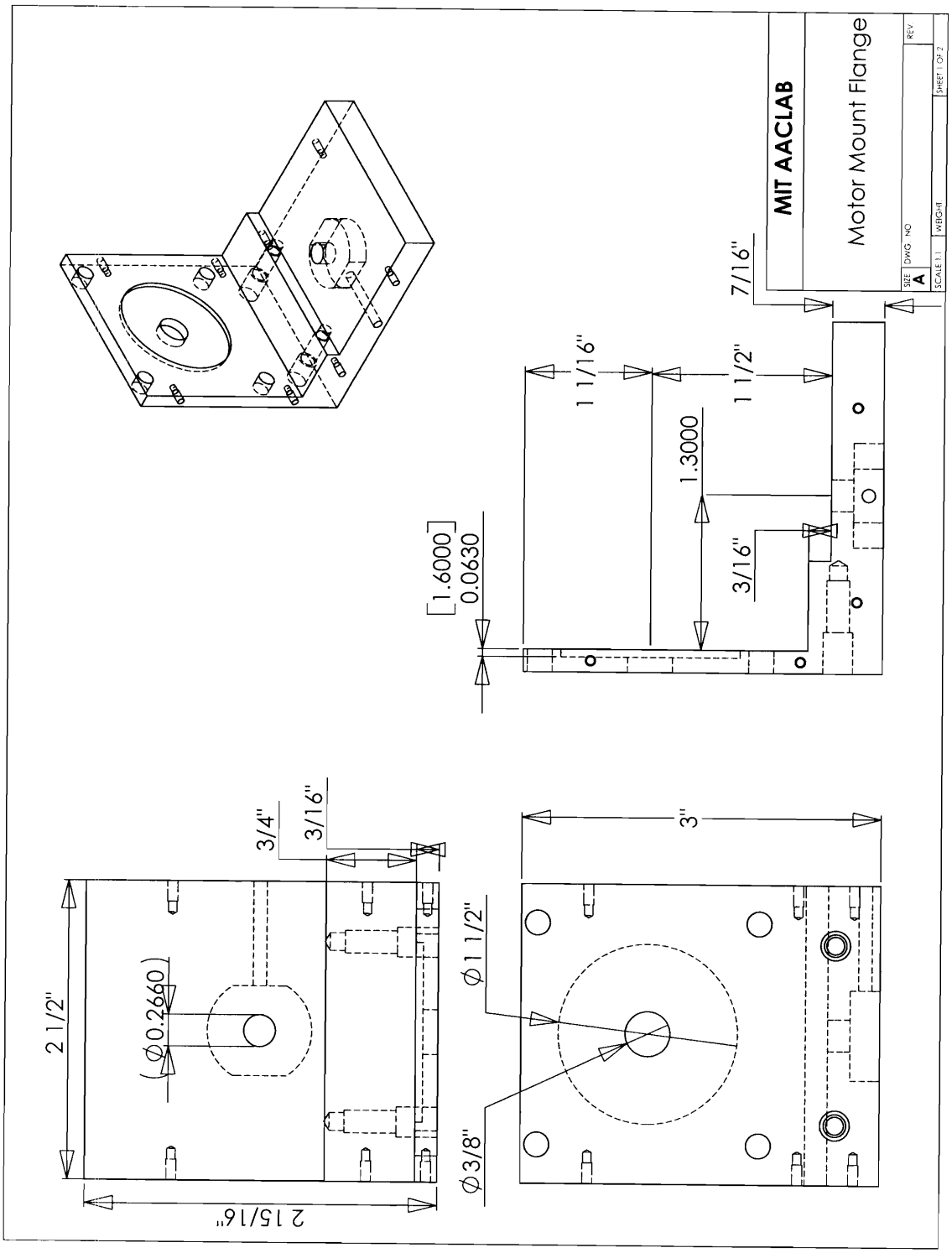

Figure A-4: Motor mount flange

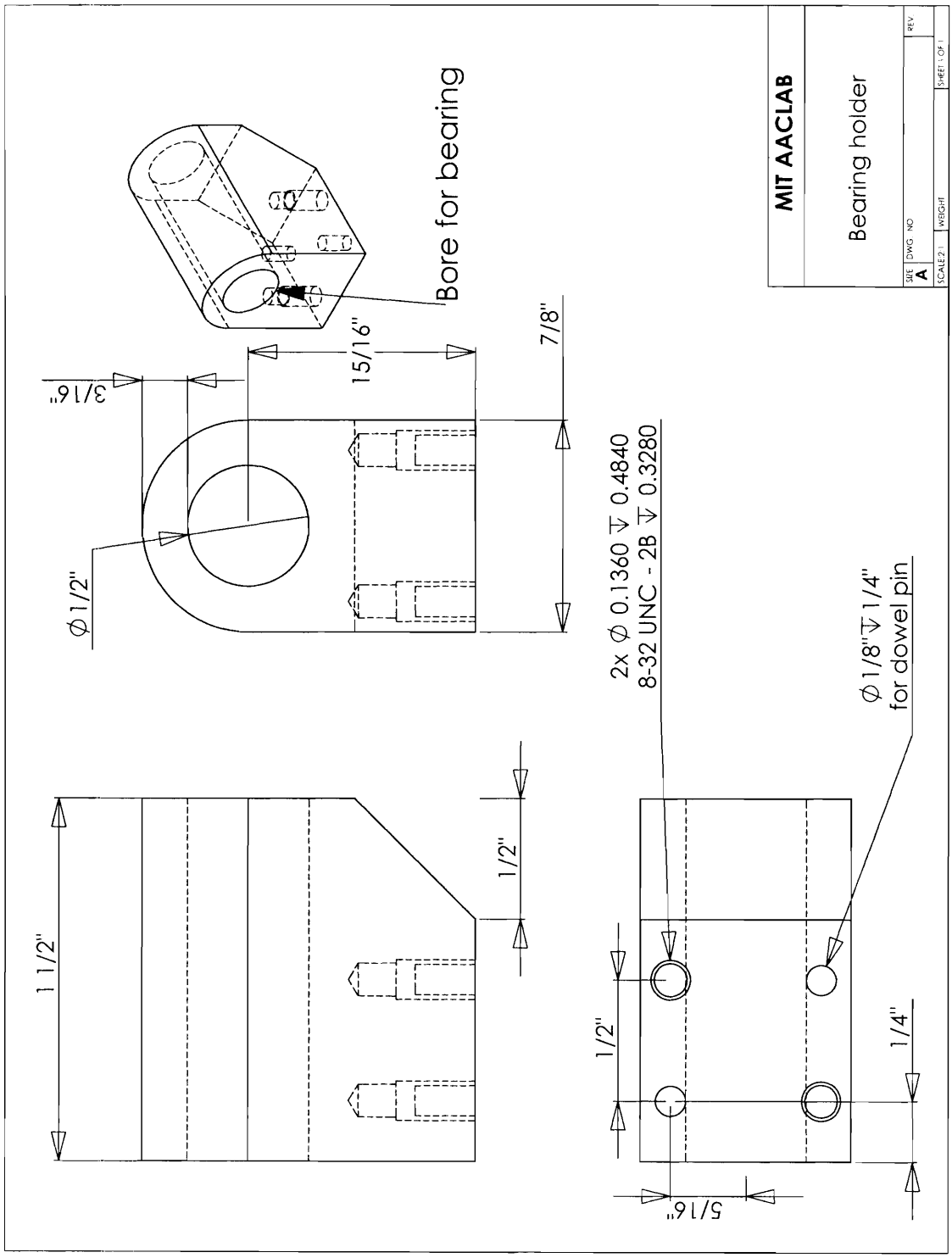

Figure A-5: Bearing holder support

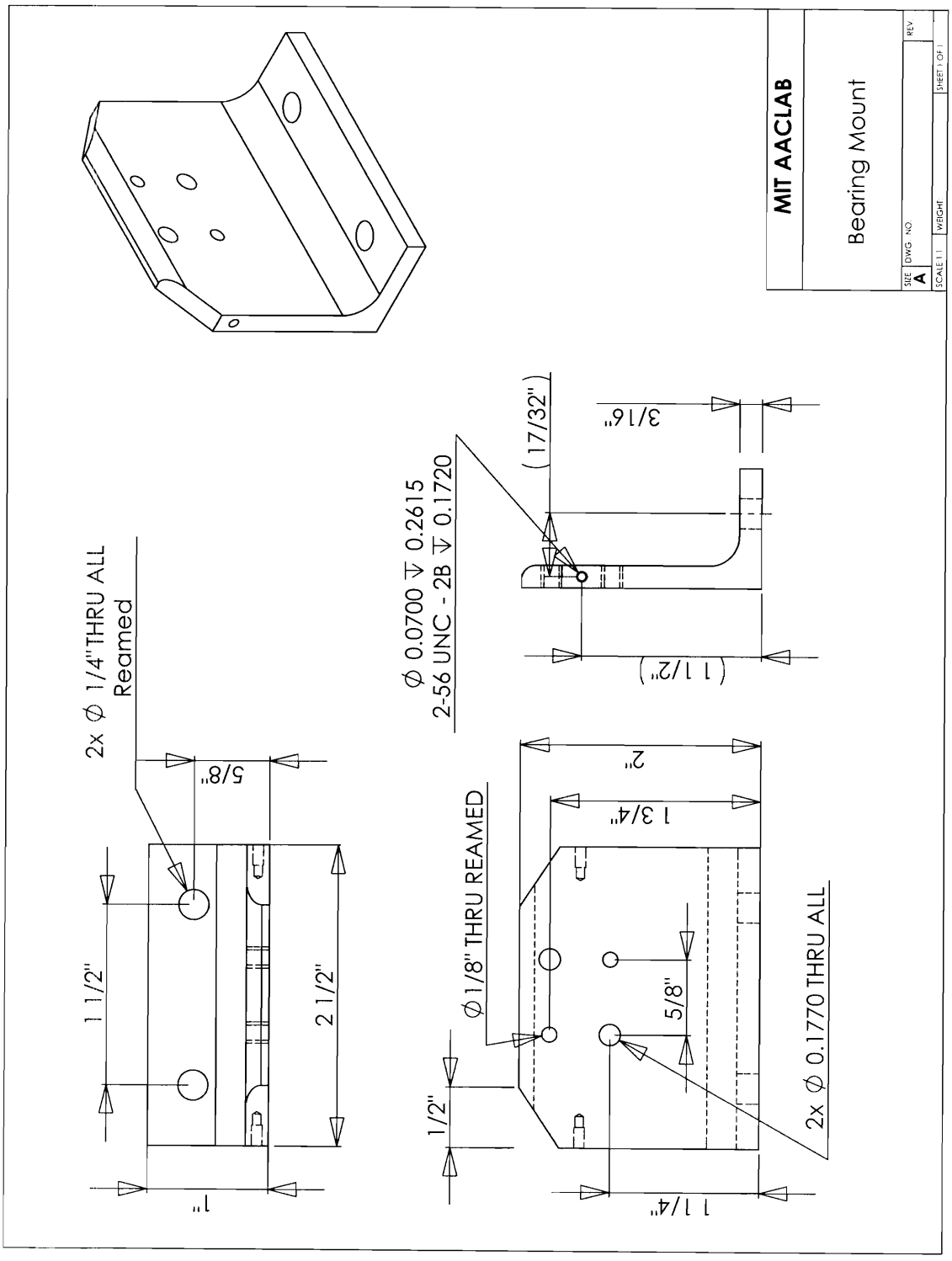

Figure A-6: Bearing holder support

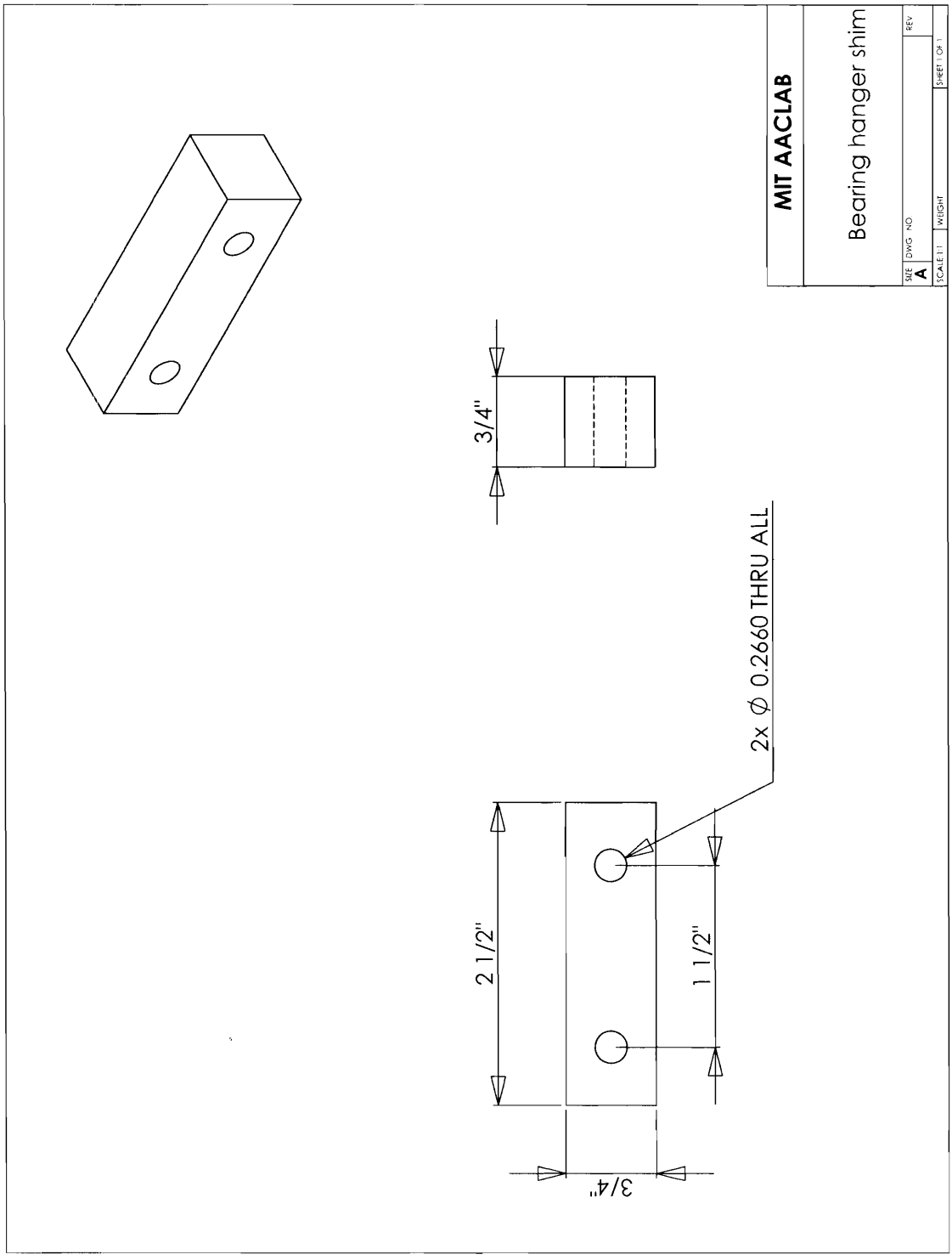

Figure A-7: Shim for bearing holder support

Figure A-8: Motor mount gusset

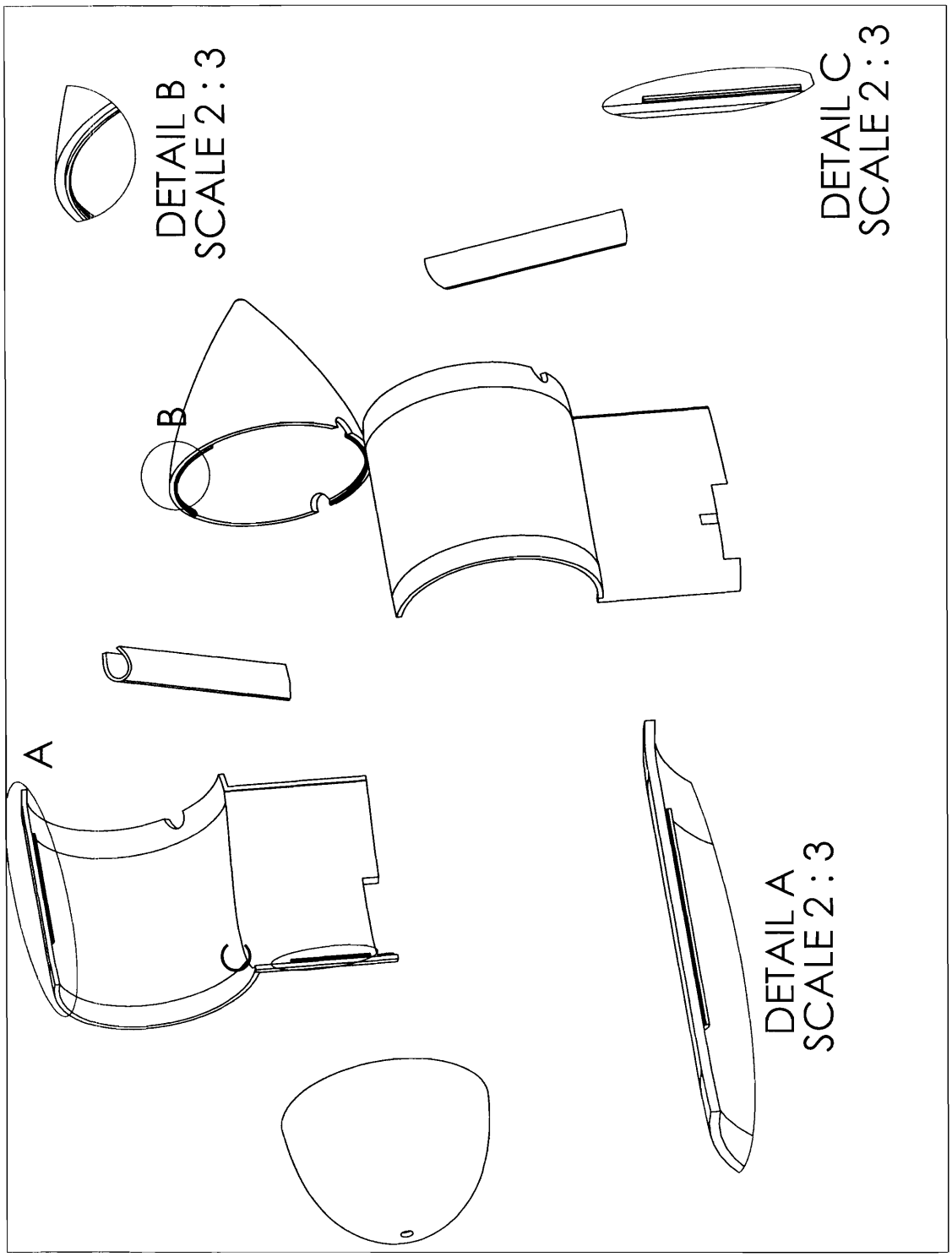

Figure A-9: Exploded-view of SLA fairing

Appendix B

Software Reference

B.1 Labview Modules

Propforce.vi: This vi was used to recored data six channel data recorded by the loadcell as well as the instantaneous stepper motor position. It initiates a test run according to the speed and phase settings specified in the control panel. It automatically sets up electronic gearing to synchronize the servo and stepper motor according to the number of propeller blades.

Zero_prog.vi: This vi is used to zero the position of the stator in its oscillation. It is used to ensure the stator's oscillations are centered about its undeflected position.

Zeroprop.vi: is used to move either the stepper motor or servo motor to their index position. The index position is used to repeatably position each motor at the beginning of a test run.

Propforceauto.vi: This is a modified version of propforce.vi used to facilitate the automation of test runs for a range of phases.

autoacquire.vi: This vi controls propforceauto.vi to automate a series of test runs for a specific propeller.

NI controller gains for servo motor: Kp - 150, Kd - 300, Ki - 120, Kv - 0
Td - 2, Ilim - 1000, Vfb - 0. Vff - 0, Aff - 0

NI controller gains for stepper motor: 2000 steps/revolution
Kp - 100, Kd - 1000, Ki - 0, Kv - 0, Td - 3, Ilim - 1000, Vfb - 0. Vff - 0, Aff - 0

RTSI bus routing for card synchronization: Stepper Encoder signals A,B and Index passed from motion control to DAQ card via RTSI bus. Pulses counted using on-board frequency counter

Counter Settings:

Pulses/Rev - 500, Initial Angle - 0, Z Index Enabled, Value - 0, Phase - A Low B Low, Decoding - X4 Stepper Encoder channel A to RTSI 0

Stepper Encoder channel B to RTSI 1

Stepper Encoder channel Index to RTSI 2

RTSI 0 to PFI8

RTSI 1 to PFI10

RTSI 2 to PFI9

AI Sample Clock to PFI0

AMC Drive Settings: 8192 Counts/index

Current Loop: P - 2.8439, I - .6543

B.2 Matlab Modules

(p,pavg,File,FT,RMS,dL,RMSdL,raw)=phasewake(bin,rpm,plot,frequency): This script calls **mreaddata** to load multiple data files. The files are loaded individually, filtered with a multi-pole butterworth filter using **filtfilt**. It is then sorted into bins of size *bin* from 0° to 360° stored in *p*. Data in each bin is averaged to create phase-averaged data. Phase-averaged data that correspond to the same test scenarios are averaged together to create multi-run averages in *pavg*. The derivative and root mean square of these phase averages are stored in *RMS*, *dL*, and *RMSdL*. The names of the orginal data files are stored in *File* while the *G* holds the post-processed data before being phase averaged. *FT* holds the fft of the filtered data sets.

(Filenames,data1,data2,...)=mreaddata: This scripts reads text files created in Labview from measured forces. It is called by **phasewake.m**. It loads a UI selectable number of data files and stores them in the variables data1,data2,etc. The number of outputs must match the number of inputs.

animprop(v,angamp,phase,prop,blade#,wake,file): This script is used to generate 3d visualizations of the propeller and stator wake. *v* is the propeller speed

in RPM, *angamp* is the amplitude of stator oscillation, *phase* is the phase angle between the stator tail and propeller, *prop* is a string setting which propeller model to use, *blade#* is the number of blades on the propeller, *wake* is a string that determines which pre-calculated wake flow field to use, and *file* is a string setting the name of the outputted movie file. This script uses wake files created by **MakeSimPuf.m**.

MakeSimPUF(f, tailv, taild0, bins): This scripts calculates the instantaneous flow field created by an articulating stator. **f** is the frequency of stator articulation in Hz, **tailv** and *taild0* are vectors that contain the velocity and tail tip position, and *bins* is the number of phase bins that will be calculated in one cycle of tail oscillation. The calculated flow field is saved as an external workspace file. *tailv* and *taild0* are created using **makesin.m**.

(tailv, taild0)=makesin(N,f,A,phase): This script generates the tail tip position and velocity vectors corresponding to sinusoidal flapping. N is number of points in tailv, f is tail flapping frequency in Hz, A is stator amplitude in deg, *phase* is the phase angle of oscillation in radians.

Bibliography

[1] Jamie M. Anderson. *Vorticity Control for Efficient Propulsion.* Ph.d. thesis, Massachusetts Institute of Technology, 1996.

[2] Triantafyllou G.S., Triantafyllou M.S., and Grosenbaugh M.A. Thrust development in oscillating foils with application to fish propulsion. *Journal of Fluids and Structures*, (7):205–224, 1993.

[3] W.P. Krol, A.M. Annaswamy, and P.R. Bandyopadhyay. A biomimetic propulsor for active noise control: Theory. Technical Report 11,350, NUWC-NPT, February 2002.

[4] C.C. Lindsey. Form, function and locomotory habits in fish. *Fish Physiology*, VII:1–100, 1978.

[5] Daniel L. Macumber. Blade tonal noise reduction using tail articulation at high reynolds number. Master's thesis, Massachusetts Institute of Technology, 2005.

[6] Daniel F. Opila. Active control of underwater propulsor noise using polypyrrole conducting polymer actuators. Master's thesis, Massachusetts Institute of Technology, 2003.

[7] D.F. Opila, A.M. Annaswamy, W.P. Krol, and S. Raghu. Biomimetic reduction of wake deficit using tail articulation at low reynolds number. *IEEE Journal of Oceanic Engineering*, 29(3):766 – 776, July 2004.

[8] D.A. Read, F.S. Hover, and M.S. Triantafyllou. Forces on oscillating foils for propulsion and maneuvering. *Journal of Fluids and Structures*, (17):163–183, 2003.

[9] Donald Ross. *Mechanics of Underwater Noise.* Peninsula Publishing, 1987.

[10] M. Triantafyllou and G. Triantafyllou. An efficient swimming machine. *Scientific American*, 272:64–70, March 1995.